University of Glasgow

Electrochemical Reduction of CO_2 to Oxalic Acid and Other Valuable C_2 Chemicals

Halilu Sale

Submitted in fulfilment of the requirements for the Degree of Doctor of Philosophy

School of Chemistry

College of Science and Engineering

University of Glasgow

2024

For Malam Sale Idris and Hafsat Sale

Abstract:

In recent years, there has been a growing interest and widespread adoption of electrochemical methods to address many of the energy and environmental challenges we encounter in modern society. This electrochemical approach encompasses a variety of highly adaptable techniques that often eliminate the need for harmful chemicals and extreme temperatures, aiming to offer an alternative to fossil-based compounds. In this thesis, we explore how electrochemistry can be harnessed for the development of a sustainable process based on electro-reduction. By showcasing the versatility of these techniques, our work covers a broad spectrum of approaches and analytical methods, with potential implications ranging from providing alternative pathways for industrially relevant chemical production to reducing reliance on fossil resources.

Chapter 1 introduces the electrochemical reduction of CO_2 to oxalic acid and other C_2 chemicals. It explains the fundamental concepts of this approach, discusses the parameters affecting its efficacy, and provides an extensive account of its application in previous and recent years. **Chapter 2** delves into the experimental techniques underpinning the research in this thesis.

Chapter 3 details the application of benzonitrile as a catalyst to enhance the electrochemical reduction of CO_2 to oxalic acid on the Pb electrode in propylene carbonate. Our findings indicate that the inclusion of benzonitrile in the electrolyte enhances the faradaic and reaction yields of oxalate/oxalic acid production, along with an improved area-normalized rate of formation. This achievement sets a record rate for oxalate/oxalic acid formation.

Chapter 4 explores the electrochemical reduction of oxalic acid to glyoxylic and glycolic acids on a Ti-based electrode. Our findings reveal that the direct electrochemical reduction of oxalic acid to these compounds of industrial importance (glyoxylic and glycolic acids) can be achieved with a high yield at room temperature, facilitated by the native oxides of titanium (Ti/Ti_xO_y).

Chapter 5 highlights the combined impacts of ultrasound and electrochemistry in the sonoelectrochemical reduction of CO_2 on a copper electrode, aiming to produce valuable products. The findings reveal a compelling outcome, which tackles the issue of bubble formation on the electrode surface and mitigates charge transfer resistance by amplifying the mass transport of electroactive species through acoustic streaming and cavitation phenomena.

Table of Contents

Acknowledgements

First and foremost, I would like to express my gratitude to Allah (SWT) for preserving my life in good health and granting me the opportunity to pursue chemistry up to the PhD level. I also wish to acknowledge my supervisor, Professor Mark Symes. Mark has been an exceptional mentor and guide since I joined his research group for my Ph.D. I am deeply indebted to him for his unwavering support, invaluable advice, and guidance whenever I sought it. Professor Symes has imparted a vast amount of knowledge about electrochemistry, serving as an exemplary role model. I aspire to have a similar impact on someone else's career in the future, just as he has had on mine.

Secondly, I would like to extend my heartfelt appreciation to my parents, who prioritised providing me with access to excellent education despite facing financial constraints. Their unwavering patience, support, and dedication to assisting me in every possible manner have been invaluable. I consider myself immensely fortunate and deeply grateful for their selfless generosity. Also, I would like to sincerely appreciate the Nigerian government's funding of my PhD through the Petroleum Technology Development Fund (PTDF).

I would like to express my gratitude to certain members of my immediate and extended family, whose support has been instrumental in my academic achievements. Special mention goes to Khadija Musa Kalong, who embraced me as a son following the untimely demise of my biological mother during my formative years. Mr. Edward Kwaptoe deserves recognition for sparking my interest in the field of science and guiding my career path. Additionally, I am thankful to other family members and friends, namely Alhaji Sa'idu Abdullahi, Alhaji Babayo, Haruna Muhammad, Alhaji Usman Abdullahi, Dr. Sulaiman Ihiabe Isah, Yusuf Abdulmumini, and Amina Jibrin, who have provided both financial and moral support throughout my academic journey. I deeply appreciate the guidance and contributions of each of you, and I will forever be grateful.

My PhD experience would have been significantly different without the numerous colleagues I had the privilege of working with over the years in the Symes group. Special thanks are owed to those who were present when I joined, guiding me in understanding the fundamentals of electrochemistry experiments, as well as those who joined the group after me. Particularly noteworthy are Nada Warid Alhathlaul, Athanasios Stergiou, Patrick McHugh, Abdulhai Faqeeh, Mbang Eze Obeten, and Ahmed Mohamad A. Aboor. I am grateful for your collaboration as part of the Symes group team. Undoubtedly, life within the group would not have been as enriching without such exceptional colleagues.

I must also extend a separate paragraph of acknowledgement to my two closest friends and postdoctoral researchers, Dr Lukman Yusuf, and Dr Zeliha Ertekin, with whom I have collaborated closely. Their support has been indispensable to the success of my research. Additionally, I would like to express gratitude to Amina Aminu for her constructive advice, support, and editorial contributions.

Finally, I extend my heartfelt appreciation to my beloved wife, Fatima Tanko. It is no overstatement to acknowledge that all my accomplishments throughout my PhD journey would have been unattainable without her untiring encouragement, steadfast support, and remarkable ability to effortlessly uplift my spirits when I am down with academic pressure. For her boundless love and support, I am eternally grateful. Special appreciation goes to my three kids (Hafsat, Muhammad, and Khadija Halilu), who double as my leisure crew during study-free time. You guys are amazing! May Allah bless your lives.

Author’s Declaration

I hereby declare that, unless explicitly referenced to the contributions of others, this thesis is the culmination of my efforts and has not been submitted for any other degree at the University of Glasgow or any other institution.

I declare that this thesis has been prepared in compliance with the University of Glasgow's code of good practice in research.

I acknowledge that if any concerns arise regarding good research practice following the examination of the thesis, the examination may be delayed until the resolution of any investigation into these concerns.

Halilu Sale

Abbreviations and Symbols

)))	Sonication
A	Ampere/Area
A.M.U.	Atomic Mass Units
AC	Alternating Current
C	Capacitance
c	Concentration/Speed of Light
CV	Cyclic Voltammetry
DC	Direct Current
e	Molar Absorptivity of the Compound
E	Potential
	Energy
EIS	Electrical Impedance Spectroscopy
ECR	Electrochemical Reduction
f	Frequency
F	Faraday's Constant
g	Grams
GC	Gas Chromatography
h	Planck's Constant
HER	Hydrogen Evolution Reaction
HPLC	High Performance Liquid Chromatography
Hz	Hertz
I	Current
IR	Infrared
K_s	Extinction Coefficient
K_f	Force Constant of a Bond

l	Optical Path Length
L	Litre
LC	Liquid Chromatography
LSV	Linear Sweep Voltammetry
M	Moles per Litre
m	Moles
	Metres
	Magnetic Quantum Number
m/z	Mass to Charge Ratio
M_0	Bulk Magnetisation Vector
min	Minute
MS	Mass Spectrometry
n	Number of Electrons Transferred per Ion
n_s	Refractive Index
NMR	Nuclear Magnetic Resonance
ppm	Parts per Million
Q	Charge
R	Resistance
R_a	Average roughness
R_q	Root Mean Square Roughness
R_p	Polarisation Resistance
R_{ct}	Charge Transfer Resistance
R_s	Solution Resistance
SCE	Saturated Calomel Electrode
s	Seconds
t	Time
TOC	Total Organic Carbon

TOF	Time of Flight
TMS	Tetramethyl Silane
UV-Vis	Ultraviolet-Visible
V	Volt
W	Watt
Z	Impedance
α	Rate of Change
γ	Gyromagnetic Ratio
δ	Chemical Shift
Ω	Ohms
ε	Molar Extinction Coefficient
λ	Wavelength
μ	Magnetic Moment/Effective Mass
ν	Frequency/Vibrational Quantum Number
ρ	Density
σ	Conductivity
τ	Bubble Collapse Time
φ	Phase Shift
ω	Radial Frequency
ω_a	Applied Ultrasonic Frequency

Introduction

Acknowledgements and Declaration

This chapter includes expanded and updated segments from the following published paper: "Optimising the Electrochemical Reduction of CO_2 to Oxalic Acid in Propylene Carbonate" H. Sale, G. R. Ubbara and M. D. Symes, *Sustain. Energy Fuels*, 2023, 7, 5093–5100.

The paper was written through the contribution of all cited authors.

1.1 Introduction

The current global environmental problems are closely related to energy consumption patterns. Using fossil fuels such as petroleum, coal, and natural gas has facilitated prosperous periods and played a crucial role in human advancement and development. As a result, the world has strongly depended on fossil fuels, employing them for energy production and in various manufacturing processes as a source of chemical feedstocks or intermediate chemicals for synthetic activities. However, the use of fossil fuels carries an environmental cost as it produces carbon dioxide (CO_2), a major greenhouse gas.[1] While it serves as a vital atmospheric component that supports plant growth and fosters wildlife and ecosystems, the equilibrium of CO_2 in the atmosphere has been substantially disrupted by industrial activities, leading to the current phenomenon of global warming.[2]

CO_2 is produced from natural and anthropogenic sources.[3] Fossil fuel combustion in different sectors produces around 37.5 gigatons of CO_2 annually, with the latter being the most deleterious to human and aquatic life.[4] The various forms of CO_2 emission and their sources are listed in Table 1.1.

Table 1.1: Classification of carbon dioxide emissions by sources according to Song.[5]

Entry	Sources		
	Stationary Sources	**Mobile Sources**	**Natural Sources**
1	Fossil Fuel-based Electric Power Plants	Cars, and Sports Utility Vehicles	Humans
2	Independent Power Producers	Trucks and Buses	Animals
3	Manufacturing Plants in Industry[a]	Aircrafts	Plant & Animal Decay
4	Commercial & Residential Buildings	Trains & Ships	Land Emission/Leakage
5	Flares of Gas at Fields	Construction Vehicles	Volcano
6	Military & Government Facilities	Military Vehicles & Devices	Earthquake

a) Major concentrated CO_2 sources include plants for manufacturing cement, limestone, hydrogen, ammonia, and soda ash, as well as fermentation processes and chemical oxidation processes.

Due to anthropogenic CO_2 emissions, data from the 'Earth System Research Laboratory' indicates that the average atmospheric CO_2 levels have increased to 416.35 ppm (parts per

million) as of August 2023.[6] Since 2017, there has been a global rise in CO_2 by approximately 10 ppm, leading to detrimental impacts on the ecosystem. Present CO_2 levels are at their highest ever in millions of years,[2] and if no action is taken to curb emissions or remove carbon dioxide from the atmosphere, it is projected to reach approximately 800 ppm by 2100.[7,8]

Consequently, it is imperative to address both problems of environmental pollution and energy usage simultaneously for environmental protection and sustainable development.

1.1.1 The Concept of CO_2 Conversion and Utilization

The concept of CO_2 conversion and utilisation involves transforming carbon dioxide into chemically different forms that contain the carbon of CO_2 or use an active "oxygen atom" from CO_2 to form another chemical or feedstock.[5,9] CO_2 utilisation refers to using CO_2 as a feedstock to produce various products, such as formic acid, methanol, ethanol, etc.[10] The concept represents a significant domain within chemistry and the global economy due to its vast potential. It can contribute to achieving net zero emissions whilst creating valuable products simultaneously. Most net-zero strategies tend to concentrate on the energy sector and how this can be decarbonised or de-fossilized. The petrochemical sector relies immensely on carbon derived from oil and gas to create various chemical compounds. These compounds serve as raw materials for industries such as plastics, textiles, pharmaceuticals, etc. Approximately 10% of carbon from oil and gas is used in these sectors. While net-zero strategies primarily focus on energy decarbonisation, we must also consider the petrochemicals sector's carbon usage to ensure a holistic approach toward sustainability and meet societal demands through the use of renewable sources. [5,9,11]

Though CO_2 is considered a pollutant and one of the major greenhouse gases in the atmosphere, it is identified as one of the cheapest and most naturally abundant carbon sources for producing fuels and varieties of useful intermediate chemicals for chemical industries.[12,13] The utilisation of CO_2 as a feedstock for the production of industrially relevant precursors represents a potentially sustainable way to make valuable chemicals without digging up fossil fuels.[14] Many approaches, such as chemical, photochemical, thermochemical, biochemical, and electrochemical reduction methods, have been deployed to achieve CO_2 conversion to useful forms[15–17]. Electrochemical reduction of CO_2 is promising due to the inherent advantages of forming various industrially relevant products, high conversion efficiency, ease of industrial scale-up and potential to store electrical energy obtainable from renewable sources like the sun.[12,14,18] However, application of the

electrochemical method is constrained by several factors, such as low current density, overpotential, catalyst instability and poor selectivity in some cases. Nevertheless, considering the number of advantages associated with electrochemical techniques over the other methods, we shall in this research look at the electrochemical reduction of CO_2 to oxalic acid, glyoxylic acid and glycolic acids to improve the efficiency of the process by overcoming some of the aforementioned limitations.

Electrochemical reduction of CO_2 typically takes place within an electrochemical cell. There are various cell configurations available, including single-chamber, double-chamber (H-cell) or flow cell, etc. The electrochemical cell and its components are discussed in the next section (section 1.2).

1.2 Electrochemical Cell

An electrochemical cell is a device that either uses supplied electrical energy to drive chemical reactions or generates electrical energy from the chemical reactions taking place within it. These devices can convert electrical energy into chemical energy and/or vice versa. An example of a typical electrochemical cell showing the various components of the cell is depicted in Figure 1.1.

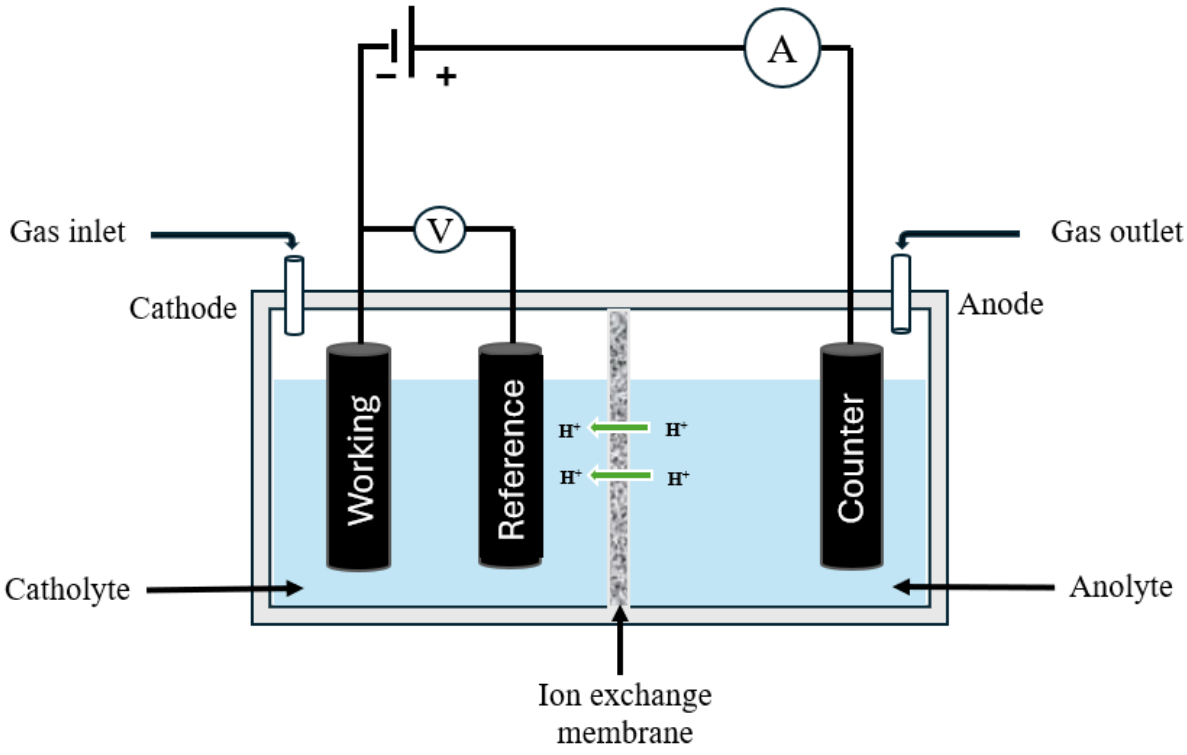

Figure 1.1: A schematic representation of a three-electrode electrochemical cell for CO_2 electrochemical reduction.

1.2.1 Factors Affecting CO_2 Reduction Reactions

Several factors are crucial in influencing the outcome of CO_2 reduction reactions. These factors encompass, among others, the type of electrodes employed, the catalysts (whether heterogeneous or homogeneous), the electrolyte, the temperature, the pH, the resistance, the separator (membrane), and the reactor's design.[19–23] It's crucial to optimise these aspects to ensure the reaction proceeds as efficiently as possible.

1.2.2 Electrolyte

In an electrochemical cell, the electrolyte typically consists of an inert electrolyte or salt (supporting electrolyte); the electrolyte facilitates the transfer of ions between the electrode compartments, thereby preserving the electrical neutrality of the system. The electrolyte plays a crucial role in enhancing solution conductivity, minimising the voltage drop across the system, and influencing the rates of various electrochemical reactions.

Generally, electrolytes should maintain a stable pH in bulk, exhibit good ionic conductivity, and possess moderate to high CO_2 solubility. It has been observed that the type, concentration, and composition of electrolytes can influence the electrochemical reduction of CO_2.[23] This implies that careful selection and optimisation of electrolytes are crucial for enhancing the efficiency and selectivity of the CO_2 reduction process.

When choosing an electrolyte for the electrochemical reduction of CO_2 to oxalic acid, it is essential that the selected electrolyte does not impact the quality of the resulting products. Therefore, a good electrolyte for CO_2 reduction should possess the following characteristics:[19 24 25 26 27]

1. High solubility for CO_2 to attain high current densities.
2. Low solubility to oxalic acid, simplifying downstream separation steps.
3. Electrochemical stability and chemical compatibility with the electrode materials.
4. Low viscosity, ensuring efficient CO_2 mass transfer rates and, consequently, conductivity.
5. Safety/non-toxicity.
6. Ease of handling and storage.
7. Availability.

8. High relative permittivity, meaning that electrolytes should readily dissolve and dissociate into cations and anions, enabling high electrostatic interaction between solutes and, therefore, high ionic conductivity and ionic transfer in the cell.

1.2.3 Electrodes

Electrodes are key elements in electrochemical cells, crucially enabling oxidation and reduction reactions which involve electron transfer between entities. Basically, the electrode materials perform the following functions in an electrochemical cell: [24]

1. Oxidation and Reduction Reactions: Electrodes are the specific sites where oxidation and reduction reactions take place. These electrochemical reactions involve changes in the oxidation states of substances, with some losing electrons (oxidation) and others gaining electrons (reduction). These reactions are vital to various applications, such as energy storage, corrosion prevention, and electrochemical synthesis.

2. Impact of Electrode Material: The material chosen for the electrodes significantly affects the rate of oxidation and reduction reactions. Different materials have unique electrochemical properties that can either accelerate or slow down these reactions. Hence, choosing the right electrode material is crucial for optimising the efficiency of electrochemical processes.

3. Electron Transfer: Electrodes have a dual role in facilitating electron transfer between the electrode and the reactants in the electrochemical reactions. In oxidation, the oxidising substance releases electrons that flow through the electrode. In reduction, the reducing substance accepts electrons from the electrode. This electron transfer is fundamental to the overall operation of the electrochemical cell.

1.2.4 Catalyst

In the realm of electrochemistry, a catalyst is often referred to as an electrocatalyst. An electrocatalyst is a substance that expedites electrochemical reactions, enabling them to occur more rapidly and at varying potentials than they would in its absence. This attribute is particularly beneficial in applications like fuel cells, electrolysis, and other electrochemical systems where reaction efficiency and kinetics are paramount.[25] The primary roles of a catalyst in an electrochemical reaction are as follows:

1. Enhancement of Reaction Rate: An electrocatalyst serves to boost the speed of electrochemical reactions. In doing so, it effectively reduces the activation energy needed for these reactions to take place. Activation energy is the energy hurdle that

must be surmounted for a chemical reaction to proceed. Lowering this hurdle quickens the pace of the reaction.

2. Alteration of Potential: Moreover, an electrocatalyst can modify the potential at which oxidation and reduction processes transpire. The potential is essentially the voltage or electrical energy necessary to drive a specific reaction. The presence of an electrocatalyst can shift the potential at which these redox processes occur, enabling them to happen more readily or under less severe conditions.

1.2.5 Temperature

Temperature changes can influence the potential energy of valence electrons within atoms of various elements, subsequently impacting the voltage of a galvanic cell. Typically, the temperature range employed for electrochemical reduction of CO_2 mostly ranges between 20-40 °C.[28] Generally, elevated temperatures lead to increased currents as ionic conductivity rises due to reduced viscosity, and the diffusion coefficient also experiences an increase, thereby enhancing the efficiency of CO_2 transport and distribution in the cell. On the contrary, the temperature rise is constrained by potential membrane degradation, resulting in a relatively narrow operational window; however, this limitation can be ameliorated by coupling the system with pressurisation.[26]

1.2.6 pH

The pH of the solution can affect both the standard and non-standard cell potentials. Changes in pH can drastically alter the rates of electrochemical reaction steps, potentially shifting them by several orders of magnitude. The formation of C_{2+} products, such as oxalic and glyoxylic acids, via various reaction pathways, depends on the protonation process. The transfer of protons can influence the product distribution in electrochemical CO_2 reduction. Hence, the pH near the catalyst electrode surface, bulk pH, and local pH have been found to impact the final product distribution.[29] Due to proton reduction, protons are consumed near the electrode surface, establishing a local pH (typically more alkaline than the bulk pH). This pH discrepancy is attributed to mass transport limitations and depends on operational conditions: current density, bulk pH, types of cations or anions, and electrode morphology.[20,26,29] Supplying suitable electrolytes with the correct pH is a crucial factor in controlling the reaction pathway and maintaining the stability of the reaction intermediates. In accordance with the pH effect, concentrations of H^+ and OH^- have been demonstrated to affect both the activity and selectivity of the electrochemical CO_2 reduction. The emergence of OH^- anions, resulting from electrochemical reactions, triggers an increase in pH on the

electrocatalyst surface, thereby boosting C_2 selectivity by inhibiting hydrogen evolution reaction. In addition to H^+ and OH^- ions, the nature of the electrolytes' cations and anions has also been reported to influence product selectivity significantly.[26]

1.2.7 Resistance

Resistance in an electrochemical cell is the hindrance experienced by the electric current as it traverses through the cell's components. In an electrochemical cell, the electrolyte's resistance can substantially affect the electric field between the electrodes. This, in turn, influences the cell potential and the efficiency of the electrochemical reactions due to the following factors:[20,27]

1. Voltage Drop: When the electrolyte resistance is high, it can cause a notable voltage drop across the cell relative to its electromotive force (EMF). As a result, the voltage that the cell experiences might be lower than the voltage applied due to the loss of some voltage to resistance.

2. Electric Field Variation: The electrolyte's resistance can alter the electric field's distribution. Discrepancies in the cross-section of the cell and the surface area of the electrodes can lead to an uneven distribution of the electric field.

3. Ion Movement: When subjected to the electric field between two electrodes, Ions formed in the electrolyte solution experience a force. This force induces motion and charge transport, resulting in ionic current flow through the electrolyte solution. Therefore, it is very important to use a less viscous electrolyte to minimise the cell resistance to ionic movement.

4. Electrode Distance: The resistance is also influenced by the distance between the electrodes. By reducing this distance, the resistance decreases.

1.2.8 Separator

Separators or membranes in electrochemical cells are critical components that permit the passage of only ions and prevent the crossover of oxidation and reduction products, which may form unsafe/unstable mixtures and make downstream steps more difficult. In addition, it also performs the following functions in an electrochemical cell:[30]

1. Maintains Local Conditions: The separator ensures the desired local conditions for the reactions occurring at the anode and cathode are maintained.

2. Provides Mechanical Support: It provides mechanical support to withstand any pressure differences between the chambers.

3. Mediates Ion Transport: The separator mediates the selective transport of ions from one half-reaction to another.

4. Prevents Parasitic Redox Shuttling: It prevents parasitic redox shuttling, i.e., reactions involving the reduction of a species at the cathode followed by its reoxidation at the anode.

5. Prevents Electrode Contact: The separator acts as a barrier, preventing direct contact between the electrodes and, in turn, averting the possibility of a short circuit.

Two primary types of separators can be identified: porous separators, encompassing materials like plastic mesh and microporous separators or diaphragms, and ion exchange membranes (IEM), which include monopolar separators such as cation exchange membranes (CEM) and anion exchange membranes (AEM), as well as bipolar membranes (BPM).[30,31]

Porous separators are essentially open structures. They come in two main types: (1) Plastic Meshes, such as polyolefin or Netlon, feature large pores ranging from 0.5-12 mm. They serve as supports for fragile electrodes, membranes, and microporous separators. Their structure promotes turbulence, thereby enhancing mass transfer near the electrodes. Furthermore, they provide minimal to no resistance to mixing anolyte and catholyte, and (2) Microporous Separators: Examples of these include glass fibres, porous polyvinyl chloride, and polytetrafluoroethylene. They have smaller pore sizes, between 0.1–50 μm, and function as both convection and diffusion barriers. Despite this, they remain permeable to the solvent, solute, and ions.[2,32]

Ion exchange membranes (IEM) typically consist of a thin polymer sheet with ion-exchange groups distributed throughout their structure. In the case of cation exchange membranes (CEM), which may include examples like ‘Nafion’, the ion-exchange groups are anions. Conversely, in anion exchange membranes (AEM), such as ‘Fumasep’, the ion-exchange groups are cations. These membranes have pore sizes ranging from 10^{-9} to 10^{-8} meters, effectively dividing the cell into two hydraulically separated compartments.[33] CEM, also known as proton exchange membranes, facilitate the transport of cations (H^+) from the anolyte to the catholyte. On the other hand, AEM enables the transport of anions in the opposite direction. Bipolar membranes (BPM) uniquely facilitate water dissociation into OH^- and H^+ under reverse bias. This drives these ions to the anode and cathode, respectively. This characteristic helps achieve more stable pH levels between the two electrodes and allows for the use of more economically viable electrocatalysts.[31,32] In 2008, Newman and his team[34] introduced a flow-cell reactor that contained Nafion for the reduction of gaseous

CO_2 to CO. This setup marked the first instance of gas-phase CO_2 electrolysis at ambient temperature and pressure in a flow cell based on a Proton Exchange Membrane (PEM). The different types of ion exchange membrane (IEM) used in the process (CO_2 to CO) are depicted in Figure 1.2.

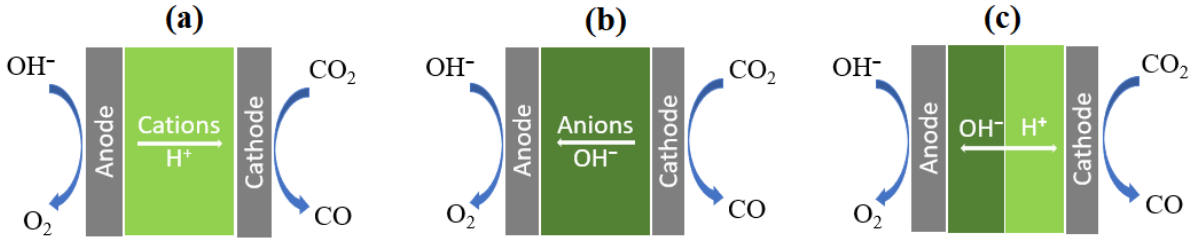

Figure 1.2: Overview of the various ion transport routes between the anode and cathode for three types of polymer electrolyte membranes in a gas-phase CO_2-to-CO electrolyser cell: (a) cation exchange membrane, the cations could be protons or other positively charged ions (e.g., K^+, Na^+), depending on the anolyte's nature. (b) anion exchange membrane, the anions could be OH^- and H^+ or another ion in the catholyte (e.g., HCO_3^-), and (c) bipolar membrane, which aids in water dissociation under reverse bias, driving OH^- and H^+ to the anode and cathode, respectively. It is implied that all reactions have a basic solution in the anodic compartment, as illustrated by Weekes et al.[31]

1.2.9 Electrolyser Configuration

Different types of electrolysers exist. They are categorised based on the number of compartments (one, two, or three-compartment cell), the method of feeding CO_2 into the cell, and the electrolyte phase.[22,26] CO_2 delivery methods include liquid form, dissolved in the catholyte solution, or ionic form (added outside the electrolyser, necessitating an extra step for CO_2 capture). Alternatively, CO_2 can be introduced directly as a gas using gas diffusion electrodes (GDE), which aids in overcoming mass transfer limitations from the gas phase to the cathode-catholyte interface.[30] As represented in Figure 1.3, the three common reactor configurations are batch or semi-batch cell (H-cell), flow cell system, and microfluidic reactors.[26]

1.2.9.1 H-Cell

H-type cells are popular due to their ease of assembly and operation, ability to separate products, configuration flexibility, and affordability. In this setup, the working and reference electrodes are positioned in the cathodic chamber, while the counter-reaction occurs in the anodic chamber. Both chambers are filled with electrolytes and operate without the need for recycling. In a typical "H" configuration, the chambers are generally linked by a circular

channel and divided by a membrane. CO_2 is consistently supplied to the cathodic chamber through a glass frit. The liquid products that form are gathered in the electrolyte, while the gaseous products are collected from the overhead space.[22] H-type cells serve as appropriate batch reactors for studying and comparing various electrocatalysts and products on a laboratory scale. However, their applicability does not extend to broader industrial applications.

1.2.9.2 Flow Cell System

Continuous flow-cell electrolysers are predominantly utilised on an industrial level where substantial amounts of CO_2 require processing. This is done to attain acceptable reaction rates and guarantee the process's economic feasibility.[30] The membrane electrode assembly (MEA) is the key component of flow cell systems. This assembly involves the attachment of electrodes to a solid polymer electrolyte or membrane. This membrane serves as a separator for the chambers and is responsible for the transfer of ions between them. The type of membrane used depends on the kind of ion being transported. For instance, a cation exchange membrane (CEM) transports protons from the anolyte to the cathodic chamber. An anion exchange membrane (AEM) transports hydroxide ions from the anode to the cathode. A bipolar membrane (BPM) is used when both types of ion transportation are required. Depending on the method of introducing CO_2 into the cell, two types of flow cell systems can be distinguished: the gas phase electrolyser and the liquid phase electrolyser. In the gas phase type, a humidified stream of gaseous CO_2 can be directly fed to the cathode, which in turn enhances mass diffusion and production rates. This design of the cell has been noted to enhance the partial current density and selectively produce C_{2+} products.[35] In the liquid phase flow electrolysers, both electrodes contain the liquid electrolyte. Consequently, this allows the system to be pressurised, enabling the feeding of CO_2 without additional humidification. Generally, these flow cells have demonstrated superior performance in electrochemical CO_2 reduction compared to H-type cells. This is primarily due to improved CO_2 diffusion and the local interface between the gas, electrolyte, and catalyst.[36]

1.2.9.3 Microfluidic Reactors

In microfluidic reactors, a CO_2 gas stream is introduced to the cathode, where it directly interacts with a porous gas diffusion layer with an electrode-electrolyte interface. Simultaneously, O_2 is supplied to the anode side. The cathode and anode are divided by an extremely thin channel, less than 1 mm in width, through which the electrolyte circulates. The byproducts and surplus protons generated at the cathode and anode are transported out

of the reactor along with the electrolyte stream.[22] The major advantage of such reactor design is avoiding issues related to membrane degradation and high cost, the absence of a separator permits wider pH and reaction temperature windows.[37] However, the presence of crossover may lead to the oxidation of the products. Nevertheless, this issue can be addressed through a multichannel design, a nanoporous separator, or a dual-electrolyte system.[38]

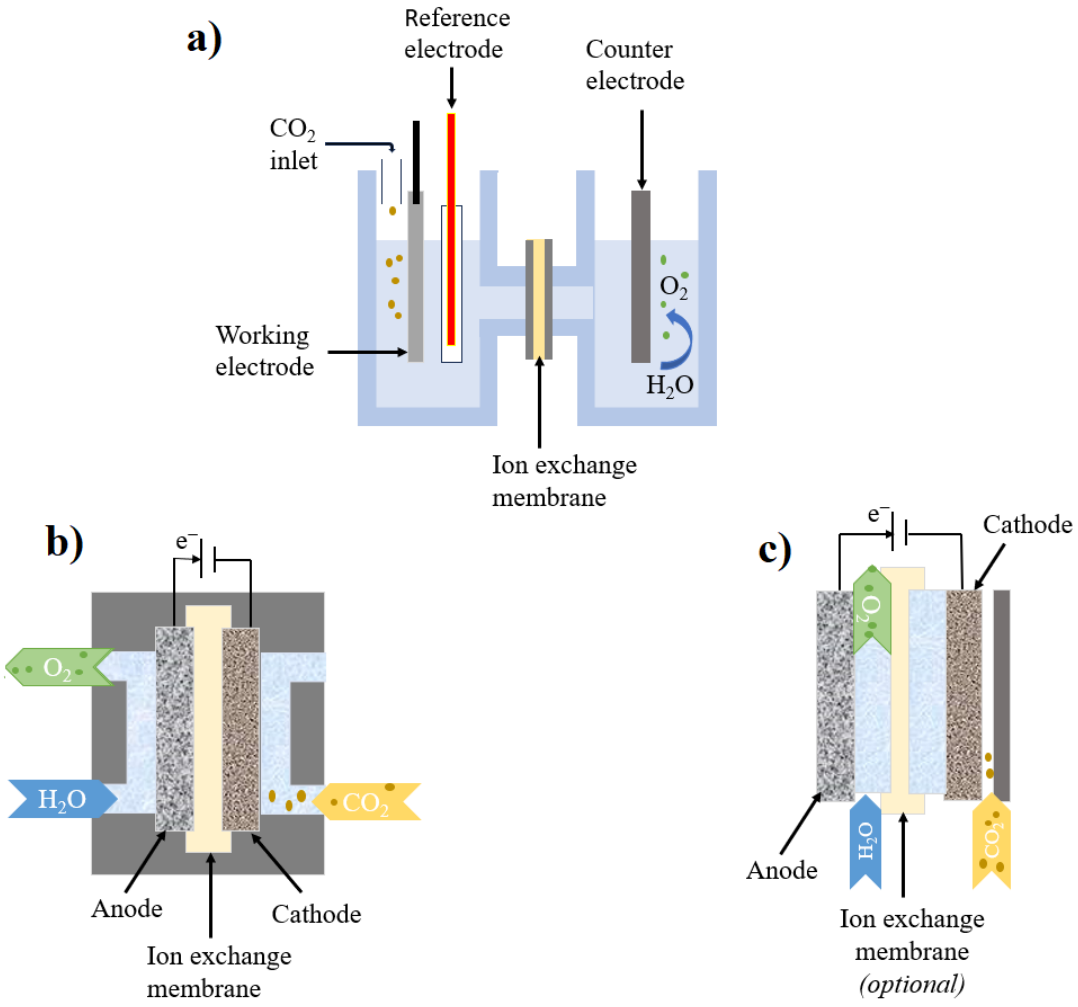

Figure 1.3: Showing the three different electrochemical reactor configurations: a) H-cell, b) flow cell, c) microfluidic cell as described by Ruiz-López et al.[26]

1.3 Electrochemical Reduction of CO_2

CO_2 contains the most oxidised form of carbon, together with carbonate minerals, having a formal oxidation state of +4. As a result, converting CO_2 into higher carbon products ($C_{n\geq2}$) requires the transfer of electrons to carbon, thereby reducing its oxidation state. The set of reactions responsible for converting CO_2 into a more reduced product is called "*CO_2*

reduction".[39] The electrochemical conversion of CO_2 has been studied via various mechanisms, including gaseous, aqueous, and non-aqueous phase methods, at both high and low temperatures. The choice of a particular medium and electrode largely depends on the target products. For instance, transition metal electrodes are widely used in low-temperature systems in both aqueous and non-aqueous mediums, but non-aqueous solvents in liquid electrolyte devices are preferable to minimise the competing hydrogen evolution reaction when it is not required in the process. [14] It is worth noting that the choice of an electrode and the reaction medium (either aqueous or organic) depends on the target product(s). A list showing the range of potential products obtainable from CO_2 conversion using a liquid electrolyte device at low temperatures is depicted in Fig. 1.4

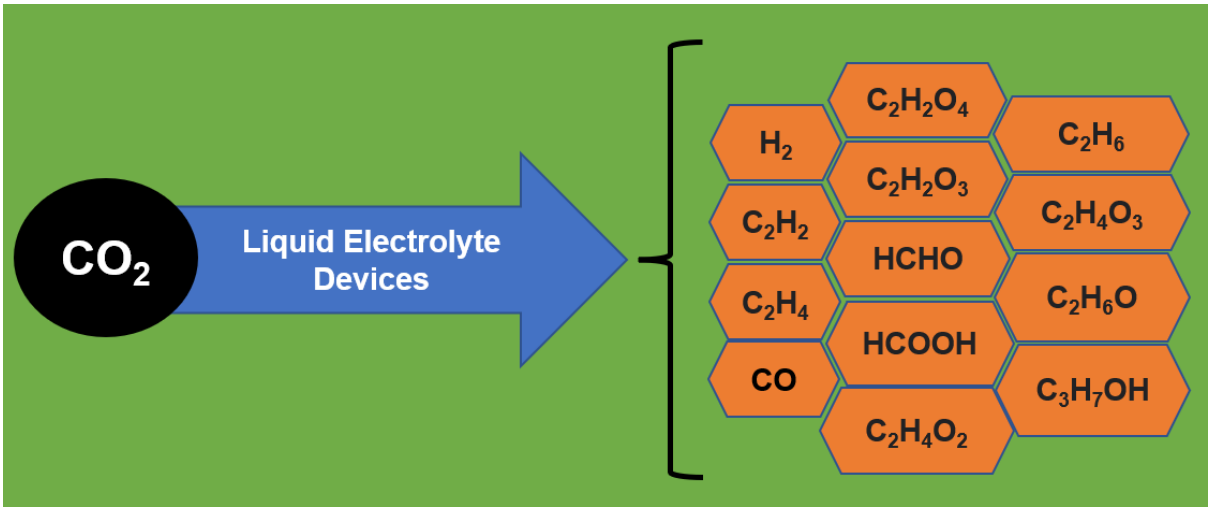

Figure 1.4: Showing a summary of potential products from electrochemical CO_2 conversion using liquid electrolyte devices as described by Spinner et al.[14]

Despite the progress made in converting CO_2 to different products electrochemically, the electrochemical method of CO_2 reduction is also not without some challenges; CO_2 is kinetically inert and thermodynamically stable, therefore a large amount of energy is required for the activation of CO_2 molecule to form an anion radical ($CO_2^{-\bullet}$) which serves as the initiation step of the reaction.[40]

The electrochemical conversion of CO_2 into a commodity or valuable chemical such as oxalate is a strategy for profitably utilising CO_2. However, previous research in this area reveals that electrocatalysts for oxalate generation require excessively large applied potentials[14,41–44]; this major drawback necessitated using catalysts to reduce the potential requirement and nonaqueous electrolytes (organic solvents) as a suitable medium that could limit the competing hydrogen evolution during CO_2 reduction.[45]

Electrochemical reduction of CO_2 can proceed through two-, four-, six-, or more electron reduction pathways in gaseous, aqueous, and nonaqueous phases at both low and high temperatures [42].

The reduction reactions of CO_2 are dominated by nucleophilic attack at the carbon, which results in the bending of the O—C—O bond. The most common reaction pathways are represented in Table 1.2 [46–50].

Table 1.2: showing some of the possible CO_2 reduction products and the corresponding standard reduction potential (E^0) vs. normal hydrogen electrode (NHE) at pH 0.

Entry	Cathodic Half-Cell Reaction	E^0 (V vs. NHE) at pH 0
1	$4H^+ + 4e^- \rightarrow 2H_2$	0.00
2	$CO_2 + 2H^+ + 2e^- \rightarrow CO + H_2O$	− 0.105
3	$CO_2 + 2H^+ + 2e^- \rightarrow HCOOH$	− 0.169
4	$CO_2 + 4H^+ + 4e^- \rightarrow HCHO + H_2O$	− 0.141
5	$CO_2 + 6H^+ + 6e^- \rightarrow CH_3OH + H_2O$	0.017
6	$CO_2 + 8H^+ + 8e^- \rightarrow CH_4 + 2H_2O$	0.169
7	$2CO_2 + 12H^+ + 12e^- \rightarrow C_2H_4 + 4H_2O$	0.079
8	$2CO_2 + 14H^+ + 14e^- \rightarrow C_2H_6 + 4H_2O$	0.142
9	$2CO_2 + 12H^+ + 12e^- \rightarrow C_2H_5OH + 3H_2O$	0.084
10	$3CO_2 + 18H^+ + 18e^- \rightarrow C_3H_7OH + 5H_2O$	0.099
11	$CO_2 + e^- \rightarrow CO^{\bullet -}$	−1.486

Table 1.2 shows some of the standard reduction potentials of CO_2 for various products depending on the reaction conditions. It is interesting to note that the standard reduction potential of the likely products is quite modest. However, a high potential is required to generate the carbon dioxide anion radical ($CO_2^{-\bullet}$), which is the necessary energy barrier that must be overcome to form the intermediate that can be converted to different products. It is also considered to be the rate-determining step (RDS) of the reaction. In addition to radical generation, another factor responsible for the high overpotential in CO_2 reduction is the kinetic barriers of multi-electron transport. This kinetic restriction has the tendency to limit or replace the reduction of CO_2 in aqueous electrolytes with a competitive hydrogen evolution reaction (HER), which is kinetically more favourable.[51]

High overpotential entails more energy requirements in the system, which is economically undesirable in both laboratory and industrial-scale production. Overpotential technically refers to the difference between the thermodynamic potential needed for a half-reaction to occur and the applied potential, which is needed for the actual reaction to occur.[52]

1.3.1 Early Work in Electrochemical Reduction of CO_2 to Oxalates/Oxalic Acid

Considering nature's ability to convert CO_2 into organic compounds through a sequence of light-dependent and light-independent reactions (photosynthesis). Over the years, this phenomenon has inspired researchers to emulate nature and evaluate the feasibility of utilising CO_2 to produce value-added $C_{n\geq2}$ materials.[53,54] In this regard, different catalytic approaches enabling carbonylation,[55] carboxylation,[56] or copolymerisation reactions[57] were developed based on CO_2 as a C_1 building block.[58] Moreover, the direct conversion of CO_2 into $C_{\geq2}$ compounds, such as ethane, ethylene, hydrocarbons, aromatic compounds, ethanol, and higher alcohols, has been achieved.[59–61] Nevertheless, the selective formation of $C_{\geq2}$ products under moderate reaction conditions remains a significant challenge. The absence of progress in this area starkly contrasts the notable advancements in CO_2 reduction to C_1 products, including methanol, carbon monoxide, formic acid, and methane, achieved through thermal, electrochemical, and photochemical methods.[62–64]

Furthermore, the mechanism governing the formation of C−C bonds seems to be highly specific to each respective system. Consequently, analysing oxalate in the presence of additional CO_2 reduction products through NMR or IR spectroscopy can be challenging,[65] and common analytical techniques for oxalate quantification have seen limited adoption in this field.[65–67] Oxalic acid is a dicarboxylic acid that contains two carboxylic acid groups. Due to the presence of these two groups, analysing oxalic acid by NMR spectroscopy can be challenging. The carboxylic acid groups can undergo hydrogen bonding with each other, resulting in broad and overlapping peaks in the NMR spectrum. Oxalic acid can be effectively analysed using IR spectroscopy when the concentration is high. In the IR spectrum, characteristic peaks corresponding to the carboxylic acid groups and the C=O stretching vibrations are observed. However, it is worth noting that generating an IR spectrum for oxalic acid becomes very difficult when its concentration is low[45].

These challenges impede the systematic development and refinement of protocols for coupling CO_2. Hence, the limited number of reports on CO_2 reductive coupling compared to well-established CO_2 reduction to CO, formic acid, and MeOH is not unexpected.[63,68,69] Nevertheless, recent findings revealed the successful analysis of oxalates/oxalic acid from CO_2 reduction by high-performance liquid chromatography (HPLC).[45,70]

Another key challenge in advancing selective processes for $C_{n\geq2}$ products lies in the step involving the formation of C − C bonds. A thorough comprehension of C − C bond formation originating from CO_2 could aid in designing specific catalytic systems, potentially enhancing the selectivity of transformations towards a target product.[71] The dimerisation of two CO_2

molecules resulting from two-electron reduction, leading to the formation of oxalate, known as CO_2 reductive coupling, serves as an excellent model reaction for studying the desired C − C bond formation. Furthermore, oxalic acid has been proposed as a foundational chemical for producing sustainable polymers and converting them into reduced C_2 compounds like glyoxylic acid, glycolic acid, glyoxal and ethylene glycol.[72,73]

Most of the early research work on the electrochemical reduction of CO_2 to oxalate/ oxalic acid has been done in aqueous electrolytes; very few researchers used non-aqueous electrolytes for the electrochemical conversion of CO_2. Many of the researchers discovered that lower temperatures are desirable for the reaction because they suppress hydrogen evolution and increase efficiency for CO_2 reduction.[74]

We shall start with a brief overview of the related work in this field, before exploring more recent developments in the electrochemical conversion of CO_2 to oxalate/oxalic acid. Initial findings highlighted the generation of oxalate in the electrochemical reduction of CO_2 on inert electrodes (Hg and Pb)[75,76]Also, aromatic esters or nitriles and transition metal complexes were reported as effective electrocatalysts for this process.[69] Historically, electrochemical reduction of CO_2 to oxalates/oxalic acid started about four decades ago.[77–84]

Savéant *et al*. [80] studied the electrochemical reduction of CO_2 using Pb and Hg electrodes in water-dimethylformamide (H_2O-DMF) solutions. The primary outcomes were CO, HCOOH, and $(COOH)_2$, with the product distribution influenced by operational conditions. They deliberated on the reaction mechanisms, assuming that a presumed intermediate, $CO_2^{-\bullet}$ is not adsorbed on either Pb or Hg electrode, and there is no specific interaction between intermediates or products and the electrodes.

Kaizer and Heitz[83] used Cr-Mo-Ni steel as a cathode in acetonitrile and propylene carbonate electrolytes, employing tetraalkylammonium salt as the electrolyte. They demonstrated that oxalic acid is the primary product. However, introducing a small amount of water into the electrolyte makes formate the main product.

In tetraethylammonium aqueous electrolytes under 10 atm conditions, Ito *et al*.[81] identified small quantities of oxalic and propionic acids by utilising Pb, Sn, and In electrodes for CO_2 reduction.

Eggins *et al.* [82] also investigated the reduction of CO_2 to oxalic acid; they employed carbon and Hg electrodes in aqueous solutions of tetramethylammonium chloride and tetramethylammonium hydroxide at pH 9. They obtained oxalic and glyoxylic acids in

addition to formic acid, as confirmed by the analytical outcome using high-performance liquid chromatography (HPLC).

Amatore and Saveant[77] have investigated and proposed a mechanism for reducing carbon dioxide in solvents of low proton availability, such as dimethylformamide. The research outlined the mechanism of reducing carbon dioxide in solvents of low proton availability based on the variation of the electrolysis products' distribution with the current density and concentration of CO_2 and water. Using the product distribution data together with the kinetic data obtained, it was concluded that the reduction of CO_2 in media of low proton availability appears to involve three competitive pathways as schematically illustrated in Scheme 1.1: oxalate formation through self-coupling of $CO_2^{-\bullet}$, formate formation through protonation of $CO_2^{-\bullet}$ by residual or added water followed by an electron transfer occurring in the solution, the electron source being $CO_2^{-\bullet}$ itself, and CO formation via oxygen-carbon coupling of $CO_2^{-\bullet}$ with CO_2. However, the diverse product distribution suggests that carbon-oxygen coupling of $CO_2^{-\bullet}$ with CO_2 appears as a negligible pathway for the formation of oxalate.

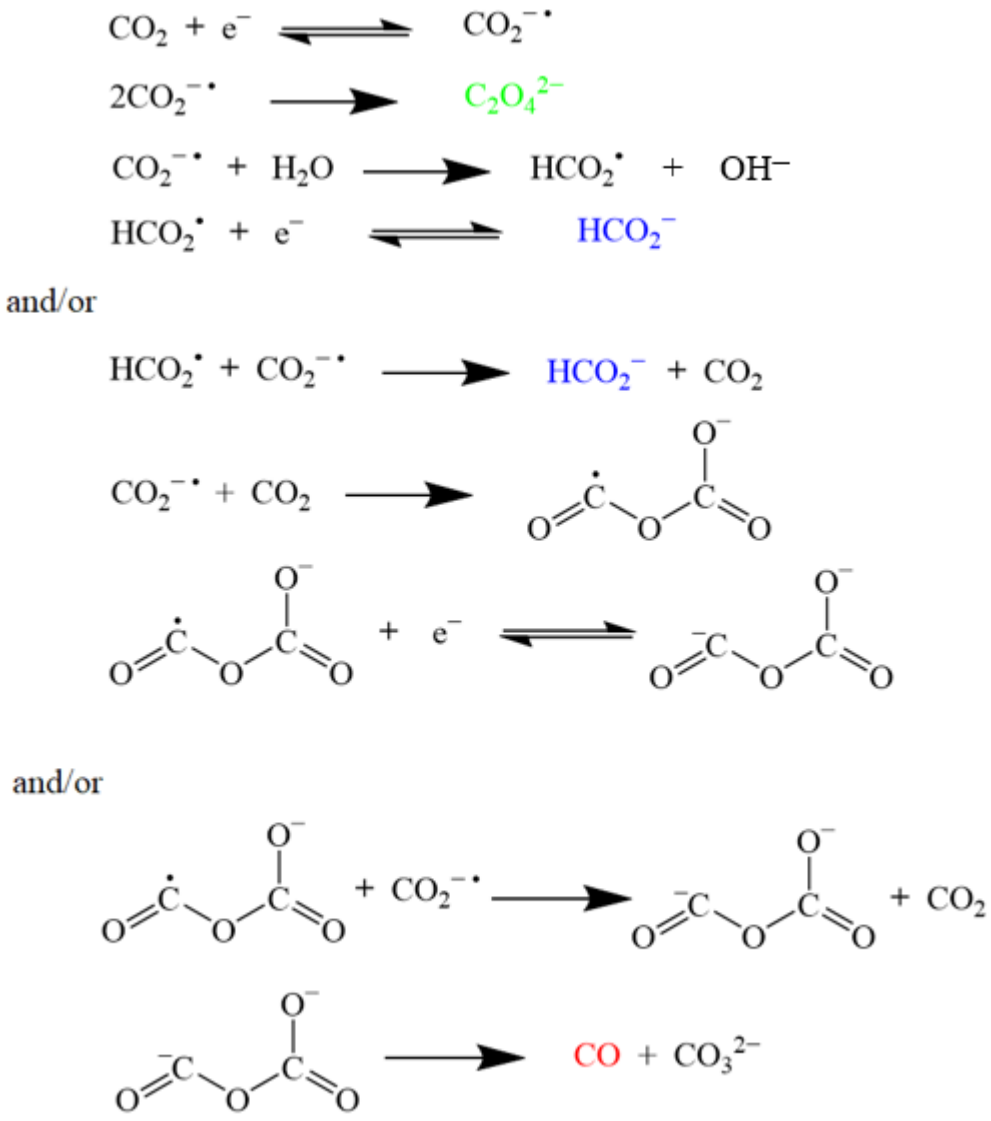

Scheme 1.1: Schematic illustration of product distribution of CO_2 reduction in a medium of low proton availability. Colour codes in the scheme are as follows: oxalate (green), formate (blue), and carbon monoxide (red), as described by Amatore and Saveant.[77]

Kaname *et al*.,[78] investigated the electrochemical reduction of carbon dioxide in nonaqueous electrolytes consisting of dimethyl sulfoxide (DMSO) as an aprotic solvent and tetraalkylammonium salts such as $(C_2H_5)_4NClO_4$, $(C_2H_5)_4NBr$ and $(n\text{-}C_4H_9)_4NBr$ using various metal electrodes such as Pb, In, Zn and Sn. The outcomes suggest that the main product was oxalic acid in the case of the Pb electrode. In addition, formic acid and some higher carboxylic acids, like tartaric, malonic, glycolic, propionic and n-butyric acids, were obtained in significant quantities in $(C_2H_5)_4NBr$/dimethyl sulfoxide. In $(n\text{-}C_4H_9)_4NBr$/Dimethyl Sulfoxide, oxalic, formic and tartaric acids were the major products obtained with small quantities of other organic acids. Experimental evidence confirmed

that the higher carboxylic acids mentioned above were produced through oxalic acid as an intermediate in the cathodic reduction of CO_2. For In, Zn, and Sn electrodes, carbon monoxide emerged as the primary product, albeit with the generation of minimal quantities of oxalic, malonic, glycolic, and formic acids.

Ito and colleagues[84] utilised various metal electrodes for constant potential electrolysis in CO_2 reduction at −2.8 V vs. Ag/AgCl in propylene carbonate, employing tetraethylammonium perchlorate (TEAP) as the electrolyte with a water content of 300 ppm. Only Pb, Hg, and Tl demonstrated significant Faradaic efficiency towards oxalate among all the tested metal electrodes. Consequently, metal electrodes were categorised into three groups, where Pb, Hg, and Tl emerged as the primary producers of $C_2O_4^{2-}$. Oxalic acid underwent partial reduction to glycolic acid and glyoxylic acid in the presence of a small amount of water in the electrolyte solution. Cu, Ag, Au, Zn, In, Sn, Ni, and Pt predominantly generated CO from CO_2. Fe, Cr, Mo, Pd, and Cd produced both $C_2O_4^{2-}$ and CO in comparable yields.

Hori *et al.,*[79] have investigated the electrochemical reduction of CO_2 using a platinum electrode in 0.1 M tetraethylammonium perchlorate in acetonitrile-water mixtures at a constant current density of 5mA/cm^2. It was found that Pt being inert in the reaction in aqueous media reduces CO_2 to oxalic acid in water-free acetonitrile. However, an increase in water concentration favours formic acid formation with a decrease in oxalic acid formation. As the concentration of water increased, the reduction of CO_2 was hindered, and hydrogen evolution became more dominant. The adsorption of CO on the surface of the Pt electrode was verified through in situ Fourier transform-infrared reflection absorption spectroscopy conducted in the electrolyte.

From the preceding discussions on the electrochemical reduction of CO_2 to oxalic acid under different conditions, it can be noticed that this process is complex and influenced by various factors such as the type of electrodes, electrolytes, and other conditions. Understanding the interplay of these factors is crucial for optimising the electrochemical reduction of CO_2 to oxalic acid. Each hypothesis points to the need for careful tuning of reaction conditions to achieve the desired efficiency, yield, and selectivity. Experimental investigations and computational studies can help validate these hypotheses and guide the development of optimised systems for CO_2 reduction to oxalate/oxalic acid. Based on experimental

outcomes and recommendations from early researchers, some of these factors profoundly affecting the electrochemical reduction of CO_2 are outlined as follows:[19,24,26]

1. Electrode Material: The choice of electrode material plays a significant role in the efficiency and selectivity of the reaction. For example, lead (Pb) cathode has been found effective in reducing CO_2 to oxalic acid in non-aqueous solvents, because $CO_2^{-\bullet}$ is not absorbed on the Pb electrode thereby creating room for the self-coupling of the anion radicals to form oxalate/oxalic acid.

2. Electrolyte Composition: The type and concentration of electrolytes can greatly influence the product distribution and overall efficiency of the reaction. For instance, more than 90% Faraday efficiency of oxalic acid can be achieved at a cathode potential of −2.5 V vs Ag/AgCl, but this occurs at relatively low current densities (10–20 mA/cm^2).

3. Reaction Conditions: Conditions like temperature, pressure, and applied potential can influence selectivity and product distribution. For example, low temperatures might slow down reaction rates but could improve selectivity by stabilizing intermediates. On the other hand, high temperatures can increase reaction rates but might lead to lower selectivity and more side products.

4. Process Optimization: The economic viability of the process could be further improved by optimizing reaction conditions to increase the current density and Faraday efficiency of oxalic acid. This can be achieved by eliminating water from the cathode, lowering the cell voltage, and applying a catalyst that could increase the conductivity of the electrolyte solutions.

These hypotheses provide a basis for further research and optimization in the electrochemical reduction of CO_2 to oxalic acid. However, more studies are needed to fully understand the complex relationship between these factors and to develop efficient and scalable processes for CO_2 reduction.

1.3.2 Recent Progress in the Electrochemical Reduction of CO_2 to Oxalates/Oxalic Acid

Recently, there has been growing interest in converting CO_2 to oxalic acid due to its enormous potential and versatile applications. The current oxalic acid market stands at 350,000 tons per year. However, in the future, oxalic acid has the potential to serve as the precursor for numerous high-value and high-volume chemicals. Two instances include formic acid/formate, with a market size of 900,000 tons per year or mono-ethylene glycol (MEG), with 30,000,000 tons yearly.[72] While it is possible to produce these chemicals from various sources, the sole alternative carbon sources are biomass and CO_2 if a fossil feedstock-free approach is to be achieved by 2050.[85,86] CO_2 reduction can potentially be a major platform for carbon-containing materials, such as new classes of polymers.[87] This does not only include products derived directly from oxalic acid but also the oxalic acid-based C_2 compounds like glyoxylic acid, glycolic acid, glyoxal, glycol aldehyde and ethylene glycol[72] This area stands poised for remarkable potential in the chemical industries, thanks to the development of the electrochemical process, which makes it possible to convert CO_2 with a high level of selectivity to the target products. The selectivity of products in CO_2 reduction is influenced by various factors, including the concentration of reactants, electrode potential, and temperature. Out of these factors, the electrode material and the solution are fundamental in determining product selectivity, as most researchers in the field have acknowledged.[41,58,81,82]

Over the last decade, intensive research has been conducted on the electrochemical reduction of CO_2 in both aqueous and non-aqueous solvents.[45,72,88,89] Although most of the early findings on CO_2 reduction are primarily in aqueous solvents despite the well-established benefits of nonaqueous solvents, such as high CO_2 solubility and the mitigation of the competing hydrogen evolution reaction (HER), there is relatively limited information available on CO_2 reduction in nonaqueous solvents.[90,91] Based on the overview of research findings on CO_2 reduction in section 1.3.1 Early Work in Electrochemical Reduction of CO2 to Oxalates/Oxalic Acid, it is evident that oxalate can be obtained in nonaqueous solvents with a notable Faraday efficiency (FE), although current densities tend to be relatively low.[45] Most of these experiments were performed in an H-cell reactor, resulting in low current densities due to limitations in mass transfer. In a recent development, Konig et al.[90] utilised a Pb gas-diffusion electrode (GDE) in a flow cell (flow-through configuration) to reduce CO_2 into oxalate, achieving a Faradaic efficiency of 53% at a current density of 80 mA/cm^2. However, the authors observed catalyst breakdown at high current density (> 100 mA/cm^2) due to

cathodic corrosion of Pb in the presence of tetraalkylammonium salts at elevated negative applied potentials.

The electrochemical reduction of CO_2 to oxalate in nonaqueous solutions poses more challenges than other electroreduction products such as formic acid, CO, and hydrocarbons.[92] Specifically, the difficulties in CO_2 reduction to oxalate in nonaqueous solvents revolve around the need to identify suitable catalysts, electrolytes, and membranes for stable operation.[45] The distribution of products in CO_2 reduction can greatly differ, mainly depending on the metal electrode and the electrolyte solutions used in the reaction. Multiple reactions occur concurrently on the surface of the electrode. The electrode serves as the reaction site, and the adsorption of reactants and other related species influences the selectivity of products in CO_2 reduction. The adsorption strength also affects the selectivity of any species that are adsorbed on the surface. The electrolyte solution dictates the concentration and stability of the reactants and intermediate species.[41]

Ikeda et al.[93] outlined various results from CO_2 reduction reactions, with the CO_2 anion acting as an intermediate. Figure 1.5 provides an overview of the reaction products formed, based on the type of solvent and electrode employed. It is important to highlight that the products of the reaction vary between aqueous and non-aqueous solvents. The mechanisms of the reaction also change depending on the presence of a proton donor. Formic acid is generated on indium, lead, and mercury in aqueous solvents. CO is formed on zinc, silver, and gold in aqueous solutions, and also on zinc, tin, and gold in non-aqueous solvents. Oxalic acid is produced on lead, thallium, and mercury in non-aqueous solvents.

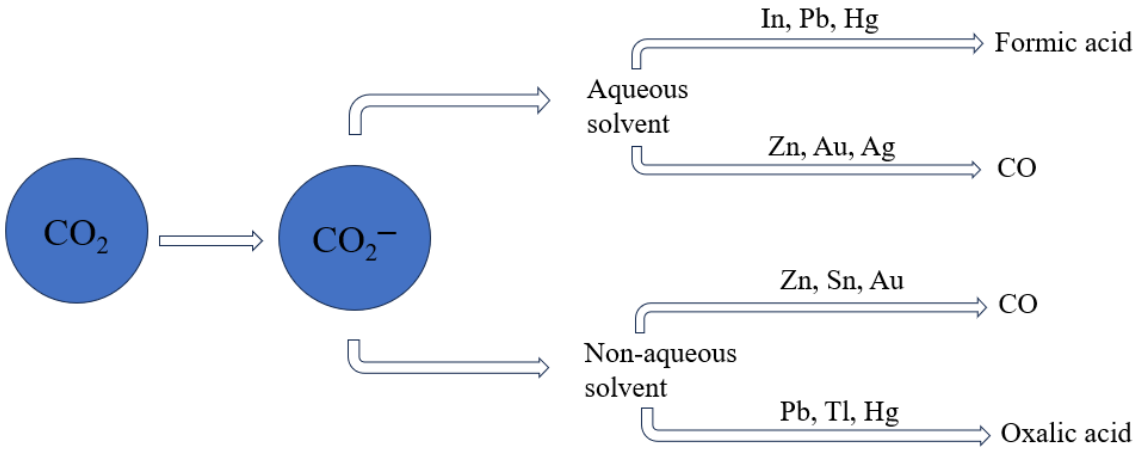

Figure 1.5: The CO_2 reduction reaction routes and the various products obtainable on different electrodes in aqueous and non-aqueous medium as described by Ikeda et al.[93]

The promise of CO_2 reduction is great, offering a pathway to a more sustainable future by utilising what is essentially a waste product. However, substantial technological advancements are needed for this process to be economically feasible and acknowledged as a solution to global challenges posed by the rising CO_2 concentration in the atmosphere.

The evolution of electrochemical CO_2 reduction depends on meeting three fundamental criteria: high energy efficiency, long-term stability, and the attainment of high current densities for reaction rates and turnover. A major obstacle to progress is the significant gap in understanding the mechanism of CO_2 reduction. Numerous attempts have been made to model this through experimental and computational approaches,[94–96] but the pathways to generate valuable products or chemical intermediates have not been conclusively clarified. Clarifying these pathways would offer valuable insights into the chemistry behind CO_2 reduction at the electrode/electrolyte interface and mechanisms to achieve high faradaic efficiencies. Various factors and sub-branches must be considered to achieve these high faradaic efficiencies. The catalyst must be capable of suppressing competing hydrogen evolution reaction while also being selective towards the desired products. Therefore, the operating conditions must be optimised for the best yields and efficiencies.

Another challenge to consider is the high overpotentials associated with these reactions. The energy input into the system compared to the products obtained from it is small, therefore reducing this high overpotential is necessary. The high overpotential can be attributed to the limiting step in CO_2 reduction, which is the formation of the radical anion intermediate $CO_2^{-\bullet}$ In water and many solvents, the equilibrium potential for forming this anion intermediate is very negative, resulting in a high overpotential. Therefore, the role of the catalyst would be to stabilise this intermediate. The solubility of CO_2 is also relatively low in most aqueous electrolytes under the conditions used for CO_2 reduction, introducing a mass transfer limitation of the CO_2 to the electrode surface.

Therefore, a combination of a suitable catalyst, reactor design, and efficient product analysis is necessary to reduce CO_2 efficiently and achieve the goal of obtaining high-value products.

In recent decades, the field of electrochemical CO_2 reduction has seen significant growth and achievements. Nonaqueous solvents have been identified as the preferred medium for reducing CO_2 to oxalic acid, primarily due to the absence of the hydrogen evolution reaction, which tends to dominate in aqueous solvents. One of the most recent advancements in this area is the research reported by Boor et al.,[45] in which a combination of various organic

solvents and salts (supporting electrolytes) was examined. The results suggest that a mixture of tetraethylammonium chloride and propylene carbonate is an effective medium for the electrochemical reduction of CO_2 to oxalic acid, although it requires a higher applied potential of −2.7 V vs Ag/AgCl. In conclusion, the research team hypothesized that the use of an appropriate catalyst could potentially lower the potential requirement in the system, leading to an overall increase in efficiency. However, there is still limited scientific knowledge of the catalytic mechanisms. The multiple bond-breaking and forming processes and the sheer complexity of the reaction environment contribute to significant difficulties in elucidating precise catalytic mechanisms and pathways, thus hindering the fine-tuning of the reaction conditions, kinetics, and chemistry. Further research is also needed to understand and suppress the competing and parasitic hydrogen evolution reaction (HER) occurring in the process.

1.3.3 Application of Electrocatalysts in CO_2 Reduction

Electrocatalysts play a role in enhancing the rate of oxidation and reduction reactions in electrochemical processes. They represent a specialised category of catalysts designed specifically at electrode surfaces or as the electrodes themselves. The primary function of electrocatalysts is to expedite the transfer of electrons between electrodes and reactants, and they can also facilitate intermediate chemical transformations described by an overall half-reaction.[97] Electrocatalysts are classified into either homogeneous or heterogeneous catalysts.[98]

Catalysts have played a significant role in CO_2 reduction for over 40 years. However, the primary emphasis during this period has been on generating syngas or directly forming possible fuels. Benson et al. have comprehensively reviewed this subject.[99] Some research groups have directed their efforts towards the production of oxalate. Becker *et al.*[100] pioneered the development of homogeneous catalysts specifically designed for oxalate formation. They utilised silver and palladium porphyrins, successfully lowering the operational potential. Notably, they observed selectivity towards oxalic acid. However, they did not provide specific selectivity or efficiency figures and did not delve into potential mechanisms.

Kushi *et al.*[101] adopted a distinct approach, employing a rhodium sulfide cluster in CO_2-saturated CH_3CN in the presence of $LiBF_4$. Adding rhodium sulfide to the electrolyte as a homogeneous catalyst facilitated the reduction of CO_2 to oxalate as a predominant product; the electron-rich sulfur ligands are the possible sites for the activation of CO_2 by the metal-

sulfur clusters, as shown in Figure 1.6. They successfully reduced the operational potential to −1.5 V, achieving a 60% current efficiency. The cluster was constructed on a glassy carbon plate and displayed no indications of fragmentation. Notably, low-valence metals and electron-rich sulfur ligands can be potential sites for activating CO_2 by metal-sulfur clusters. Fourier-transform infrared spectroscopy (FTIR) revealed the bonding of CO_2 to the reduced clusters, occurring either at two Rh sites or at an S and Rh site. In a subsequent investigation, they demonstrated superior activity by employing iridium and cobalt complexes, enabling the reduction of operational potentials to −1.3 and −0.7 V, respectively, while still achieving a 60% current efficiency. This represents a significant reduction in the overpotential, amounting to 1.4 V compared to the uncatalysed reaction.[102]

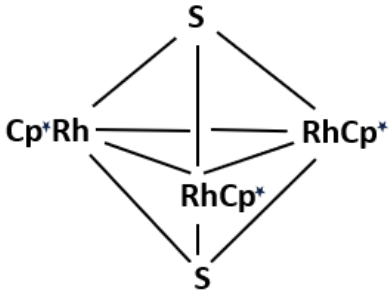

Figure 1.6: Structure of rhodium (Rh) cluster $[1]^{2+}$ as described by Kushi et al.[101]

Furthermore, Evans *et al.*[103] examined the application of lanthanides, specifically samarium in the form of divalent and trivalent complexes, as an effective catalyst to achieve good yield and selectivity for oxalic acid under suitable conditions. One of the major challenges associated with this process is the difficulty in separating the product of CO_2 reduction from the divalent and trivalent complexes of samarium $(C_5Me_5)_2Sm$.

Kumar et al.[104] adopted a different strategy for arranging their catalyst by designing a copper-based metal-organic framework (MOF). They managed to reduce the overpotential by 0.7 V and increase the current density from 2.27 to 19.22 $mAcm^{-2}$ in dimethylformamide (DMF) solution with Tetrabutylammonium tetrafluoroborate (TBATFB) as supporting electrolytes. They proposed the formation of the $CO_2^{-\bullet}$ radical anion, which couples to oxalate and abstracts a proton from the solvent to produce oxalic acid with 90% selectivity at 51% Faradaic efficiency.

The use of transition metal complex systems has the ultimate advantages of offering high selectivity and using non-precious metals in some cases. Nevertheless, there are significant

drawbacks, such as low Faraday efficiency, extended reaction times, and the use of toxic solvents like dimethylformamide. Moreover, process development faces challenges due to the complexity of these systems, and it is currently in the early stages of development at the laboratory scale. These factors underscore the challenges and complexity associated with these systems.[105]

1.3.4 Kinetics of CO_2 Electroreduction

Kinetics in electrochemical reactions refer to the study and characterisation of the rates at which electrochemical processes occur and the factors influencing these rates. The kinetics of CO_2 electroreduction describe the reaction rate, charge transfer, mass transport and possible pathways for reducing CO_2 into different products. Several factors, as highlighted in section **1.2.1** Factors Affecting CO2 Reduction Reactionsare crucial in determining the outcome or selectivity of CO_2 reduction reactions. Although different reaction mechanisms have been proposed, it is generally agreed that the initial step consists of a single electronation of the CO_2 molecule to form an anion radical (equation 1.1).[106]

$$CO_2 + e^- \longrightarrow CO_2^{-\bullet} \qquad \textit{(Equation 1.1)}$$

This first step is the rate-determining step of the process. Due to the linear nature of the CO_2 molecule, a substantial energy barrier exists, which makes the electrochemical reaction energy-intensive, as a high overpotential is needed. This barrier can be reduced by protonating the reduction products. CO_2 reacts with hydrated electrons in either the gas phase or aqueous medium to form a radical anion, which is stabilised by hydration.[107]

In the second step, the $CO_2^{-\bullet}$ generated in step one accepts protons, one from water and one or more electrons from the electrode, respectively. Reaction products like formate ions could be produced at this stage (equation 1.2 and 1.3).

$$CO_2^{-\bullet}{}_{(ads)} + H_2O \longrightarrow HCOO^{\bullet}{}_{(ads)} + OH^-_{(aq)} \qquad \textit{(Equation 1.2)}$$

$$HCOO^{\bullet}{}_{(ads)} + e^- \longrightarrow HCOO^-_{(aq)} \qquad \textit{(Equation 1.3)}$$

The existence of free protons in the acidic supporting electrolyte provides another source of hydrogen ion which can interact with the adsorbed $CO_2^{-\bullet}$ anion radicals (equation 1.4).

$$CO_2^{-\bullet} + H^+ \longrightarrow HCOO^{\bullet} \qquad \textit{(Equation 1.4)}$$

In an aqueous media, most flat metallic cathodes yield carbon monoxide and formic acid [108,109]. Conversely, in nonaqueous media, the radical anion generated in equation 1.1 may undergo a dimerisation reaction with an electrically neutral CO_2 molecule to form $^{-}OOC–COO^{\bullet}$ (ads) (equation 1.5), followed by a second electronation to give oxalate ions (equation 1.6)

$$CO_2^{-\bullet}{}_{(ads)} + CO_2 \longrightarrow {}^{-}OOC—COO^{\bullet}{}_{(ads)} \qquad \textit{(Equation 1.5)}$$

$$^{-}OOC—COO^{\bullet}{}_{(ads)} + e^{-} \longrightarrow {}^{-}OOC—COO^{-}{}_{(aq)} \qquad \textit{(Equation 1.6)}$$

Eggins et al.[43] reported a competing reaction happening simultaneously with the dimerisation reaction to oxalate. The competing dimerisation reaction produces $O=^{\bullet}C–O–COO^{-}$ (equation 1.7), and the subsequent reduction of the product in equation (1.8) yields carbon monoxide and carbonate.

$$CO_2^{-\bullet}{}_{(ads)} + CO_{2\,(aq)} \longrightarrow O=^{\bullet}C—O—COO^{-}{}_{(ads)} \qquad \textit{(Equation 1.7)}$$

$$O=^{\bullet}C—O—COO^{-}{}_{(ads)} + e^{-} \longrightarrow CO_{(g)} + CO_3^{2-}{}_{(aq)} \qquad \textit{(Equation 1.8)}$$

In CO_2 reduction, the electrolyte is a crucial factor to consider. The chosen electrolyte must not compromise the quality of the products formed. The hydrogen evolution reaction (HER) is viewed as a competing reaction that can elevate the pH of the electrolyte and inhibit the active sites on the electrode surface. This is because a higher pH increases the concentration of hydroxide ions (OH^{-}) in the solution. These ions can react with protons (H^{+}) to form hydrogen gas (H_2), potentially limiting the efficiency of CO_2 reduction. Therefore, careful control of the solution pH is important in optimising the CO_2 reduction process. In addition, the choice of the catalyst remains extremely important as it needs to promote CO_2 reduction while suppressing hydrogen evolution reaction, requiring the catalyst to facilitate multiple electron transfers at a low overpotential.[110] It should be noted that the Faraday efficiency increases when the selectivity towards the target product improves, and the potential requirement decreases due to the addition of a catalyst. Faraday Efficiency, also referred to as Faradaic efficiency or Faradaic yield, quantifies the effectiveness of electron transfer in an electrochemical reaction to produce a specific product. It essentially measures how efficiently the supplied electrons in the electrochemical process contribute to the desired chemical reaction.[111] The Faradaic efficiency of the various products in CO_2 reduction can be calculated using Equation 1.9

$$Faradaic\ efficiency\ (\%) = \frac{m_{product} \times n \times F}{Q} \times 100 \qquad (Equation\ 1.9)$$

Where $m_{product}$ = moles of the reduction products, n = number of electrons needed for the formation of the product, F = Faradaic constant (96485 C mol^{-1}) of electrons, Q = total charge in coulombs passed across the electrode for the duration of the electrolysis.

1.3.5 Benzonitrile

Anion radicals of aromatic nitriles such as benzonitrile, which are generated electrochemically, have a unique characteristic that boosts the reduction process of carbon dioxide.[112] Benzonitrile is a chemical compound represented by the formula $C_6H_5(CN)$. Its discovery was first documented by Hermann Fehling in 1844. He identified the compound as a result of the thermal dehydration of ammonium benzoate. He inferred its structure, as illustrated in Figure 1.7, from the already established analogous reaction of ammonium formate, producing hydrogen cyanide (formonitrile). He was also the one to introduce the term benzonitrile, which subsequently became the name for the entire group of nitriles.[113]

This aromatic organic compound is a colourless liquid that emits a sweet, bitter almond scent. It is a useful solvent and a versatile starting material for many derivatives. The benzonitrile ligands can be easily replaced by stronger ligands, making benzonitrile complexes valuable synthetic intermediates.[114]

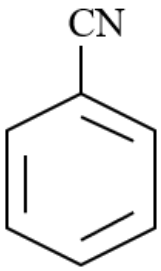

Figure 1.7: Benzonitrile.

Subsequently, the use of benzonitrile as a homogeneous catalyst that improves selectivity to oxalates in some organic solvents has been reported.[112,115] Homogeneous catalysis is a process in which the reactants and the catalyst are in the same phase, usually in solution. During electrochemical reactions, the electrocatalyst helps in the electron transfer on the electrode and facilitates the reaction on the electrode surface. The electrochemical reduction of CO_2 using benzonitrile as a catalyst is represented thus (equation 1.10):

$$2CO_2 + 2H^+ + 2e^- \xrightarrow[C_6H_5(CN)]{} H_2C_2O_4 \qquad (Equation\ 1.10)$$

The mechanism of the electrochemical process involves the formation of a relatively stable benzonitrile anion radical (BN•⁻) through a one-electron reduction process (equation 1.11).

$$BN + e^- \rightleftharpoons BN^{\bullet -} \qquad (Equation\ 1.11)$$

The BN•⁻ anion radical formed in the CO2-saturated environment then react with CO_2 molecule to facilitate the formation of a $CO_2^{-}\bullet$ anion radical (equation 1.12).

$$BN^{\bullet -} + CO_2 \rightleftharpoons BN + CO_2^{-}\bullet \qquad (Equation\ 1.12)$$

The anion radical formed eventually undergoes dimerisation to form oxalate ions ($C_2O_4^{2-}$), which in turn get protonated to form oxalic acid, as shown in equations 1.13 and 1.14 respectively.

$$2\ CO_2^{-}\bullet \longrightarrow C_2O_4^{2-} \qquad (Equation\ 1.13)$$

$$C_2O_4^{2-} + 2H^+ \longrightarrow H_2C_2O_4 \qquad (Equation\ 1.14)$$

1.3.6 Description of Reaction Mechanism of CO_2 Reduction on Pb Electrode

The reaction mechanism for the production of oxalate on a Pb electrode in an organic solvent has been described by Eneau-Innocent.[18] Scheme 1.2 provides an overview of the reaction steps for oxalate formation on lead in propylene carbonate (PC). The mechanism consists of three basic steps; step I starts with forming the CO_2 anion on the lead electrode, which reacts to form oxalate in step II. Finally, the bond between oxalate and lead is broken in step III, forming an oxalate anion.

Step I

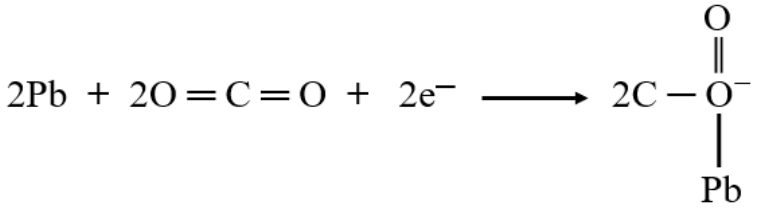

Step II

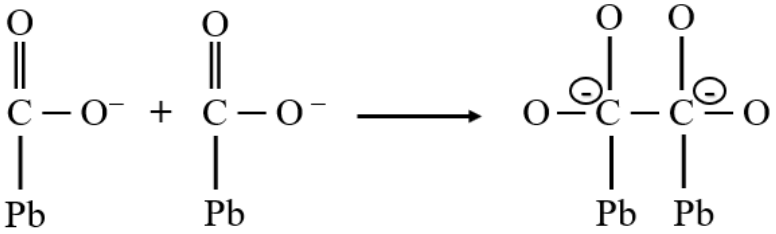

Step III

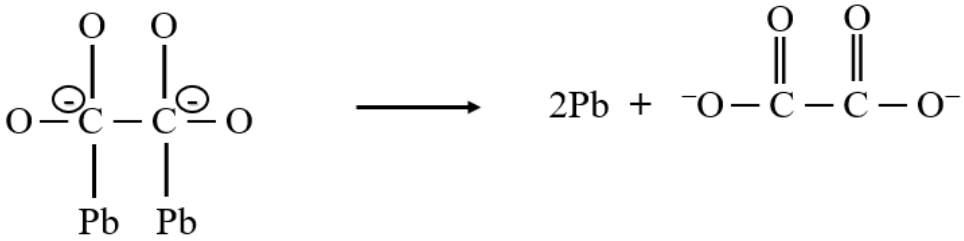

Scheme 1.2: The mechanism for forming oxalate on a lead electrode in propylene carbonate as described by Eneau-Innocent et al.[18]

According to the literature,[93,116] when CO_2 reduction is conducted in an aprotic organic medium like acetonitrile, dimethylformamide or propylene carbonate, it facilitates the orientation of CO_2 reduction towards dimerisation, whereas the presence of H_2O molecules triggers the hydrogenation reaction, resulting in the production of formate, as illustrated in Figure 1.8.

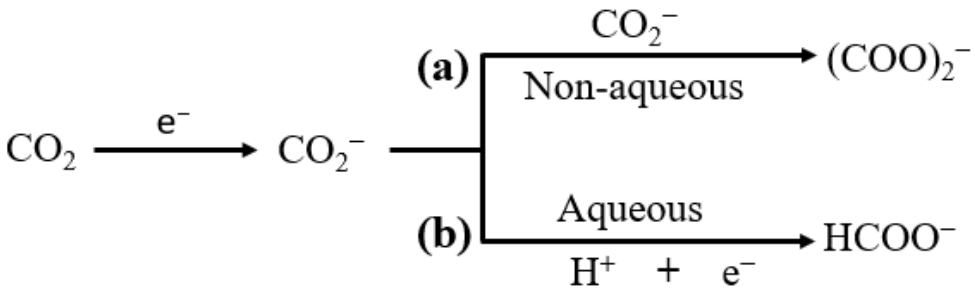

Figure 1.8: Reaction pathways in the electrochemical reduction of CO_2 in (a) non-aqueous and (b) aqueous medium as described by Ikeda et al.[73]

Propylene carbonate was selected due to its capacity to dissolve CO_2 in large amounts (0.14 mol L^{-1} at 25 °C, 1 bar),[18] extensive electrochemical window, and comparatively low toxicity relative to other aprotic solvents.

1.4 Raw Materials and Routes to Oxalic Acid Synthesis

Oxalic acid can be synthesised through six primary pathways. The raw materials are: (a) alkali formate, (b) propylene, (c) CO_2, (d) CO, (e) ethylene glycol and (f) carbohydrates, as illustrated in Scheme 1.3.

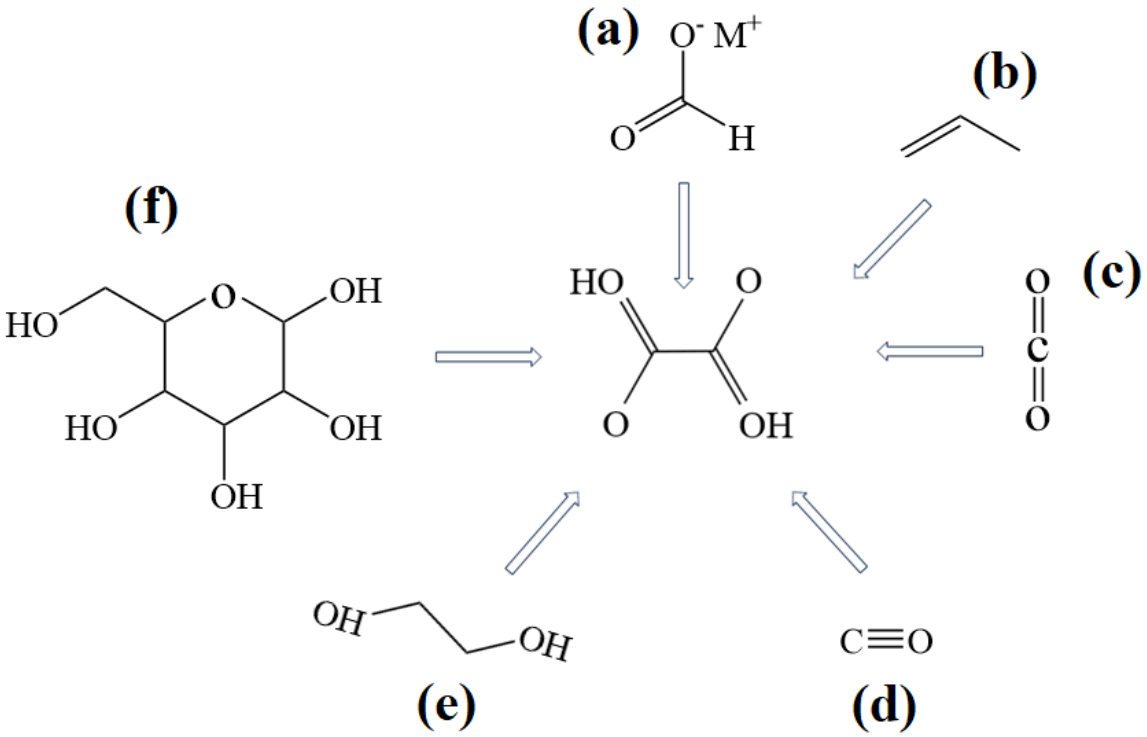

Scheme 1.3: The six raw materials and routes for the production of oxalic acid as described by Schuler et al.[72]

Some of these methods are currently employed in commercial applications, while others represent recent advances. Enhancing sustainability can be achieved by either replacing fossil-based building blocks with renewable alternatives or creating novel, sustainable pathways to produce oxalic acid.[72] Given the abundance of CO_2 in the atmosphere, utilising it to produce oxalic acid and other valuable fuels could serve as an economical and sustainable source of carbon in the synthesis of valuable chemicals.

Bergmann identified the earliest method for producing oxalic acid in 1776. This process involves oxidising biomass, specifically the carbohydrates it contains, into oxalic acid using nitric acid.[117] Biomass refers to plant material that is produced from the photosynthetic transformation of CO into sugars and other organic components.[118] A significant issue with the widespread use of biomass as a raw material in the chemical industry is its potential to compete with food production, especially when the crops used are grown on agricultural land or are food sources themselves, like corn or wheat.
Additionally, biomass can serve as a raw material for creating other precursors to oxalic acid. These include CO (through gasification), CO_2 (via fermentation or combustion), alkali formate, and ethylene glycol (through bio-ethylene or direct hydrogenolysis).[72]

Oxalic acid can be derived from fossil carbon through four distinct pathways, illustrated in Scheme 1.4, representing all the possible fossil carbon-based pathways, including oxidative pathways via naphtha-derived ethylene and propylene; (a) naphtha can undergo conversion to ethylene glycol (via ethylene), subsequently oxidised to oxalic acid; (b) propylene, obtained through naphtha cracking, can be transformed into oxalic acid; (c) fossil carbon undergoes gasification to produce CO, which can be further converted to oxalic acid using the dialkyl oxalate process; and alternatively, (d) CO can be transformed into formate, and subsequently, oxalic acid is generated through formate coupling followed by acidification. This synthetic strategy was first introduced by Gallently[119] in 1881, who produced oxalic acid by heating paraffin in the presence of HNO_3. The major limitation of this process is multiple reaction stages, resulting in the loss of some products and the use of harsh oxidants in some instances. The difficulties and inefficiency associated with using fossil carbon could be addressed by using CO_2 as a feedstock in producing oxalic acid.

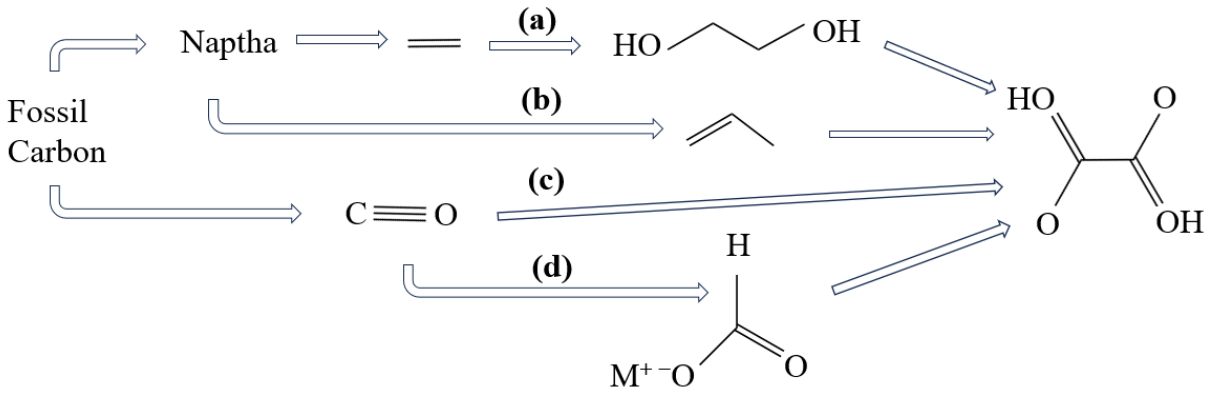

Scheme 1.4: The four pathways for converting fossil carbon to oxalic acid as described by Schuler et al.[72]

Some sources of CO_2 emissions, such as the production of cement, steel, or ammonia, are unavoidable or a carbon source is strongly preferred despite the proposal of alternative hydrogen-based processes. Therefore, it is particularly important to devise a means of combating or utilising the CO_2 from the production processes. However, for industries to embrace CO_2 as a raw material, it is also necessary for the processes (along with regulations or taxes) to be market-competitive to challenge and reduce reliance on fossil fuels.[120,121]

Oxalic acid synthesis from CO_2 can be achieved through four primary pathways, as illustrated in Scheme 1.5: (a) direct conversion of CO_2 to alkali oxalate, (b) generation of a metal formate intermediate from the electrocatalytic or photocatalytic reduction of CO_2, followed by conversion to oxalic acid; (c) utilisation of CO and the dialkyl oxalate process, and (d) the fourth route via ethylene glycol and subsequent oxidation, although this is not commonly practised since ethylene glycol is typically derived from oxalic acid rather than the reverse.[72]

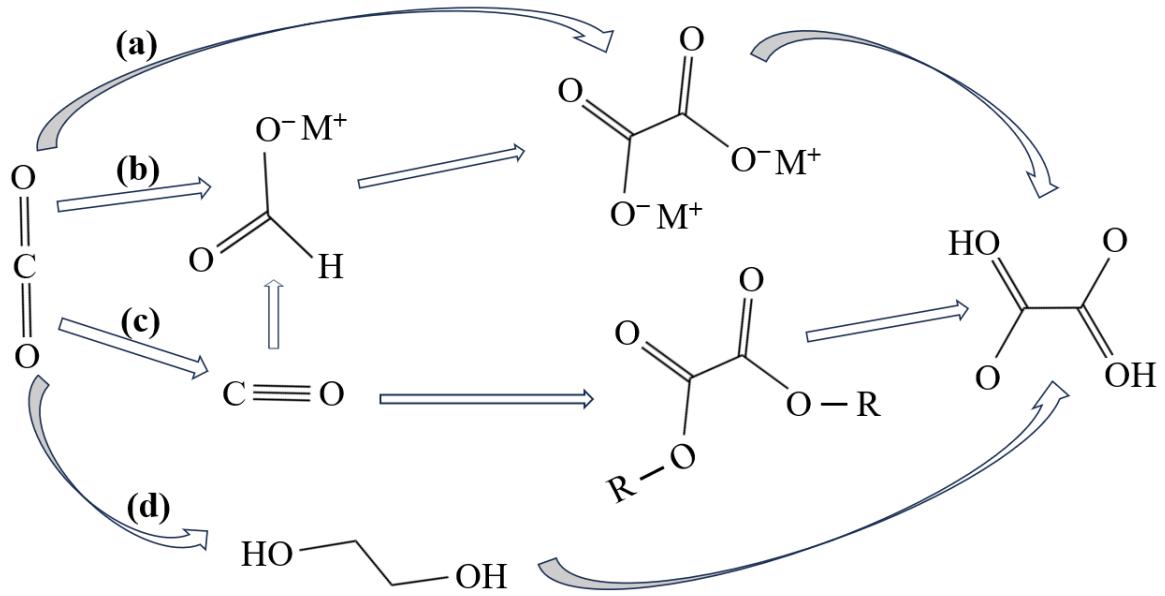

Scheme 1.5: The four main pathways for producing oxalic acid from CO_2, as described by Schuler et al.[72]

1.5 Electrochemical Reduction of Oxalic Acid

The process of electrochemical reduction involves oxalic acid ($H_2C_2O_4$) being transformed at the electrode's surface through reduction reactions when an electric potential is applied. This leads to the formation of important chemicals such as glyoxylic acid (GA) and glycolic acid (GC). The significance of this reaction spans across multiple disciplines, from organic synthesis and environmental chemistry to energy storage solutions.

1.5.1 Overview of Electrochemical Reduction of Oxalic Acid

Many individual researchers and research groups have investigated the electrochemical reduction of aqueous oxalic acid solutions. The pioneer references in this direction appear to be a patent by Royer[122] and a subsequent study by Tafel[123], both of whom experimented with the process.

Further comprehensive studies were carried out by Baur,[124] and Mohschulz,[125] who patented a process which employed a graphite cathode and an oxalic acid/sulfuric acid mixture in ethanol and water. They reported a yield of 60% by weight at a current density of 0 - 0.2 A/cm^2 and a temperature of 5 - 10 °C. Operation with lead and mercury cathodes gave yields of 79% and 82-85%, respectively. An almost identical process to Mohrschultz's was reported by Nakata,[126] who used a mercury cathode and claimed a yield of 90%.

Furthermore, most of the subsequent research has been concerned with the mechanism of oxalic acid reduction. Listopadov *et al.*[127] used a variety of cathodes including lead, cadmium, thallium amalgam and mercury in the electrochemical reduction of oxalic acid and considered that the rate-determining step was the reduction of hydrogen ions activated in the double layer. However, contrary opinions were held by Florianovich *et al.*,[128] who proposed that the slow step was the addition of an electron to an oxalic acid molecule.

Smialowski *et al.*[129] reported investigations with a lead cathode and concluded that the reduction of oxalic acid was dependent on the hydrogen evolution overpotential, the yield of glyoxylic acid being raised by the addition of sodium sulfate to the electrolyte to increase the hydrogen overpotential.

Pickett *et al.*[130] investigated the formation of glyoxylic acid by the electrochemical reduction of oxalic acid/sulfuric acid aqueous solutions at various temperatures and cathode potentials using lead electrodes. They reported that, for a given quantity of electricity passed, greater current efficiencies were obtained at higher electrode potentials and lower temperatures. It was reported that the current efficiency decreased with an increasing quantity of electricity passed.

In the recent past, different types of titanium-based electrodes were examined with various catalysts by many researchers.[131–134] Titanium-based electrodes are considered the material of choice to electrochemically reduced oxalic acid because of their durability, cost-effectiveness, and non-toxicity. Nevertheless, there is still room for improvement in the processes as the conversion efficiencies are considerably low.

1.5.2 Reaction Scheme for Electrochemical Reduction of Oxalic Acid

The process of electrochemically reducing oxalic acid typically occurs in a low-temperature, acidic environment using hydrogen electrodes with a high overvoltage or alongside a protonic mineral acid like H_2SO_4, facilitated by an ion-exchange membrane.[43] The conversion of oxalic acid into glyoxylic and glycolic acids through this method involves the transfer of two and four electrons, respectively, as illustrated in Scheme 1.6 (Gimenez et al., 1987).[135]

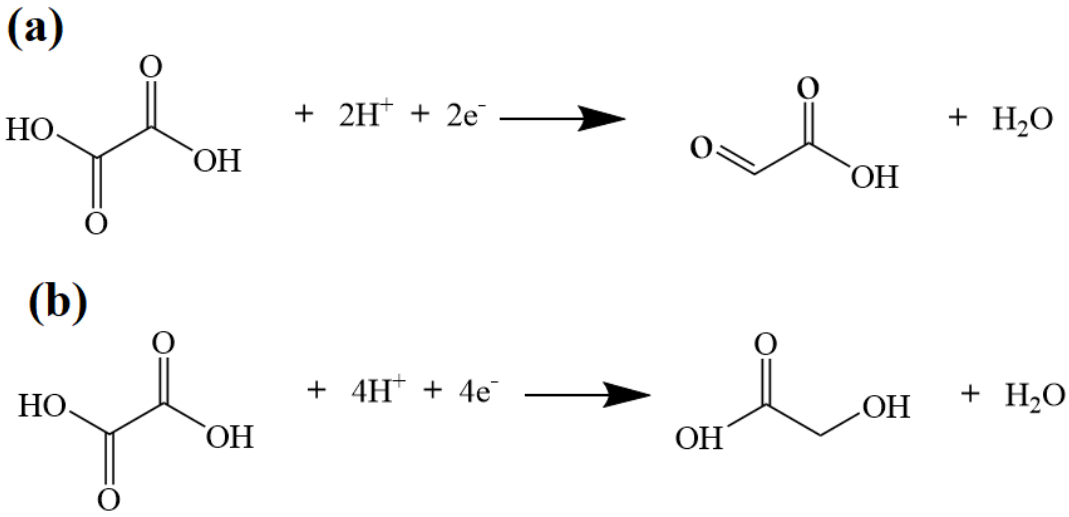

Scheme 1.6: The reaction scheme for the electrochemical reduction of oxalic acid to (a) glyoxylic acid and (b) glycolic acid as described by Eggins et al.[43]

1.5.3 Applications of Glyoxylic Acids and Glycolic Acids

Glyoxylic acid is the primary reduction product of oxalic acid, which serves as a crucial carbon component for many industrially significant organic molecules. It plays a key role in the manufacturing processes of agrochemicals, fragrances, cosmetics ingredients, pharmaceutical intermediates, and polymers.[136] Glyoxylic acid is directly applied in personal care products as a neutralising agent, especially in hair straightening products like shampoos, conditioners, lotions, and creams, ranging from 0.5% to 10%.

When the aldehyde function of glyoxylic acid is further reduced, it results in glycolic acid. This acid is a valuable intermediate for organic synthesis, participating in reactions such as oxidation-reduction, esterification, and long-chain polymerisation. It is a monomer creating polyglycolic acid and other biocompatible copolymers like poly lactic-co-glycolic acid (PLGA).[137] Glycolic acid is used in the textile industry as a dyeing and tanning agent, as a flavouring agent, and as a preservative in food processing. It is also used as a skincare agent in the pharmaceutical industry and in adhesives and polymers.[138,139] Glycolic acid is frequently incorporated in emulsion polymers, solvents, and additives for ink and paint to enhance flow properties and provide gloss. From a commercial standpoint, significant glycolic acid derivatives include the methyl and ethyl esters, which can be readily distilled, unlike the parent acid. The butyl ester is preferred for some varnishes due to its non-volatile nature and excellent dissolving properties.[72]

1.6 Sonoelectrochemical Reactions

Sonoelectrochemical reactions combine ultrasound and electrochemical processes to enhance chemical reactions. This synergy significantly improves reaction rates, yields, and selectivities. The technique applies high-frequency sound waves to create cavitation bubbles in the solution. The collapse of these bubbles generates localized hot spots with high temperatures and pressures, along with intense shear forces and shock waves. These effects, in conjunction with the electrical energy (applied potential) supplied to the system, drive redox reactions at the electrode-solution interface, thus enhancing the electrochemical reaction's efficiency.[140]

1.6.1 Application of Ultrasound Parameters for Efficient Sonoelectrochemical CO_2 Reduction

Ultrasonic assistance in electrochemistry offers several benefits, including the activation and purification of electrode surfaces, the mitigation of gas bubble accumulation at the electrode interface, the prevention of potential-induced damage, and the augmentation of mass transport via acoustic streaming and cavitation phenomena.[140] Previous studies have showcased the significant impact of ultrasound on various electrochemical reactions, highlighting its potential as a tool for enhancing reaction kinetics and selectivity.[141] Furthermore, the synergistic effects of ultrasound and electrochemistry have been widely recognised. Ultrasonic irradiation can lead to the formation of reactive species and localised heating, which can facilitate electron transfer processes and alter reaction pathways.[141,142] Additionally, ultrasound-induced cavitation events can promote the dispersion of reactants and enhance mass transport, thereby improving the overall efficiency of electrochemical processes.[72,143] Despite these potential advantages, there is limited information and understanding of how the various ultrasonic parameters influence CO_2 reduction. Consequently, this study investigates the electrochemical reduction of CO_2 under varying ultrasound-assisted conditions, including frequency and power levels, at ambient temperatures (~25°C). Through systematic exploration of these parameters, we aim to elucidate their impact on reaction efficiency, selectivity, and underlying mechanisms. Such insights are crucial for optimising CO_2 electroreduction processes and advancing the development of sustainable energy technologies. Moreover, the findings of this study may contribute to the broader understanding of ultrasound-assisted electrochemistry and its potential applications in other catalytic reactions and energy conversion processes. The application and evaluation of different ultrasound parameters for an efficient sonoelectrochemical CO_2 reduction are presented in chapter 5 of this thesis.

1.7 Aim and Objectives

This research aims to electrochemically convert CO_2 to oxalic acid and other useful C_2 chemicals.

The objectives are:

I. To electrochemically reduce CO_2 in organic solvent (propylene carbonate) in order to suppress hydrogen evolution which tends to prevail in an aqueous medium.

II. To use a combination of propylene carbonate and benzonitrile as a homogeneous catalyst to improve the selectivity of CO_2 reduction to oxalate/oxalic acid. To the best of our knowledge, this is the first time that the catalytic effect of benzonitrile would be exploited in propylene carbonate to electrochemically reduce CO_2.

III. To determine the conversion efficiency and product distribution during the electrochemical reduction of CO_2 and oxalic acid conversion to glyoxylic and glycolic acid.

IV. To optimise the operating conditions, such as applied potential, catalytic requirement, choice of electrodes, etc., for efficient electrochemical reduction reaction.

V. To evaluate the synergistic effects of ultrasound and electrochemistry (sonoelectrochemistry) in enhancing the electrochemical reduction of CO_2.

1.8 Conclusion

The conversion of CO_2 into industrially relevant products is a globally significant area of research, driven by its potential as a sustainable feedstock and concerns about escalating atmospheric CO_2 concentrations with their attendant catastrophic consequences. Electrochemical techniques stand out as particularly attractive in this context, offering greater perspective and more customisable reaction pathways compared to other methods of CO_2 conversion. The pursuit of electrochemical approaches reflects a proactive response to sustainable sources of some organic chemicals and addresses the pressing environmental challenges associated with rising CO_2 levels.

In this chapter, we have attempted to introduce the concept of electrochemical reduction of CO_2 (an environmental pollutant) to useful products. The concept of CO_2 conversion and utilisation aligns with the principles of a circular economy, where waste is minimised, and resources are utilised efficiently. It presents an interdisciplinary approach that combines chemistry, engineering, and environmental science.

We also aim to investigate the suitable medium for CO_2 reduction to oxalates/oxalic acid. The finding reveals that most of the early research in this area was conducted in aqueous medium, albeit the efficiency of the process is low due to the competing hydrogen evolution reaction (HER). Although subsequent researchers reported the successful reduction of CO_2 to oxalic acid in organic solvents with improved efficiency,[144 45 145] compared to aqueous media. However, the issue of the high energy requirement needed in the process is still challenging and needs to be addressed by using a suitable catalyst that could reduce the potential requirement. In this regard, benzonitrile was applied to the organic solvent to catalyse the process and make it sustainable by improving the overall efficiency. Moreover, several potentials were applied to determine the optimal potential at which the electrochemical reduction reactions are most efficient.

Oxalic acid is a versatile product with a wide range of uses. Consequently, the electrochemical conversion of oxalic acid into glyoxylic and glycolic acid is particularly intriguing, as these are high-value chemicals with promising market potential. However, the economic feasibility of the process is hindered by a low yield due to the inadequate percentage conversion of oxalic acid in the process. To improve the efficiency, we aim to investigate the catalytic influence of the native oxide of a titanium electrode (Ti/Ti_xO_y) in the reduction of oxalic acid.

To sum up, in this chapter, we provide a comprehensive study of the current literature on the electrochemical reduction of CO_2 to oxalic acid and explore a sustainable approach to converting CO_2 into other valuable chemical products. We have identified a choice of an organic solvent (propylene carbonate) and the use of benzonitrile as a catalyst to enhance the efficiency and selectivity of oxalic acid production. Propylene carbonate has been proposed as a suitable organic solvent because it is relatively cheap and non-toxic. In addition, dimethylformamide (DMF) is toxic and will soon face heavy restrictions in many countries. In contrast, acetonitrile is too volatile to endure prolonged electrolysis.

In another conceptual approach, we intend to investigate the synergistic effects of ultrasound and electrochemistry in the sonoelectrochemical reduction of CO_2 into useful chemicals. Integrating ultrasonic waves and electrochemical methods is anticipated to offer substantial benefits compared to conventional electroanalytical techniques. This study contributes to the broader field of CO_2 utilisation and sustainable synthesis of industrially relevant compounds.

1.9 References

1 J. Setzer and C. Higham, *Glob. Trens Clim. Chang. Litig.*, 2021, **2**, 37 – 39.

2 J. Z. Jinli Qiao, Yuyu Liu, *Electrochemical reduction of carbon dioxide : fundamentals and technologies*, (1st ed.), CRC Press, 2016, 5 – 45.

3 B. Koerner and J. Klopatek, *Environ. Pollut.*, 2002, **116**, 45–51.

4 T. M. Gür, *Prog. Energy Combust. Sci.*, 2022, **89**, 100965.

5 C. Song, *ACS Symp. Ser.*, 2002, **809**, 1–30.

6 P. Dlugokencky, E., & Tans, *Earth System Research Laboratory (NOAA/ESRL)*, 2018.

7 D. Mazza and E. Canuto, 2023, 1 - 32, https://arxiv.org/abs/2209.01911v2, accessed on 22-11-2023

8 M. Wang, A. Lawal, P. Stephenson, J. Sidders and C. Ramshaw, *Chem. Eng. Res. Des.*, 2011, **89**, 1609–1624.

9 E. Alper and O. Yuksel Orhan, *Petroleum*, 2017, **3**, 109–126.

10 A. Gulzar, A. Gulzar, M. B. Ansari, F. He, S. Gai and P. Yang, *Chem. Eng. J. Adv.*, 2020, **3**, 100013.

11 P. Styring, S. McCord and S. Rackley, *Carbon dioxide utilization*, 2023, 391-413.

12 D. T. Whipple and P. J. A. Kenis, *J. Phys. Chem. Lett.*, 2010, **1**, 3451–3458.

13 D. Chu, G. Qin, X. Yuan, M. Xu, P. Zheng and J. Lu, *ChemSusChem Chem. Sustain. Energy Mater.*, 2008, **1**, 205–209.

14 N. S. Spinner, J. A. Vega and W. E. Mustain, *Catal. Sci. Technol.*, 2012, **2**, 19–28.

15 Y. Chen, C. W. Li and M. W. Kanan, *J. Am. Chem. Soc.*, 2012, **134**, 19969–19972.

16 E. E. Barton, D. M. Rampulla and A. B. Bocarsly, *J. Am. Chem. Soc.*, 2008, **130**, 6342–6344.

17 B. A. Rosen, A. Salehi-Khojin, M. R. Thorson, W. Zhu, D. T. Whipple, P. J. A. Kenis and R. I. Masel, *Science*, 2011, **334**, 643–644.

18 B. Eneau-Innocent, D. Pasquier, F. Ropital, J.-M. Léger and K. B. Kokoh, *Appl. Catal. B Environ.*, 2010, **98**, 65–71.

19 M. Moura de Salles Pupo and R. Kortlever, *ChemPhysChem*, 2019, **20**, 2926–2935.

20 H. Hashiba, L. C. Weng, Y. Chen, H. K. Sato, S. Yotsuhashi, C. Xiang and A. Z. Weber, *J. Phys. Chem. C*, 2018, **122**, 3719–3726.

21 K. Izutsu, *Electrochem. Nonaqueous Solut.*, 2002, 1–24.

22 S. Liang, N. Altaf, L. Huang, Y. Gao and Q. Wang, *J. CO_2 Util.*, 2020, **35**, 90–105.

23 R. Lin, J. Guo, X. Li, P. Patel and A. Seifitokaldani, *Catalysts*, 2020, **10**, 473.

24 M. Li, M. N. Idros, Y. Wu, T. Burdyny, S. Garg, X. S. Zhao, G. Wang and T. E. Rufford, *J. Mater. Chem. A*, 2021, **9**, 19369–19409.

25 W. Choi, D. H. Won and Y. J. Hwang, *J. Mater. Chem. A*, 2020, **8**, 15341–15357.

26 E. Ruiz-López, J. Gandara-Loe, F. Baena-Moreno, T. R. Reina and J. A. Odriozola, *Renew. Sustain. Energy Rev.*, 2022, **161**, 112329.

27 S. Petrovic, *Electrochem. Crash Course Eng.*, 2021, 3–10.

28 R. E. Vos, K. E. Kolmeijer, T. S. Jacobs, W. Van Der Stam, B. M. Weckhuysen and M. T. M. Koper, *ACS Catal.*, 2023, **13**, 8080–8091.

29 M. König, J. Vaes, E. Klemm and D. Pant, *iScience*, 2019, **19**, 135–160.

30 S. Garg, M. Li, A. Z. Weber, L. Ge, L. Li, V. Rudolph, G. Wang and T. E. Rufford, *J. Mater. Chem. A*, 2020, **8**, 1511–1544.

31 D. M. Weekes, D. A. Salvatore, A. Reyes, A. Huang and C. P. Berlinguette, *Acc. Chem. Res.*, 2018, **51**, 910–918.

32 N. Solutions, E. Edition, K. I. Copyright, W. V. Gmbh, and W. Isbn, "*Part One Fundamentals of Chemistry in Nonaqueous Solutions: Electrochemical Aspects*," 2009.

33 K. Praveen and M. Sethumadhavan, *Int. Conf. Adv. Comput. Commun. Informatics, ICACCI 2017*, 2017, 219–222.

34 C. Delacourt, C. Delacourt, P. L. Ridgway, J. B. Kerr and J. Newman, *Journal of The Electrochemical Society,* 2008, **115**, B43 - B49.

35 D. Sebastián, A. Palella, V. Baglio, L. Spadaro, S. Siracusano, P. Negro, F. Niccoli and A. S. Aricò, *Electrochim. Acta*, 2017, **241**, 28–40.

36 L. Fan, C. Xia, F. Yang, J. Wang, H. Wang and Y. Lu, *Sci. Adv.*, 2020, **6**, 1–18.

37 D. T. Whipple, E. C. Finke and P. J. A. Kenis, *Electrochem. Solid-State Lett.*, 2010, **13**, 3.

38 A. S. Hollinger, R. J. Maloney, R. S. Jayashree, D. Natarajan, L. J. Markoski and P. J. A. Kenis, *J. Power Sources*, 2010, **195**, 3523–3528.

39 S. Nitopi, E. Bertheussen, S. B. Scott, X. Liu, A. K. Engstfeld, S. Horch, B. Seger, I. E. L. Stephens, K. Chan, C. Hahn, J. K. Nørskov, T. F. Jaramillo and I. Chorkendorff, *Chem. Rev.*, 2019, **119**, 7610–7672.

40 J. Schneider, H. Jia, J. T. Muckerman and E. Fujita, *Chem. Soc. Rev.*, 2012, **41**, 2036–2051.

41 Y. Hori, *Mod. Asp. Electrochem.*, 2008, **42** 89–189.

42 J. Qiao, Y. Liu, F. Hong and J. Zhang, *Chem. Soc. Rev.,* 2014, **43**, 631.

43 B. R. Eggins, C. Ennis, R. McConnell and M. Spence, *J. Appl. Electrochem.*, 1997, **27**, 706–712.

44 H. R. M. Jhong, S. Ma and P. J. Kenis, *Curr. Opin. Chem. Eng.*, 2013, **2**, 191–199.

45 V. Boor, J. E. B. M. Frijns, E. Perez-Gallent, E. Giling, A. T. Laitinen, E. L. V. Goetheer, L. J. P. Van Den Broeke, R. Kortlever, W. De Jong, O. A. Moultos, T. J. H. Vlugt and M. Ramdin, *Ind. Eng. Chem. Res.*, 2022, **61**, 14837–14846.

46 M. Jitaru, *J. Univ. Chem. Technol. Metall.*, 2007, **42**, 333–344.

47 H. Guzmán, M. A. Farkhondehfal, K. R. Tolod, S. Hernández and N. Russo, *Solar Hydrogen Production: Processes, Systems and Technologies*, 2019, 365-418.

48 I. Ganesh, *Renew. Sustain. Energy Rev.*, 2016, **59**, 1269–1297.

49 F. R. Keene, C. Creutz and N. Sutin, *Coord. Chem. Rev.*, 1985, **64**, 247–260.

50 H. A. Schwarz and R. W. Dodson, *J. Phys. Chem.*, 1989, **93**, 409–414

51 P. Akhter, M. A. Farkhondehfal, S. Hernández, M. Hussain, A. Fina, G. Saracco, A. U. Khan and N. Russo, *J. Environ. Chem. Eng.*, 2016, **4**, 3934–3953.

52 J. Bard Allen and R. Faulkner Larry, *Russian Journal of Electrochemistry,*2002, 38 (**12**), 1364–1365.

53 A. M. Appel, J. E. Bercaw, A. B. Bocarsly, H. Dobbek, D. L. Dubois, M. Dupuis, J. G. Ferry, E. Fujita, R. Hille, P. J. A. Kenis, C. A. Kerfeld, R. H. Morris, C. H. F. Peden, A. R. Portis, S. W. Ragsdale, T. B. Rauchfuss, J. N. H. Reek, L. C. Seefeldt, R. K. Thauer and G. L. Waldrop, *Chem. Rev,* 2013, 113 (**8**) 6621–6658,

54 M. Aresta, A. Dibenedetto and A. Angelini, *Chem. Rev.* 2014, 114, (**3**), 1709–1742.

55 L. Wu, Q. Liu, I. Fleischer, R. Jackstell and M. Beller, *Nat. Commun.*, 2014, **5**, 1–6.

56 J. Echeverría and J. Jover, *European J. Org. Chem.*, 2022, 26–31.

57 W. M. Ren, Z. W. Liu, Y. Q. Wen, R. Zhang and X. B. Lu, *J. Am. Chem. Soc.*, 2009, **131**, 11509–11518.

58 Q. Liu, L. Wu, R. Jackstell and M. Beller, *Nat. Commun.*, 2015, **6**, 5933.

59 K. Adachi, K. Ohta and T. Mizuno, *Sol. Energy*, 1994, **53**, 187–190.

60 L. Wang, L. Wang, J. Zhang, X. Liu, H. Wang, W. Zhang, Q. Yang, J. Ma, X. Dong, S. J. Yoo, J. G. Kim, X. Meng and F. S. Xiao, *Angew. Chemie - Int. Ed.*, 2018, **57**, 6104–6108.

61 Y. Ni, Z. Chen, Y. Fu, Y. Liu, W. Zhu and Z. Liu, *Nat. Commun.*, 2018, **9**, 1–7.

62 A. J. Morris, G. J. Meyer and E. Fujita, *Acc. Chem. Res.*, 2009, **42**, 1983–1994.

63 W. H. Wang, Y. Himeda, J. T. Muckerman, G. F. Manbeck and E. Fujita, *Chem. Rev.*, 2015, **115**, 12936–12973.

64 H. Takeda, C. Cometto, O. Ishitani and M. Robert, *ACS Catal.*, 2017, **7**, 70–88.

65 F. Khamespanah, M. Marx, D. B. Crochet, U. R. Pokharel, F. R. Fronczek, A. W. Maverick and M. Beller, *Nat. Commun.*, 2021, **12**, 10–13.

66 B. C. Nelson, G. F. Rockwell, T. Campfield, P. O'Grady, R. M. Hernandez and S. A. Wise, *Anal. Chim. Acta*, 2000, **410**, 1–10.

67 W. Chai and M. Liebman, *J. Food Compos. Anal.*, 2005, **18**, 723–729.

68 Y. Yamazaki, H. Takeda and O. Ishitani, *J. Photochem. Photobiol. C*, 2015, **25**, 106–137.

69 R. Francke, B. Schille and M. Roemelt, *Chem. Rev.*, 2018, **118**, 4631–4701.

70 H. Sale, G. R. Ubbara and M. D. Symes, *Sustain. Energy Fuels*, 2023, **7**, 5093–5100.

71 M. Marx, H. Frauendorf, A. Spannenberg, H. Neumann and M. Beller, *JACS Au*, 2022, **2**, 731–744.

72 E. Schuler, M. Demetriou, N. R. Shiju and G. J. M. Gruter, *ChemSusChem*, 2021, **14**, 3636–3664.

73 M. Valderrama, R. van Putten, G. Grutter, *European Polymer Journal*,2019, **119**, 445 -468.

74 D. A. Lote, *Int. J. Electron. Electr. Eng.*, 2014, **7**, 341–346.

75 D. A. Tyssee, J. H. Wagenknecht, M. M. Baizer and J. L. Chruma, *Tetrahedron Lett.*, 1972, **13**, 4809–4812.

76 A. Gennaro, A. A. Isse, M. G. Severin, E. Vianello, I. Bhugun and J. M. Savéant, *J. Chem. Soc. - Faraday Trans.*, 1996, **92**, 3963–3968.

77 C. Amatore and J. M. Savéant, *J. Am. Chem. Soc.*, 1981, **103**, 5021–5023.

78 I. Kaname, I. Shoichiro, I. Takaya, N. Akihiko, *Eletrochem*, 1982, **50**, 463–469.

79 Y. Hori, R. Takahashi, Y. Yoshinami and A. Murata, *J. Phys. Chem. B*, 1997, **101**, 7075–7081.

80 J. Gressin, D. Michelet, L. Nadjo, J. Savéant, *Nouv. J. Chim.*, 1979, 545.

81 H. Ito, S. Ikeda, T. Iida, *Denki Kagaku*, 1981, **49**, 106.

82 B. R. Eggins, E. M. Brown, E. A. McNeill and J. Grimshaw, *Tetrahedron Lett.*, 1988, **29**, 945–948.

83 B. B. Von U. Kaiser and E. Heitz, *Phys. Chem*, 1973, **77**, 818.

84 M. Todoroki, K. Hara, A. Kudo and T. Sakata, *J. Electroanal. Chem.*, 1995, **394**, 199–203.

85 G. Centi, G. Iaquaniello and S. Perathoner, *BMC Chem. Eng.*, 2019, **1**, 1–16.

86 S. Perathoner and G. Centi, *Catal. Today*, 2019, **330**, 157–170.

87 M. A. Murcia Valderrama, R. J. van Putten and G. J. M. Gruter, *Eur. Polym. J.*, 2019, **119**, 445–468.

88 E. Jalali, S. Maghsoudi and E. Noroozian, *Sci. Rep.*, 2020, **10**, 1–10.

89 S. Subramanian, K. R. Athira, M. Anbu Kulandainathan, S. Senthil Kumar and R. C. Barik, *J. CO_2 Util.*, 2020, **36**, 105–115.

90 M. König, S. H. Lin, J. Vaes, D. Pant and E. Klemm, *Faraday Discuss.*, 2021, **230**, 360–374.

91 F. Murrieta-Guevara, A. Romero-Martinez and A. Trejo, *Fluid Phase Equilib.*, 1988, **44**, 105–115.

92 T. Fan, W. Ma, M. Xie, H. Liu, J. Zhang, S. Yang, P. Huang, Y. Dong, Z. Chen and X. Yi, *Cell Reports Phys. Sci.*, 2021, **2**, 100353.

93 S. Ikeda, T. Takagi and K. Ito, *Bull. Chem. Soc. Jpn.*, 1987, **60**, 2517–2522.

94 D. Cheng, F. R. Negreiros, E. Aprà and A. Fortunelli, *ChemSusChem*, 2013, **6**, 944–

965.

95 J. Rosen, G. S. Hutchings, Q. Lu, S. Rivera, Y. Zhou, D. G. Vlachos and F. Jiao, *ACS Catal.*, 2015, **5**, 4293–4299.

96 J. Shen, M. J. Kolb, A. J. Göttle and M. T. M. Koper, *J. Phys. Chem. C*, 2016, **120**, 15714–15721.

97 X. Huang, Z.-F., Wang, J., Peng, Y., Jung, C.-Y., Fisher, A., Wang, *Adv. Energy Mater.*, 2017, **7**, 1700544.

98 N. D. Schley, J. D. Blakemore, N. K. Subbaiyan, C. D. Incarvito, F. Dsouza, R. H. Crabtree and G. W. Brudvig, *J. Am. Chem. Soc.*, 2011, **133**, 10473–10481.

99 E. E. Benson, C. P. Kubiak, A. J. Sathrum and J. M. Smieja, *Chem. Soc. Rev.*, 2009, **38**, 89–99.

100 J. Y. Becker, B. Vainas, R. Eger and L. Kaufman, *J. Chem. Soc. - Ser. Chem. Commun.*, 1985, 1471–1472.

101 Y. Kushi, H. Nagao, T. Nishioka, K. Isobe and K. Tanaka, *Chem. Lett.*, 1994, 23, 2175–2178.

102 Y. Kushi, H. Nagao, T. Nishioka, K. Isobe and K. Tanaka, *Chem. Lett.*, 1994, 23, 2175–2178.

103 W. J. Evans, C. A. Seibel and J. W. Ziller, *Inorg. Chem.*, 1998, **37**, 770–776.

104 R. Senthil Kumar, S. Senthil Kumar and M. Anbu Kulandainathan, *Electrochem. commun.*, 2012, **25**, 70–73.

105 E. Schuler, M. Demetriou, N. R. Shiju and G. M. Gruter, *ChemSusChem*, 2021, **14**, 3636–3664.

106 R. P. S. Chaplin and A. A. Wragg, *J. Appl. Electrochem.*, 2003, **33**, 1107–1123.

107 O. P. Balaj, C. K. Siu, I. Balteanu, M. K. Beyer and V. E. Bondybey, *Chem. - A Eur. J.*, 2004, **10**, 4822–4830.

108 S. Kaneco, N. H. Hiei, Y. Xing, H. Katsumata, H. Ohnishi, T. Suzuki and K. Ohta, *Electrochim. Acta*, 2002, **48**, 51–55.

109 M. Azuma, *J. Electrochem. Soc.*, 1990, **137**, 1772.

110 Y. Hori, K. Kikuchi, A. Murata and S. Suzuki, *Chem. Lett.*, 1986, **15**, 897–898.

111 J. Hussain, H. Jónsson and E. Skúlason, *Faraday Discuss.*, 2016, **195**, 619–636.

112 G. Filardo, S. Gambino, G. Silvestri, A. Gennaro and E. Vianello, *J. Electroanal. Chem.*, 1984, **177**, 303–309.

113 N. Bloom and J. Van Reenen, *NBER Work. Pap.*, 2013, 89.

114 J. D. Smith, *J. Organomet. Chem.*, 1991, **414**, C33.

115 A. Gennaro, A. A. Isse, J. M. Savéant, M. G. Severin and E. Vianello, *J. Am. Chem.*

Soc., 1996, **118**, 7190–7196.

116 B. Innocent, D. Liaigre, D. Pasquier, F. Ropital, J. M. Léger and K. B. Kokoh, *J. Appl. Electrochem.*, 2009, **39**, 227–232.

117 Wöhler, *Polytech. J.*, 1824, **15**, 177–184.

118 C. L. Beadle and S. P. Long, *Biomass*, 1985, **8**, 119–168.

119 Gallently, *Polytech. J*, 1882, 244.

120 F. D. Meylan, V. Moreau and S. Erkman, *J. CO_2 Util.*, 2015, **12**, 101–108.

121 A. Kätelhön, R. Meys, S. Deutz, S. Suh and A. Bardow, *Proc. Natl. Acad. Sci. U. S. A.*, 2019, **166**, 11187–11194.

122 M. E. Royer, *Compt. read.*, 1869, 1374.

123 J. and F. G. Tafel, *Ber.,* 1904, 3187.

124 E. Baur, *Z. Elecktrochem.,* 1919, 102.

125 W. Mohschulz, *Z. Elecktrochem.,* 1926, 434.

126 H. Nakata, *Anniv. Vol. Dedic. to M. Chikashige, Kyoto Imp. Univ.*, 1930, 49.

127 L. I. Listopadov, V. V., and Antrpov, *Nauch. Tr. Navocherkassk Politekh Inst.,* 1956, 87.

128 A. N. Florianovich, G. M. and Frumkin, *Dokl. Akad. Nauk S.S.S.R.,* 1951, 997.

129 J. Smialowski, M, and Jarmolowicz, *Bull.acad.polon.sci.classe III,* 1955, 107.

130 D. J. Pickett and K. S. Yap, *J. Appl. Electrochem.*, 1974, **4**, 17–23.

131 F. P. Abramo, F. De Luca, R. Passalacqua, G. Centi, G. Giorgianni, S. Perathoner and S. Abate, *J. Energy Chem.*, 2022, **68**, 669–678.

132 M. A. Farkhondehfal, U. Savino, A. Chiodoni, C. F. Pirri and A. Sacco, *Electrocatalysis*, 2023, **14**, 195–201.

133 M. Sadakiyo, S. Hata, X. Cui and M. Yamauchi, *Sci. Rep.*, 2017, **7**, 1–9.

134 R. Watanabe, M. Yamauchi, M. Sadakiyo, R. Abe and T. Takeguchi, *Energy Environ. Sci.*, 2015, **8**, 1456–1462.

135 I. Gimenez, F. Application, P. Data, O. Electrochemistry and P. E. P. Demers, 1987, 1–4.

136 W. Qin, Y. Zhang, Z. Li and Y. Dai, *J. Chem. Eng. Data*, 2003, **48**, 430–434.

137 M. A. Murcia Valderrama, R. J. Van Putten and G. J. M. Gruter, *ACS Appl. Polym. Mater.*, 2020, **2**, 2706–2718.

138 O. M. Koivistoinen, J. Kuivanen, D. Barth, H. Turkia, J. P. Pitkänen, M. Penttilä and P. Richard, *Microb. Cell Fact.*, 2013, **12**, 1–16.

139 B. Pereira, Z. J. Li, M. De Mey, C. G. Lim, H. Zhang, C. Hoeltgen and G. Stephanopoulos, *Metab. Eng.*, 2016, **34**, 80–87.

140 D. L. Goldfarb, H. R. Corti, F. Marken and R. G. Compton, *J. Phys. Chem. A*, 1998, **102**, 8888–8893.

141 L. A. Yusuf, Z. Ertekin, S. Fletcher and M. D. Symes, *Ultrason. Sonochem.*, 2024, **103**, 106792.

142 S. Merouani, O. Hamdaoui, F. Saoudi and M. Chiha, *J. Hazard. Mater.*, 2010, **178**, 1007–1014.

143 C. Kormann, D. W. Bahnemann and M. R. Hoffmann, *Environ. Sci. Technol.*, 1988, **22**, 798–806.

144 J. Fischer, T. Lehmann, E. Heitz, *J. of A. Electrochem.*, 1981, **11**, 743–750.

145 S. Ikeda, T. Takagi and K. Ito, *Bull. Chem. Soc. Jpn.*, 1987, **60**, 2517–2522.

Overview of the Experimental Techniques Used

1.1 Electrochemical Techniques

This thesis employed a range of different electrochemical and analytical techniques. Observing potential, current, charge, and resistance provides valuable insights into the target products and possible by-products in the electrochemical system. The following section will delve into the fundamentals of electrochemistry and various methods employed throughout the thesis.

2.1.1 Electrochemical Setup

In most cases, electrochemical reactions are investigated using a standard three-electrode setup comprising a working electrode, a counter electrode, and a reference electrode.[1–3] The diagram below (Figure 2.1) illustrates the configuration of a three-electrode electrochemical cell.

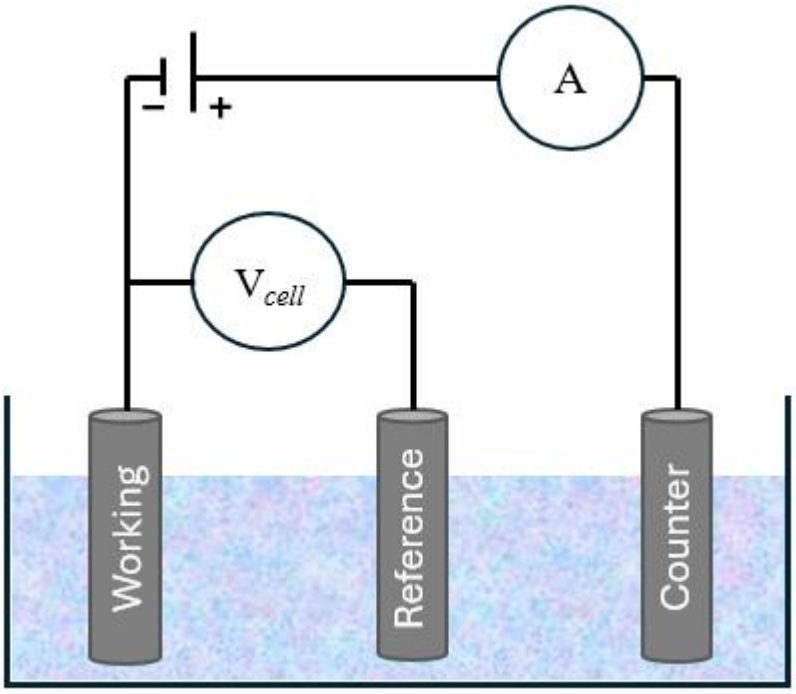

Figure 2.1: Schematic diagram of a conventional 3-electrode cell

The working electrode is usually the site of the studied electrochemical reaction, and any experiment investigating an electrode reaction must focus on monitoring changes at the working electrode surface or the working electrode side of the cell in the case of a divided electrochemical cell,[1,2] as employed in this research (Chapters 3, 4 & 5). Various materials can serve as working electrodes, chosen based on factors such as experimental requirements

and specific properties of the electrode material like cost, stability, selectivity towards the target product, etc. In this thesis, lead (Pd), titanium (Ti/Ti_xO_y), and Cu plate were used as working electrodes in chapters 3, 4 and 5, respectively.

The counter electrode, also known as the secondary electrode, plays a vital role in an electrochemical cell by supplying a current of equal magnitude but opposite sign to that of the working electrode. If the reaction at the working electrode involves reduction, the counter electrode performs oxidation, and *vice versa*. The process at the counter electrode must not interfere with the chemistry and current response at the working electrode. [1,2] An effective counter electrode facilitates a ready electron-transfer reaction, ensuring equal and opposite current to the process at the working electrode. In this thesis, electrode materials like platinum wire, platinum foil and graphite rod were employed as counter electrodes.

Reference electrodes are galvanic half-cells designed to maintain a constant potential consistently throughout an electrochemical experiment, with a predetermined and consistent value. Ideally, the half-cell reaction operates independently of the current density, and potentiostats are configured to minimise current flow through the reference electrode.[2–4] During the electrochemical reaction, minimal current passes through the reference electrode, which serves the purpose of providing a stable potential for referencing the voltage at the working electrode. Various reference electrodes are available for both aqueous (e.g., standard hydrogen electrode, reversible hydrogen electrode, Ag/AgCl) and non-aqueous (e.g., $Ag/AgNO_3$) solvents. In the context of references in non-aqueous (organic solvents), these are more accurately described as part of a broader category known as pseudo-references, where the potential varies predictably.[3] A saturated calomel electrode (SCE) was employed as a reference electrode throughout the experiments in this thesis.

2.1.2 Voltammetry Techniques

Voltammetry is a technique that examines how current varies in relation to the potential applied. It employs electrochemical cells to explore the reactions that take place at the interfaces between electrodes and electrolytes.[5] Voltammetry is the most popular electrochemical technique for rapidly generating qualitative and quantitative data. It explores the redox activity of the studied species across a range of applied potentials, measuring the current response as the working electrode's potential changes at a fixed rate, known as the scan rate. The two primary voltammetry techniques are linear sweep voltammetry (LSV) and cyclic voltammetry (CV).

2.1.2.1 Linear Sweep Voltammetry (LSV) and Cyclic Voltammetry (CV)

Linear sweep voltammetry is a technique in voltammetry where the current at a working electrode is recorded as the potential difference between the working electrode and a reference electrode is swept linearly in time. In linear sweep voltammetry, the potential is swept in one direction from a chosen starting point, E_1, to an endpoint, E_2. The voltage is scanned from a lower limit to an upper limit, as illustrated in Figure 2.2.

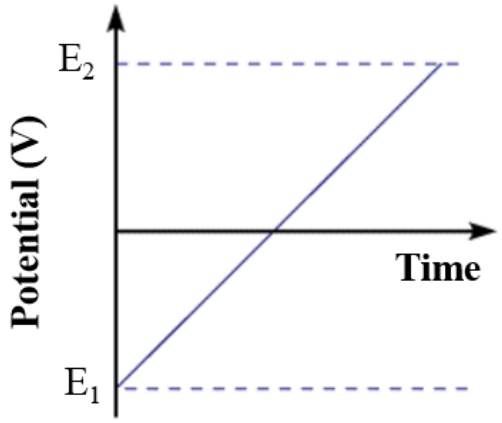

Figure 2.2: Schematic graph showing the potential-time graph for a typical linear sweep voltammetry (LSV) experiment.

Conversely, the technique slightly differs in cyclic voltammetry. In a standard cyclic voltammetry experiment, an initial potential (E_i) is selected, and then the potential is swept from E_i to E_1. The sweep direction is then reversed until E_2 is reached and again reversed to return to the initial potential E_i, completing a full cycle. In some instances, E_i may equal E_1. Figure 2.3 visually depicts a typical cyclic voltammogram, illustrating how the potential changes over time. Unlike linear sweep voltammetry (LSV), where the potential is swept in one direction, cyclic voltammetry introduces a return scan in the same experiment, allowing for an examination of the reversibility of an electrochemical reaction. In cyclic voltammetry, it is essential to maintain the electrolyte solution in a static state until the experiment concludes to restrict mass transport within the solution. This is vital to ensure that any observed changes in the current response are due to the electrochemical or chemical processes at the working electrode, not because of mass transport within the solution. For similar reasons, cyclic voltammograms are typically recorded under an inert atmosphere to

prevent atmospheric gases, primarily oxygen, from reacting with or interfering with the species under investigation. In this context, it is also important that the inert gas (argon or nitrogen) supply does not disrupt the solution through increased convection.

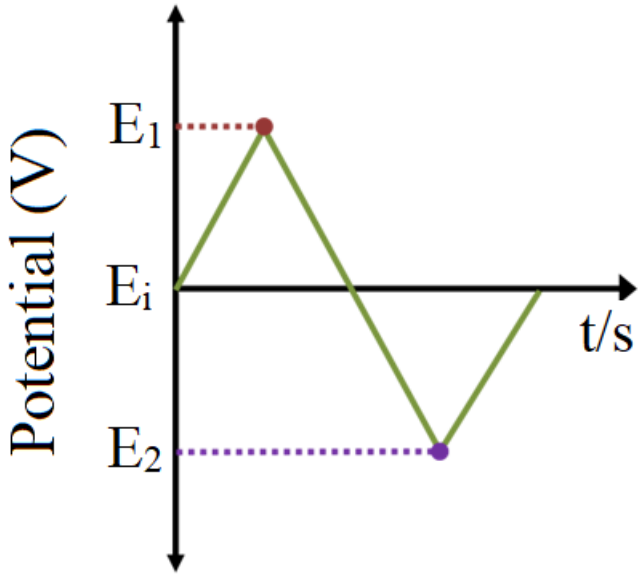

Figure 2.3: Schematic graph showing the potential-time graph for a typical cyclic voltammetry experiment.

2.1.3 Reversibility of a Redox Process

In electrochemistry, the term "reversibility" is frequently employed. However, it typically relates to the electrochemical reversibility of a system rather than chemical reversibility. To understand the distinction between chemical and electrochemical reversibility, we must examine the half-equation governing chemical reaction (equation 2.1)

$$Ox + ne^- \rightarrow Red \qquad (Equation\ 2.1)$$

In a chemically reversible reaction, the oxidised species (*Ox*) can accept 'n' electrons to be reduced to the reduced species (*Red*). Simultaneously, the *Red* species can be oxidised to the *Ox* species if they lose 'n' electrons. However, if either of these two processes is hindered (for example, if the *Red* species decomposes upon electron transfer), the process is deemed a chemically irreversible reaction. This is a crucial concept in understanding the dynamics of electrochemical reactions.[4]

In an electrochemical system, it is crucial to consider both the charge transfer from the electrode to the active species in the bulk solution and the mass transport from the bulk

solution to the electrode surface. To analyse this system, we need to break down equation 2.1 into two concerted processes, which are represented by equations 2.2 and 2.3.

$$Ox_{bulk} \rightarrow Ox_{surface} \qquad (Equation\ 2.2)$$

$$Ox_{surface} + ne^- \underset{k_{ox}}{\overset{k_{red}}{\longleftrightarrow}} Red_{surface} \qquad (Equation\ 2.3)$$

In an electrochemical system, if the rates of oxidation and reduction (represented by k_{ox} and k_{red}, in equation 2.3) are large and exceed the rate of mass transport, the redox process (as depicted in equation 2.2) remains in equilibrium. Under these circumstances, the process is termed as "electrochemically reversible". Conversely, when both k_{ox} and k_{red} are small, it implies that the electron transfer is slower than the mass transfer. This prevents the reaction from maintaining equilibrium. As a result, the equilibrium shifts towards the reaction with the higher rate. This scenario is classified as "electrochemically irreversible".[2,4,5]

In addition to the reversible and irreversible regimes, there is a third classification known as the "quasi-reversible" regime. In this scenario, the rate of mass transport is roughly equal to the rates of the reduction and oxidation reactions. However, despite these rates being of the same magnitude, the process is not truly reversible. This can occur when the system is in a state where it does not fully meet the criteria for either complete reversibility or irreversibility.

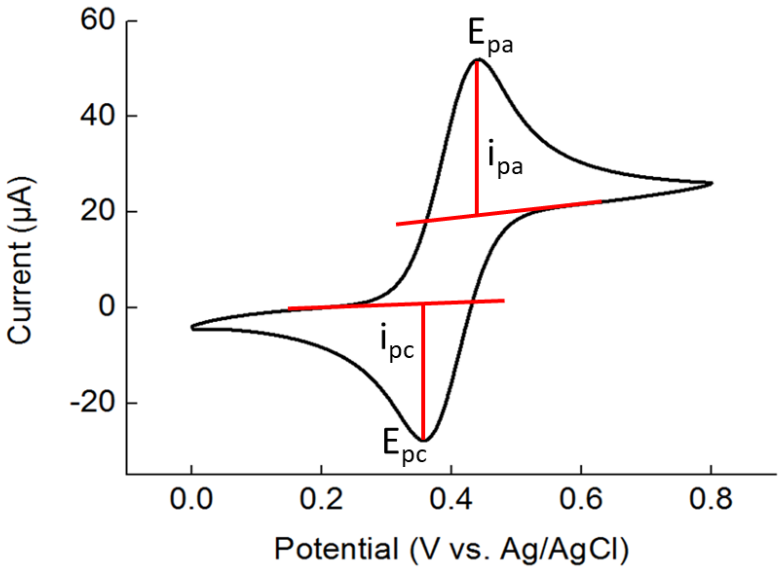

Figure 2.4: A typical cyclic voltammogram of the reversible wave of the ferrocene/ferrocenium redox couple.

Figure 2.4 displays a typical cyclic voltammogram of a reversible redox couple (ferrocene/ferricenium). Key information, such as the cathodic peak potential (E_{pc}), anodic peak potential (E_{pa}), cathodic current (i_{pc}), and anodic current (i_{pa}) is highlighted in red lines. Crucial aspects of a CV include the peak-to-peak separation and the ratio of oxidation/reduction peaks. A ratio close to 1:1 signifies reversibility, while a significant deviation indicates irreversibility or quasi-reversibility. Additionally, the current in each process (i_{pc} and i_{pa}) serves as a measure of the reaction rate, with larger currents indicating higher rate of reaction.

2.1.4 Bulk Electrolysis

Electrolysis is a method in electrochemistry that uses an external power source to trigger redox reactions that would not naturally have happened. Depending on the variables involved in the process, electrolysis reactions can be classified into two types: chronopotentiometric and chronoamperometric.[1,2]

Chronopotentiometry, also called galvanostatic electrolysis, involves imposing a fixed current demand on the system while measuring the potential required to achieve this current value over time. In a chronopotentiometry experiment, the potentiostat adjusts the applied potential to counteract a low current response, potentially altering the redox process. As a result, this technique offers less control over the reaction compared to chronoamperometry.

Chronoamperometry involves applying a set potential to the working electrode for a specific duration, during which the system's current response is observed over time. This method offers a higher degree of control in electrochemical processes, as it allows for the study of particular redox species based on their redox potential, which is typically determined in prior cyclic voltammetry experiments. Considering the advantage of chronoamperometry over chronopotentiometry for exploratory research, all bulk electrolysis experiments in this thesis were accomplished using the chronoamperometric technique.

Both methods allow for the calculation of the theoretical yield in an electrochemical reaction. Initially, the charge passed (*Q)* is determined by multiplying the current *(I)* by the reaction time (t) as shown in Equation 2.4. Subsequently, Faraday's law of electrolysis is applied using this value to ascertain the theoretical yield of the reaction product. Consequently, the Faraday efficiency of the electrochemical process can be calculated (Equation 2.5).[2] The Faraday efficiency is a measure of how effectively a system conducting an electrochemical reaction transfers charge or electrons.

$$Q = It \qquad (Equation\ 2.4)$$

$$Q = mnF \qquad (Equation\ 2.5)$$

Where *Q* represents the charge passed in Coulombs, *m* stands for the number of moles of the electroactive species being examined, *n* is the number of electrons transferred per mole of the electroactive species, and *F* is the Faraday constant, which is equivalent to 96,485 C mol^{-1}.[2,6]

2.2 Liquid Chromatography-Mass Spectrometry

Liquid chromatography-mass spectrometry (LC-MS) is a highly valuable technique for researchers studying compound mixtures. This analytical technique synergises liquid chromatography's physical separation capabilities with the analytical precision of mass spectrometry. The upcoming section will introduce the fundamentals and instrumentation of both components in this method.

2.2.1 Liquid Chromatography

Liquid chromatography is a separation technique for mixed samples, isolating individual components within a mobile phase based on their movement rate through a stationary phase.[7] The mobile phase, typically a liquid, is maintained under high pressure (up to 400 bar) to ensure a consistent flow rate. The stationary phase consists of chemically modified silica, such as silica with bonded C_{18} alkyl groups, packed into a column designed to withstand high liquid pressures during the experiment. The choice of the mobile phase is influenced by the sample's solubility, typically favouring a more polar mobile phase than the stationary phase. Successful separation with a single solvent is not always feasible, leading to the use of multiple-solvent eluent systems that can be fine-tuned to optimise component separation.[7] Successful execution results in specific compounds exhibiting characteristic retention times in certain eluent systems, allowing for theoretical identification. However, the challenge arises when many compounds share identical retention characteristics in a given medium, necessitating further analysis for definitive identification. In such instances, mass spectrometry analysis has been proven to be a complementary technique by extracting the mass to validate the presence of each compound. A schematic diagram of a liquid chromatography-mass spectrometer (LC-MS) is represented in Figure 2.5.

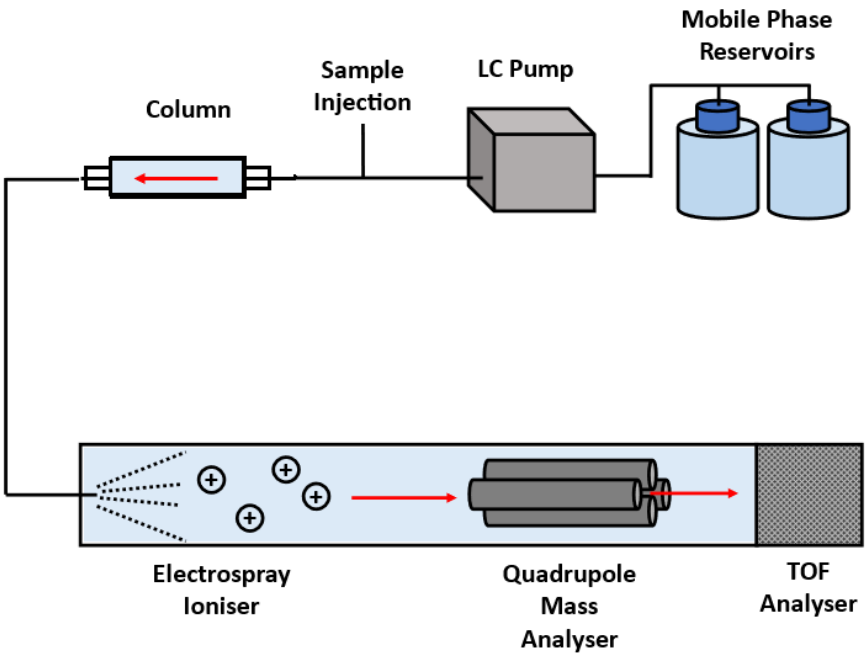

Figure 2.5: Schematic flow diagram of a liquid chromatography-mass spectrometer

2.2.2 Mass Spectrometry

Mass spectrometry provides details about the structural composition and molecular weight of an analyte. The instrument's operation involves three key stages: ionisation of the sample,

subsequent separation of the ions, and final analysis. It is crucial to state that, despite its name, this technique does not directly detect the mass of ions. Instead, it detects the ratio of their mass to charge (m/z).[8]

Various methods exist for ionising a sample, but this thesis exclusively utilizes electrospray ionization (ESI), limiting further discussion to this approach. ESI employs electrical charge to transfer ions from a solution into a gaseous phase. In simple terms, the liquid sample continuously passes through a capillary needle maintained at a significant potential difference to the surrounding chamber (2.5 – 6.0 kV).[9] As the liquid exits the capillary tip, it forms an aerosol of charged droplets. Driven by potential and pressure gradients, these droplets move toward the analyser. During this process, a drying gas removes the solvent until the droplets reach a critical electric field strength, causing ions within the droplet to eject into the gaseous phase.[9]

The separation of these generated ions leverages the fact that ions with different m/z values exhibit distinct movements in a magnetic or electrical field.[9] Various analytical instruments, including quadrupole, time-of-flight (TOF), and ion trap mass analyzers, have been developed for this stage. In this thesis, a tandem-in-space mass analysis process was employed, combining a quadrupole mass analyzer with simultaneous TOF analysis. Therefore, further discussion will be confined to this specific analytical approach.

As the name implies, a quadrupole mass analyser consists of four parallel rods. These rods supply a direct current (DC) that is superimposed with a radiofrequency alternating current (AC). The rods positioned opposite each other are electrically connected, and the AC component between the two pairs is 180 degrees out of phase. For each specific value of these voltages, only ions of a certain mass-to-charge ratio (m/z) follow a path through the rods that leads to the detector; all other ions collide with the rods. A mass spectrum can be generated by altering the AC and DC voltages.[7,9] This method has been widely accepted due to its ease of operation and its ability to detect a broad mass range 10-4000 atomic mass units (AMU) with good resolution.[10]

A Time-of-Flight (TOF) mass analyser operates on the principle that ions produced during the ionisation phase are given identical kinetic energy. Consequently, each ion's velocity is proportional to the square root of its mass, and the time it takes for the ion to reach the detector serves as an indication of its m/z.[7] This principle allows for effective ion analysis and identification based on mass-to-charge ratios.

2.3 Gas Chromatography

Gas chromatography (GC) is an analytical chemistry technique that separates and analyses compounds that can be vaporised without decomposition. It is commonly employed to assess the purity of a substance or separate components in a mixture.[11] Typical gas chromatography setups include components such as a carrier gas system, injector, gas chromatographic column, detector, and data processing unit, as depicted in Figure 2.6

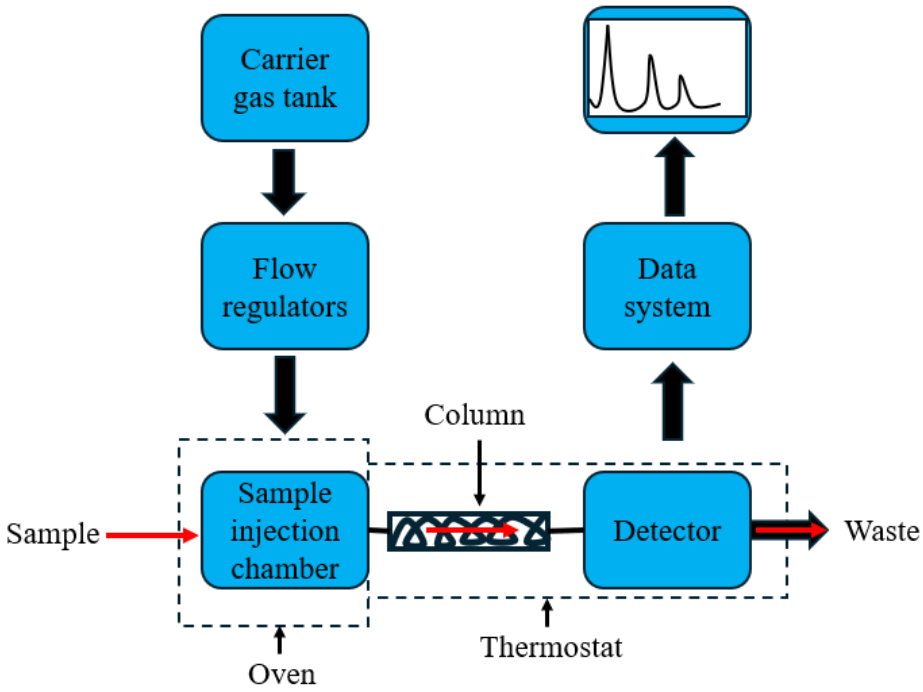

Figure 2.6: Gas chromatography analytical set-up for the separation, identification, and quantification of gases.

The process begins with the vaporisation of the sample, which is then introduced into a mobile phase. This phase usually involves a carrier gas such as helium or nitrogen that transports the vaporised sample through a stationary phase. This stationary phase could be a liquid or solid coating inside a column. The sample's components interact with the stationary phase in varying ways, leading to their separation and subsequent elution from the column at different intervals. As chemicals exit the column, they are electronically detected and identified. The detector identifies a physicochemical characteristic of the analyte and generates a response. This response is amplified and transformed into an electronic signal by a thermal conductivity detector (TCD), thereby creating a chromatogram. Owing to its high sensitivity, precision, and efficiency in dissecting complex mixtures, GC finds extensive application in diverse areas such as environmental analysis, forensics, pharmaceuticals, and food analysis.[11,12]

2.4 Ellipsometry

Ellipsometry is a highly sensitive and non-destructive optical reflectance measurement that offers unparalleled capabilities in thin film metrology.[13] It can provide valuable information on the composition, thickness, conductivity, and porosity of thin films, as these factors influence the optical properties of the films.

Ellipsometry operates on a simple principle: it measures the alteration in the polarisation of light that is reflected off the surface of a sample by determining the amplitude ratio of two beams polarised at right angles to each other. While ellipsometry measurements on their own may not provide significant insights, they can become extremely valuable when analysed using a suitable model.[14,15] This allows for a more comprehensive understanding of the data. Ultimately, the outcomes of ellipsometry are invariably reliant on the model used. Fortunately, the physics governing the reflection of light from surfaces is well understood, enabling the creation of highly precise and detailed models rooted in classical electromagnetic theory based on Maxwell's equations (Equations 2.6 and 2.7).[14] This understanding allows for a more accurate interpretation of ellipsometry results.

Figure 2.7 illustrates a diagram of light reflection from a sample surface. The light beam strikes the sample surface at an incidence angle (ϕ). The specularly reflected beam emerges from the sample surface at the same angle, ϕ. The incident and reflected beams establish a plane called the 'plane of incidence', which defines two polarisation directions:

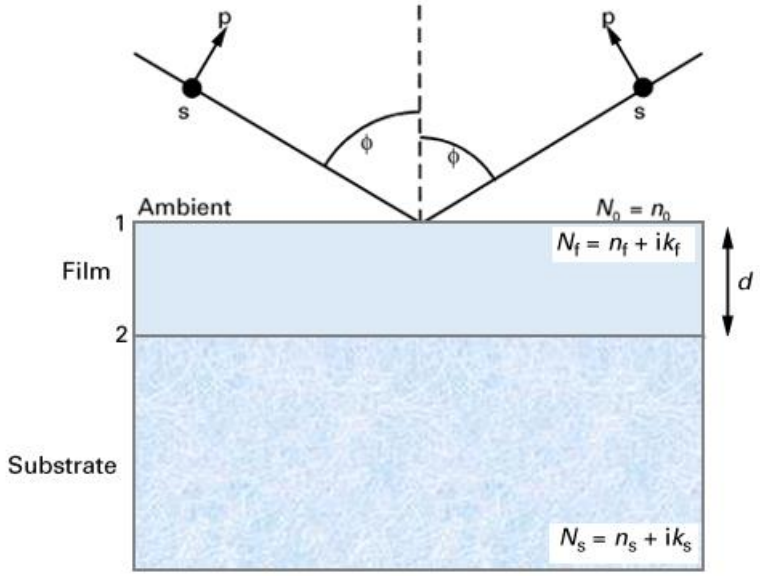

Figure 2.7: A schematic illustration depicting light reflection from a sample surface. The vectors *s* and *p* indicate the orientation of *s* and *p* polarised light, as defined by the plane of incidence. The angle of incidence is ϕ, and N_0, N_f, and N_s represent the complex refractive indices of the ambient, film, and substrate, respectively.

The term 'p' denotes light polarisation parallel to the plane of incidence, while 's' signifies light polarisation perpendicular to the plane of incidence. All azimuthal angles are determined in relation to the plane of incidence, with positive rotations being defined as clockwise rotations when viewed from the perspective of the light source towards the detector.

If the sample surface is isotropic and devoid of any film or additional overlay (d = 0 in Figure 2.7), then Maxwell equations can be employed to compute the complex reflection coefficients.

$$r_p = \frac{N_s\cos(\phi_0) - N_0\cos(\phi_s)}{N_s\cos(\phi_0) - N_0\cos(\phi_s)} \qquad (Equation\ 2.6)$$

$$r_s = \frac{N_0\cos(\phi_0) - N_s\cos(\phi_s)}{N_0\cos(\phi_0) - N_s\cos(\phi_s)} \qquad (Equation\ 2.7)$$

In Equations 2.6 and 2.7, N_0 and $N_s = n_s + ik_s$ (where n_s is the refractive index and k_s is the extinction coefficient). The quantities ϕ_0 and ϕ_s are complex angles, determined by Snell's law: $[N_0 \sin(\phi_0) = N_s \sin\phi_s]$. The reflection ratios r_p and r_s are complex, indicating that the light reflected from a surface will generally undergo a phase shift.

However, if the surface region of the substrate (sample) consists of a film, the composite reflection coefficients can be calculated from the Airy formula (Equations 2.8 and 2.9):

$$r_{s,p} = \frac{r_{1s,p} + r_{2s,p}e^{-2ib}}{1 + r_{1s,p}\, r_{2s,p}e^{-2ib}} \qquad (Equation\ 2.8)$$

$$b = \frac{2\pi d N_f \cos(\phi_f)}{\lambda} \qquad (Equation\ 2.9)$$

Here, d represents the thickness of the film, N_f is the complex refractive index of the film, and ϕ_f is the complex angle within the film as defined by Snell's law. The terms $r_{1s,p}$ and $r_{2s,p}$ are the complex reflection coefficients calculated using Equations 2.8 and 2.9 for the air–film interface and the film–substrate interface, respectively.

2.5 Atomic Force Microscopy (AFM)

Atomic Force Microscopy (AFM) represents a powerful and versatile form of scanning probe microscopy (SPM), delivering highly detailed three-dimensional images of samples with exceptional resolution.[16] It operates on the principles of force detection between a pointed tip and the surface of a sample, offering comprehensive insights into the surface structure, mechanical attributes, and interactions at the nanometer level. It can image various surfaces, encompassing metals, polymers, ceramics, composites, glass, and biological specimens.

The fundamental operational procedure of AFM entails capturing the topography of a sample surface through the scanning of a cantilever across a region of interest. This is achieved by securing one end of a cantilever, known for its high sensitivity to weak forces, and subsequently engaging with the sample surface via a nanoscale tip affixed to the opposite end of the cantilever. Weak forces between the atoms on the sample surface and the atoms on the tip induce fluctuations in the probe. This enables the measurement of the sample surface by a detector. By monitoring the cantilever oscillation and converting it into a signal, topographic images can be generated by plotting the oscillation against its position on the sample surface.[17] The experimental set-up for AFM measurement is depicted in Figure 2.8.

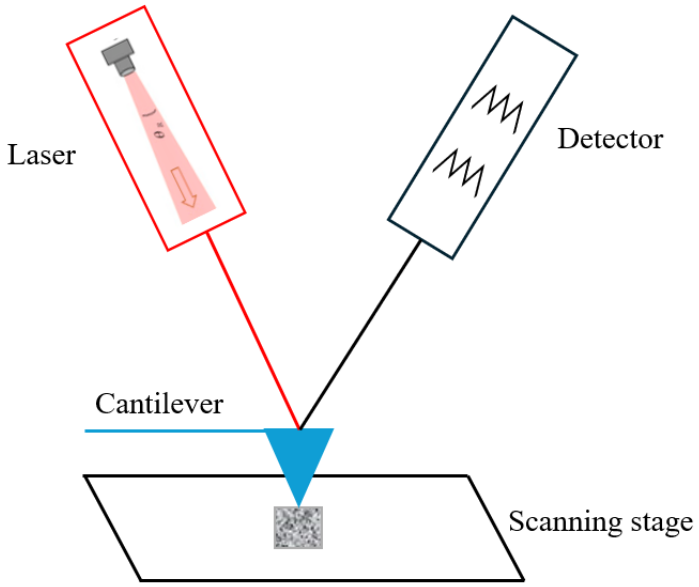

Figure 2.8: Schematic of an AFM experimental set-up that detects cantilever deflection/oscillation from a laser source to measure the surface structure of a sample.

In general, the determination of surface morphology characteristics of sample material by AFM can be quantitatively described by roughness parameters, including average roughness (R_a) and root mean square roughness (R_q), represented by Equations 2.10 to 2.12:[16,18,19]

The average roughness (R_a) represents the average distance between the detected surface and the datum (Equations 2.10 and 2.11):[18]

$$R_a = \frac{1}{N_x N_y} \sum_{i=1}^{N_x} \sum_{j=1}^{N_y} \left| Z(i,j) - Z_{mean} \right| \qquad (Equation\ 2.10)$$

Where,

$$Z_{mean} = \frac{1}{N_x N_y} \sum_{i=1}^{N_x} \sum_{j=1}^{N_y} Z(i,j) \qquad (Equation\ 2.11)$$

The root mean square roughness (R_q) is represented by the mathematical expression in Equation 2.12:[19]

$$R_q = \sqrt{\frac{1}{N_x N_y} \sum_{i=1}^{N_x} \sum_{j=1}^{N_y} (Z(i,j) - Z_{mean})^2} \qquad (Equation\ 2.12)$$

Where N_x and N_y denote the amount of data in the X and Y directions, respectively. $Z(i, j)$ represents the deviation in height, while Z_{mean} refers to the average height of the baseline.

2.6 Electrochemical Impedance Spectroscopy (EIS)

Electrochemical impedance spectroscopy (EIS) is one of the highly valuable electroanalytical techniques for investigating resistances in experiments.[20] It is widely recognised that all conductors exhibit some resistance to electrical current, and this value is typically quantified using Ohm's law for resistance (Equation 2.13):

$$R = \frac{E}{I} \qquad (Equation\ 2.13)$$

Where R represents resistance, E is the applied voltage, and I is the current. However, this law applies only to an ideal resistor, which assumes, among other things, that alternating potentials and their resulting currents are in phase when passing through a resistor. In practical scenarios, a phase shift exists between the applied AC potential and the current response (Figure 2.9). In EIS, a small sinusoidal excitation signal (~5-15 mV) is applied,[21,22] while this phase shift is recorded at different frequencies to provide a more accurate understanding of the resistances or impedances within an electrochemical system.[20,23]

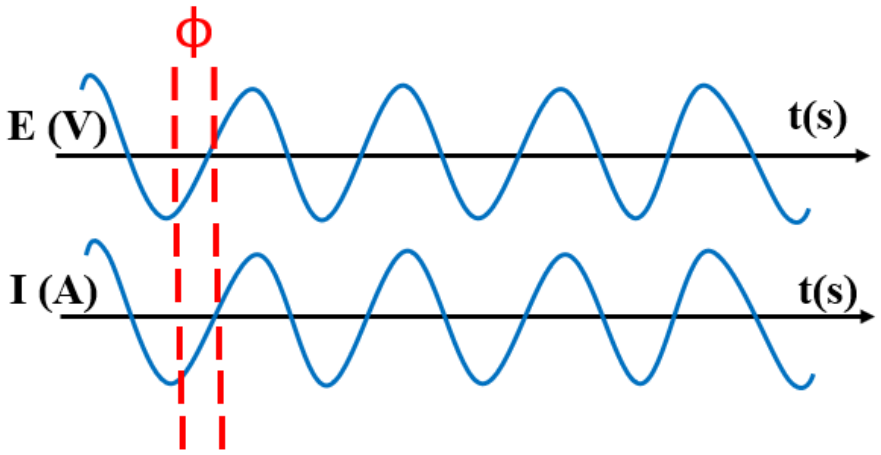

Figure 2.9: Illustration depicting the AC excitation signal (top) and current response (bottom) passing through a resistor. The two signals are characterized by a phase shift, denoted as ϕ.

Given the sinusoidal characteristic of the excitation signal, we can represent its potential as a function of both time (t) and radial frequency (ω), as shown in Equation 2.14. Similarly, the current response can be formulated using these same variables, while also accounting for the phase shift (ϕ), as depicted in Equation 2.15.

$$E_t = E_0 \sin(\omega t) \qquad (Equation\ 2.14)$$

$$I_t = I_0 \sin(\omega t + \phi) \qquad (Equation\ 2.15)$$

Where E_t and I_t represent the potential and current at a given time t, respectively. Similarly, E_0 and I_0 denote the amplitudes of these signals. The radial frequency is represented by ω and the phase shift between the two signals is given by ϕ. By applying a relationship like Ohm's law, we can derive an expression for the impedance, denoted as Z (Equation 2.16).

$$Z_t = \frac{E_t}{I_t} = \frac{E_0 \sin(\omega t)}{I_0 \sin(\omega t + \phi)} = Z_0 \frac{\sin(\omega t)}{\sin(\omega t + \phi)} \qquad (Equation\ 2.16)$$

Equation 2.16 provides a definition for the impedance at a specific time, t (Z_t), which is expressed in terms of a magnitude, Z_0, and the phase shift, ϕ. In the past, EIS measurements were analysed by constructing a "Lissajous plot" where the E_t signal is represented on the x-axis and I_t signal on the y-axis (Figure 2.10a).[24]

The evolution of modern EIS instrumentation has led to the emergence of alternative methods for presenting EIS data, such as Nyquist or Bode plots. In this thesis, the interpretation of EIS data is exclusively carried out using Nyquist plots, necessitating further manipulation of Equation 2.16. The first step involves considering Euler's formula, which outlines the relationship between trigonometric and complex exponential functions (as shown in Equation 2.17).[25] This relationship can be applied to modify our expressions for E_t and I_t (as per Equations 2.18 & 2.19), enabling the representation of impedance at any given frequency as a complex number (as illustrated in Equation 2.20).

$$\exp(i\phi) = cos\phi + isin\phi \qquad (Equation\ 2.17)$$

$$E_t = E_0 \exp(i\omega t) \qquad (Equation\ 2.18)$$

$$I_t = I_0 \sin(i\omega t - \phi) \quad (Equation\ 2.19)$$

$$Z_\omega = \frac{E_t}{I_t} = Z_0 \exp(i\phi) = Z_0(cos\phi + isin\phi) \quad (Equation\ 2.20)$$

As evident from the above expression (Equation 2.20), the impedance at a specific frequency comprises both a real and an imaginary component. In a Nyquist plot, these components are represented on the x- and y-axes, respectively (Figure 2.10b). The EIS data displayed on a Nyquist plot typically forms a semi-circle from which various values can be inferred. The high-frequency intercept on the x-axis (the left side of the semi-circle) corresponds to the experiment's solution resistance (R_s). The impedance can be depicted as a vector extending from this intercept to the "peak" of the semi-circle, with a length of |Z|, and the angle of this vector represents the phase angle (ϕ). The charge transfer resistance (R_{ct}) is determined by the difference between the high-frequency and low-frequency intercepts. It represents the total resistance encountered when polarising the cell, which includes factors like energy barriers related to the electrochemical reaction being studied, as well as kinetic and mass transfer effects.[20,24]

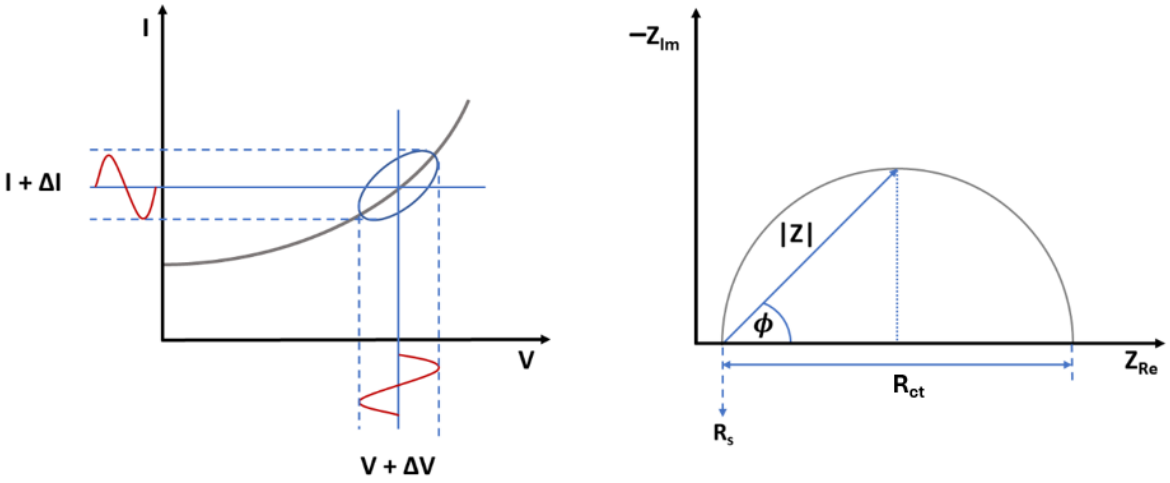

Figure 2.10: Depiction of EIS data (a) in the form of a Lissajous plot, and (b) a Nyquist plot as described by Magar et al. [20]

Electrochemical Impedance Spectroscopy (EIS) can be applied to investigate the inherent properties of materials or specific processes that could affect the conductance, resistance, or capacitance within an electrochemical system.[20] Electrochemical impedance spectroscopy data acquired from experiments is frequently subjected to fitting with an equivalent circuit to facilitate the determination of electrochemical parameters associated with various processes in the system, as illustrated in Figure 2.11. In the equivalent circuit model, Rs

refers to the solution resistance, while R_1 and R_2 represent charge transfer resistance. CPE1 and CPE2, representing the constant phase elements, are commonly used to describe nonhomogeneous surfaces.[26] A constant phase element is an equivalent electrical circuit component that models the behaviour of a double layer or non-homogeneous surface, acting as an imperfect capacitor. Electrochemical Impedance Spectroscopy was employed as one of the characterisation techniques to analyse the titanium electrode used in Chapter 4 of this thesis.

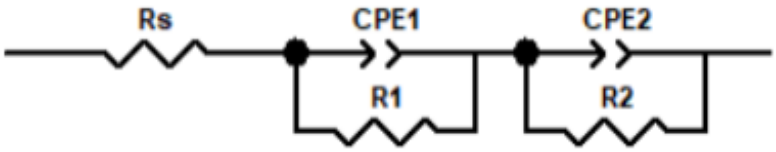

Figure 2.11: Illustration of the equivalent circuit model employed to analyse the electrochemical impedance spectroscopy (EIS) data acquired for the titanium electrode in Chapter 4.

2.7 UV-visible Spectroscopy

UV-visible spectroscopy is a potent analytical technique extensively used in chemistry. It measures the absorption of ultraviolet (UV) and visible light by molecules, delivering valuable insights into their electronic structure and bonding. While the UV wavelength spans from 100 to 380 nm, and the visible component extends up to 800 nm,[27] the working wavelength range of most spectrophotometers typically falls between 200 and 1100 nm. The practical range for UV-Vis spectroscopy varies from 200 to 800 nm; wavelengths beyond 800 nm fall into the infrared range, while those below 200 nm are referred to as vacuum UV. The colour of a substance, defined by its ability to absorb and emit light, is perceptible to the human eye, which can distinguish up to 10 million unique colours.[28]

UV-visible spectroscopy measures the absorbance or transmittance of light. The signal response is a function of the sample's composition (properties) and concentration. When a particular wavelength of light interacts with a molecule, the molecule becomes excited. As a result of this excitation, an electron transitions from its ground (lower) energy state to a higher energy state. When the electron subsequently moves away from the molecule, it absorbs light energy. This absorption occurs because electrons in the orbital at a lower energy state utilise energy to transition to a higher energy level.[29] Consequently, the spectra obtained

following the interaction with electromagnetic radiation are termed absorption spectra, leading to the classification as electron spectroscopy. Likewise, when electrons in the orbital at a higher energy level shift to the ground energy level, the resulting spectra are referred to as emission spectra. Figure 2.12 illustrates the experimental setup for UV-visible spectroscopy.

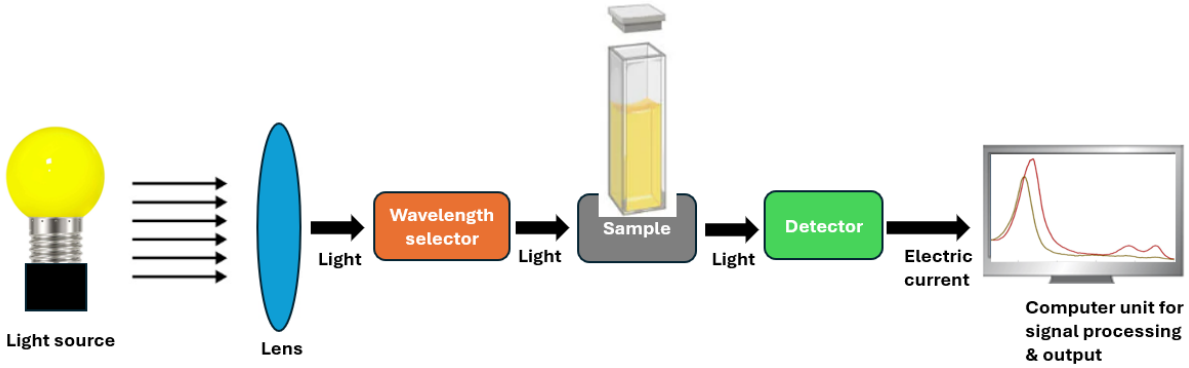

Figure 2.12: Schematic diagram of UV-visible spectroscopy.

The Beer-Lambert's law equation is the fundamental principle behind absorbance spectroscopy. By analysing the absorption spectra produced by samples at specific wavelengths, we can directly determine the sample's concentration using the law. The law states that when a beam of light passes through a transparent medium, the rate at which its intensity decreases with the thickness of the medium is directly proportional to the initial intensity of the light beam. In accordance with the law, absorbance is directly proportional to the concentration of the substance in the solution. Hence, the concentration of a sample can be determined using UV-visible spectroscopy.[28]

The Beer-Lambert equation can be formulated with the following equations:

$$A = -\log T = -\log (I/I_0) = \log (I/I_0) = \varepsilon cl \qquad (Equation\ 2.21)$$

Where, A = absorbance, T = transmittance (I/I_0), I = intensity of transmitted light, I_0 = intensity of incident light, ε = molar absorptivity ($L \cdot mol^{-1} \cdot cm^{-1}$), c = concentration of the absorbing species in the sample (mol/L), and l = the distance that light travels through the sample.

According to the Beer-Lambert law, if we measure the absorbance of a series of sample solutions with known concentrations and plot it against equivalent concentrations, the resulting graph should exhibit a linear relationship. This graph is commonly referred to as a calibration graph.

2.8 Nuclear Magnetic Resonance (NMR) Spectroscopy

NMR spectroscopy involves examining molecular behaviour by observing various isotopes of atomic nuclei when subjected to a magnetic field and radio frequency radiation. Given the high natural abundance of the ^{1}H isotope (99.9%) in organic species, hydrogen nuclei are predominantly used in NMR-based molecular studies. Other nuclei frequently observed include the ^{13}C isotope of the carbon atom, which has a natural abundance of approximately 1.1%, and ^{15}N, with a natural abundance of 0.4%.

2.8.1 Fundamentals of NMR

Nuclear Magnetic Resonance (NMR) spectroscopy is a method of analysis that enables the examination of a material's molecular structure by gauging the interaction of nuclear spins when subjected to a magnetic field.[30]

NMR is only relevant for nuclei that have a property called a magnetic moment. The magnetic moment (μ) is determined by Equation 2.22.

$$\mu = I\gamma\frac{h}{2\pi} \qquad (Equation\ 2.22)$$

Where *I* represents the quantum number for the nuclear spin, determined by the number of protons and neutrons in the nucleus, γ denotes the gyromagnetic ratio, which is the ratio of its magnetic moment to its angular momentum, and *h* represents Planck's constant.

Basically, three scenarios explain the interaction between protons and neutrons in a nucleus, all of which are related to the value of *I.* Nucleons with opposite spins can pair up (like electrons), but only with nucleons of the same type. Therefore, in atoms where the numbers of neutrons and protons are odd, *I* result in half-integral numbers (like 1/2, 3/2, etc.), making these atoms easily analysable using NMR spectroscopy. Conversely, in atoms where the numbers of neutrons and protons are even, all spins are paired, and $I = 0$. In this case (for instance, the ^{12}C isotope), the atoms are magnetically inactive and do not interact with the spectrometer. Lastly, when both neutrons and protons are present in odd numbers, *I* is an

integer number (I > 1/2), and the nucleus also has an electric quadrupole moment, Q. In this situation, the charge distribution is not spherical, which can affect the NMR spectra. However, the study of such molecules remains technically feasible.[31]

Magnetic moments within atoms can be likened to the needle of a compass aligning with the Earth's magnetic field. These moments are oriented along specific directions but can be reoriented in the presence of an external magnetic field. When a nucleus is subjected to an external magnetic field (B_0), the nuclear spin of the atom aligns itself with the external field. The potential orientations are determined by the quantum number *m*, which can assume 2*I* + 1 values. This magnetic moment does not stay fixed but undergoes precession around the direction of B_0. For instance, in the ^{1}H isotope (where $I = 1/2$), two orientations are possible: one for nuclei with $m = +1/2$ (also known as the α spin state), which aligns parallel to the external field and has lower energy, and another for nuclei with $m = -1/2$ (also known as the β spin state), which aligns against the magnetic field. Consequently, the energy of the interaction is dependent on the angle between the magnetic moment and the applied field.[31] These distinct energy states provide the essential conditions for spectroscopy. Given the minimal energy difference between these two states (on the order of $10^{-5}/10^{-6}$), a radio-wave frequency of electromagnetic radiation is sufficient to induce transitions between them. The frequency is derived from the Bohr relation (Equation 2.23) and can alternatively be expressed in terms of the gyromagnetic ratio for NMR (Equation 2.24).[30,31]

$$h\nu = \Delta E \qquad (Equation\ 2.23)$$

$$\nu = B_0 \frac{\gamma}{2\pi} \qquad (Equation\ 2.24)$$

This frequency, often referred to as the Larmor frequency in scientific literature, is directly proportional to the strength of the magnetic field (B_0). As a result, ΔE increases with higher frequencies, which explains why NMR instruments with higher frequencies are more sensitive. Figure 2.13 illustrates this.

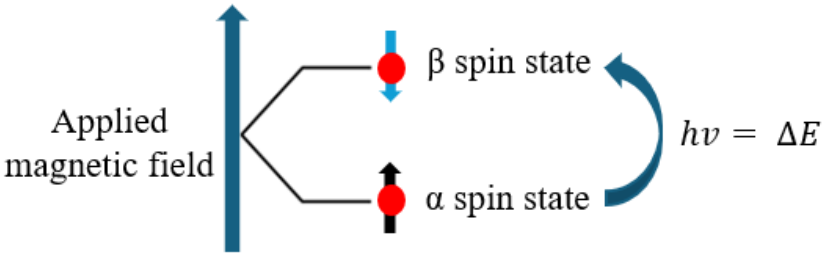

Figure 2.13: Visual representation depicting the spin states and the energy required to transition from the α spin-state to the β spin-state.

When a sample is exposed to the appropriate frequency, it absorbs energy equivalent to ΔE, allowing a lower state nucleus (α proton) to 'spin-flip' to a higher energy state (β proton). This is when the nuclei resonate with the applied radiation, giving rise to the term 'nuclear magnetic resonance'. Following excitation, the nucleus reverts to its original lower state, discharging the absorbed energy in a process known as relaxation. At this point, a minute pulse of radiofrequency electromagnetic radiation is emitted, and the corresponding signal for this energy transfer is captured and analysed to produce an NMR spectrum specific to the nucleus in question, as illustrated in Figure 2.14.[30]

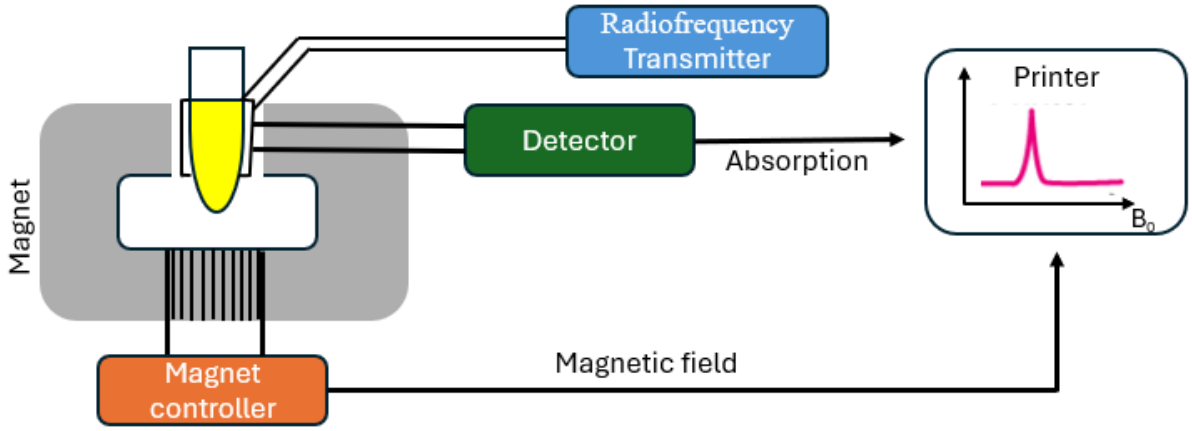

Figure 2.14: Analytical set-up depicting a nuclear magnetic resonance (MNR)

2.8.2 The Chemical Shift

When examining NMR, the chemical environment of the atom influences the frequency of the resonating nuclei. In a chemical structure, nuclei are connected to other atoms and enveloped by electrons. Since electrons are charged particles, they move in a manner that creates a local magnetic field (B_i) in response to an external field, counteracting B_0. Although

this local magnetic field is significantly smaller than the external field, it reduces the nucleus's effective magnetic field ($B_{effective} = B_0 - B_i$). When B_i is generated, the nucleus is considered to be shielded by the electron cloud. When a nucleus is associated with an electronegative atom, such as oxygen, it encounters a reduction in electron density, leading to a smaller B_i (increased $B_{effective}$) and, consequently, a rise in resonance frequency. These nuclei, referred to as de-shielded, typically appear on the left side of the spectrum, commonly known as downfield. Conversely, the opposite effect is observed when nuclei are bound to less electronegative atoms, like carbon, causing a shift of the absorption peak upfield. The alteration in absorption frequency is termed the 'chemical shift'.[30]

To facilitate the interpretation of acquired signals, the NMR absorption frequencies of a compound are juxtaposed with those of the internal standard $Si(CH_3)_4$, commonly known as tetramethyl silane or TMS. The signals emanating from TMS in both ^1H and ^{13}C NMR exhibit a slightly greater degree of shielding compared to most organic molecules, owing to the lower electronegativity of silicon relative to carbon. As the carbons and protons in TMS share the same environment, a single high-intensity signal is generated, conveniently excluded from the spectrum. An example ^1H NMR spectrum illustrating liquid-phase CO_2 reduction product is depicted in Figure 2.15.

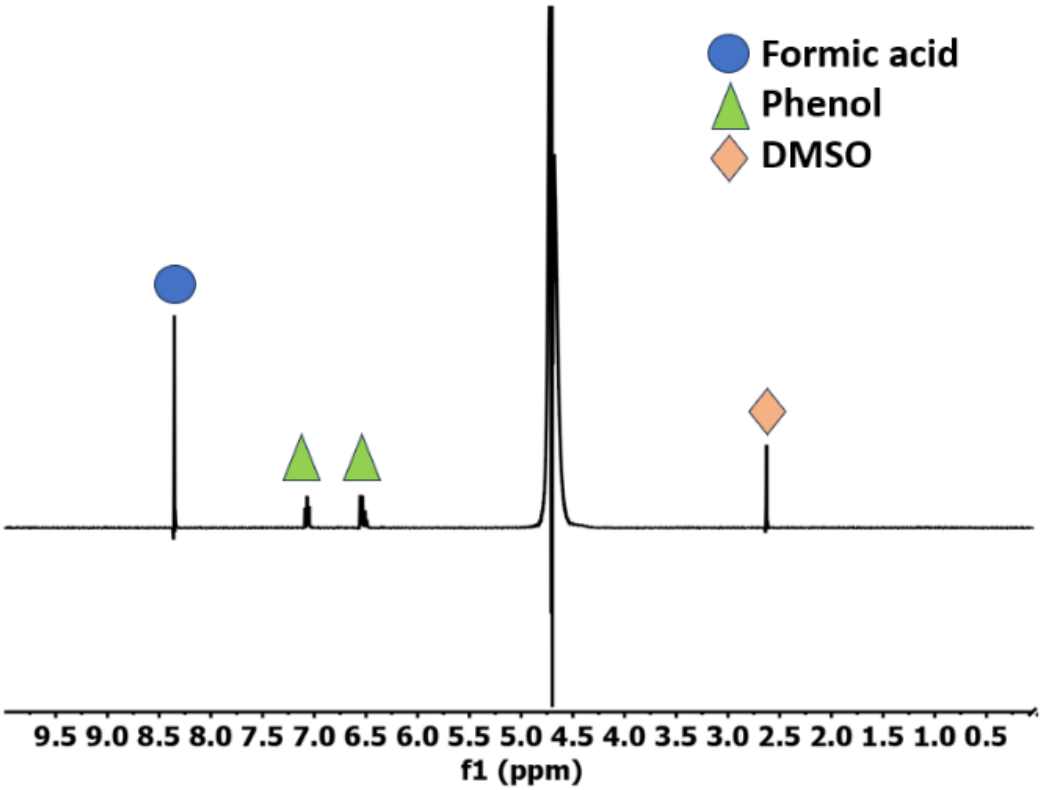

Figure 2.15: An example ^{1}HNMR spectrum illustrating liquid-phase CO_2 reduction product: formic acid with internal standard dimethyl sulfoxide-D6 (DMSO) and phenol. This NMR spectrum has been extracted from Chapter 5.

Furthermore, the resonance frequencies are directly proportional to the strength of the applied magnetic field (B_0), making them non-comparable across machines with different frequencies. To address this challenge, the concept of relative chemical shift (δ) is introduced (see Equation 2.25).

$$\delta = \frac{v_H - v_{reference}\ (Hz)}{frequency\ of\ the\ spectrometer\ (MHz)} \qquad (Equation\ 2.25)$$

The chemical shift value, which is independent of the field, is denoted in parts per million (ppm). It facilitates the comparison of chemical signals derived from various NMR machines.[30]

The typical scale for the chemical shift of ^{1}H NMR ranges from 0 to 12 ppm, and for ^{13}C NMR, it ranges from 0 to 220 ppm. In contemporary systems, the need to add TMS as an internal standard has been eliminated, as the residual signals of deuterated solvents have a standard chemical shift relative to TMS and can thus serve as a reference ($\nu_{reference}$).

2.9 References

1 J. Bard Allen and R. Faulkner, *Electrochemical Methods: Fundamentals and Applications*, John Wiley & Sons, New York., 2nd edn., 2001.

2 D. Pletcher, *A First Course in Electrode Processes,* RSC Publishing, Cambridge, 2nd edn., 2009.

3 A. L. and F. S. G. Inzelt, *Handbook of Reference Electrodes, Springer Berlin, Heidelberg*, 2013.

4 P. Zanello, *Inorganic Electrochemistry: Theory, Practice and Application*, The Royal Society of Chemistry, Cambridge, 2003.

5 N. Elgrishi, K. J. Rountree, B. D. McCarthy, E. S. Rountree, T. T. Eisenhart and J. L. Dempsey, *J. Chem. Educ.*, 2018, **95**, 197–206.

6 M. Faraday, *R. Soc.*, 1834, 77–122.

7 R. E. Ardrey, *Liquid Chromatography-Mass Spectrometry: an Introduction,* Wiley & Sons, Chichester, 2003.

8 G. L. Glish and R. W. Vachet, *Nat. Rev. Drug Discov.*, 2003, **2**, 140–150.

9 M. W. M. S. and H. L. T. C. S. Ho, C. W. K. Lam, M. H. M. Chan, R. C. K. Cheung, L. K. Law, L. C. W. Lit, K. F. Ng, *Clin. Biochem. Rev.,* 2003, **24**, 3.

10 K. J. K. and V. V. S. Parasuraman, A. Rao, S. Balamurugan, S. Muralidharan, *Pharm. Methods*, 2014, **5**, 47–55.

11 E. Forgács and T. Cserháti, *Food Authent. Traceability*, 2013, 197–217.

12 Z. Wang and J. R. Jocelyn Paré, *Tech. Instrum. Anal. Chem.*, 1997, **18**, 61–91.

13 A. Einstein, *Ann. Phys.*, 1905, **17**, 132.

14 A. Absorption and A. Emis, *Lit. Compass*, 2020, 402–411

15 V. M. Airaksinen, *Handb. Silicon Based MEMS Mater. Technol. Second Ed.*, 2015, 381–390.

16 K. Wang, K. G. Taylor and L. Ma, *Int. J. Coal Geol.*, 2021, **247**, 103852.

17 A. N. Patel and C. Kranz, *Annu. Rev. Anal. Chem.*, 2018, **11**, 329–350.

18 O. B. Abouelatta and J. Mádl, *J. Mater. Process. Technol.*, 2001, **118**, 269–277.

19 R. L. Jackson, *Handb. Lubr. Tribol. Vol. II Theory Des. Second Ed.*, 2012, **123**, 14-1-14–14.

20 H. S. Magar, R. Y. A. Hassan and A. Mulchandani, *Sensors*, 2021, **21**, 19.

21 T. Romero-Castañón, L. G. Arriaga and U. Cano-Castillo, *J. Power Sources*, 2003, **118**, 179–182.

22 R. F. Silva, M. De Francesco and A. Pozio, *J. Power Sources*, 2004, **134**, 18–26.

23 X. Yuan, H. Wang, J. Colin Sun and J. Zhang, *Int. J. Hydrogen Energy*, 2007, **32**, 4365–4380.

24 D. Qu, G. Wang, J. Kafle, J. Harris, L. Crain, Z. Jin and D. Zheng, *Small Methods*, 2018, **2**, 1–27.

25 M. A. Moskowitz, *World Scientific,* 2002.

26 A. C. Alves, F. Wenger, P. Ponthiaux, J. P. Celis, A. M. Pinto, L. A. Rocha and J. C. S. Fernandes, *Electrochim. Acta*, 2017, **234**, 16–27.

27 R. Asahi, T. Morikawa, T. Ohwaki, K. Aoki and Y. Taga, *Science (80-.).*, 2001, **293**, 269–271.

28 T. Owen, *Fundamentals of UV-visible Spectroscopy: A Workbook*, Hewlett Packard Company, Berlin, 1st edition, 1998.

29 F. S. Rocha, A. J. Gomes, C N. Lunardi, S. Kaliaguine, and G. S. Patience, *Canadian Society for Chemical Engineering,* 2008, 1-6.

30 J. Keeler, *Understanding NMR Spectroscopy*, John Wiley & Sons, Ltd, 2005.

31 J. W. A. and B. E. Mann, *NMR and Chemistry: An introduction to modern NMR spectroscopy,* Cheltenham : Stanley Thornes, c2000, 4th edn., 2000.

Optimising the Electrochemical Reduction of CO_2 to Oxalic Acid in Propylene Carbonate

Published as "Optimising the Electrochemical Reduction of CO_2 to Oxalic Acid in Propylene Carbonate" H. Sale, G. R. Ubbara and M. D. Symes, Sustain. Energy Fuels, 2023, **7**, 5093–5100.

Acknowledgements and Declaration

Halilu Sale performed the experimental work and data analysis and co-wrote the paper. Gangi R. Ubbara conducted settings and optimisation of liquid chromatography-mass spectrometry methods, and HS analysed the experimental samples. Mark Symes conceived the idea, assisted with data analysis, and co-wrote the paper.

3.1 Introduction

The rising cost of energy from fossil fuels and concern about a steady increase in the atmospheric concentration of carbon dioxide (CO_2) which is one of the major greenhouse gases have prompted a lot of attention and research towards renewable energy.[1] It has been reported that the rise in atmospheric CO_2 concentration is up by over 40% since the preindustrial era, from 280 ppm to 417.39 ppm (as of August 14, 2022).[2] The overdependence and utilisation of fossil fuels to meet energy requirements in transportation and industrial sectors is the major factor responsible for this gradual but significant increase in global CO_2 concentration, which in turn is considered to be the primary cause of climate change.[3] CO_2 as a greenhouse gas absorbs infrared heat which is reflected off the earth's surface from the sun. To mitigate the potential effects of climate change, the European Union (EU) is set to achieve a target of 80-95% greenhouse gas reduction by 2050. This noble objective is needed to keep the global temperature increase well below 2 °C, as agreed to in the 2015 Paris Climate Change Convention.[4]

In an attempt to sanitise the atmosphere and provide a sustainable source of energy, CO_2 is identified as one of the cheapest and most naturally abundant carbon sources for the production of fuels and varieties of useful intermediate chemicals for chemical industries.[5,6] The utilisation of CO_2 as a feedstock for the production of industrially relevant precursors or directly usable organic resources represents a potentially sustainable way of addressing the ever-increasing challenges posed by CO_2 in the atmosphere.[7] So many approaches, such as chemical, photochemical, thermochemical, biochemical, and electrochemical reduction methods have been deployed to achieve CO_2 conversion into useful forms[8–10]. However, from all the various methods available, previous researchers reveal that electrochemical reduction of CO_2 is found to be more attractive due to its obvious advantages of forming various industrially relevant products, higher conversion efficiency, product selectivity, ease of industrial scale-up and potential to store electrical energy obtainable from renewable sources like the sun.[5,7,11]

Various electrochemical systems have been developed for CO_2 reduction, operating with both aqueous and non-aqueous electrolytes.[12,13] Depending on the reaction conditions, particularly the nature of the cathode material (electrode) and the electrolyte, typical reaction products include CO and formic acid/formate,[14–16] with more reduced and longer-chain carbon products less frequently reported.[17] In such scenarios, multi-carbon products are frequently generated as mixtures. The components of these mixtures often present challenges during separation for product analysis.[18] Furthermore, the competing hydrogen evolution

reaction through the electroreduction of protons or water frequently serves as a significant side reaction that diminishes the efficiency of CO_2 reduction, particularly in aqueous solvents.[19,20] Therefore, achieving high selectivity for individual products from CO_2 electroreduction reactions is a critical goal for any potentially scalable electrochemical carbon dioxide reduction process.[21–23] The electroreduction of CO_2 in liquid electrolytes has resulted in a diverse array of potential products. Among these, it is interesting to state that oxalic acid ($C_2H_2O_4$) stands out due to its extensive applications in various fields such as metallurgy, pharmaceuticals, photography, metalwork cleaning, food industry, bleaching agents, and as a laboratory analytical reagent.[15,16,24–27]

The choice of media (aqueous or non-aqueous) is one of the integral factors influencing the selectivity in CO_2 reduction. Hence, utilizing non-aqueous solvents is one strategy to reduce the evolution of hydrogen during the electrochemical reduction of CO_2. Although various researchers have suggested different reaction mechanisms, there is a consensus that the initial electroreduction of carbon dioxide in non-aqueous solvents typically involves a single-electron reduction, as indicated in section 1.3.6 Description of Reaction Mechanism of CO2 Reduction on Pb Electrodein Chapter 1.

Despite the significant strides made in transforming CO_2 into various products, the electrochemical approach to CO_2 reduction also presents certain challenges. CO_2 is kinetically inert and thermodynamically stable, necessitating a substantial amount of energy to activate CO_2 and form an anion radical ($CO_2^{-\bullet}$), which acts as the starting point of the reaction. To improve the process for sustainability and economic viability, there is a need to reduce the high potential requirement of the process. In this regard, it is imperative to search for an efficient catalyst that may improve the current density at a lower applied potential

Table 3.1 This provides a summary of earlier research on the electroreduction of carbon dioxide to oxalate and oxalic acid. Many of these prior studies usually exhibit relatively low current densities (< 10 mA cm^{-2}) and oxalic acid formation rates that are less than 0.2 mM cm^{-2} h^{-1}. Both measurements could present obstacles to the potential economic feasibility of large-scale production of oxalate through electrochemical CO_2 reduction. Moreover, there are conflicting reports on the extent of side reactions: Garcia *et al.* propose that glyoxylic acid can be directly produced by the electrochemical reduction of CO_2 on glassy carbon and mercury electrodes. However, when using a lead cathode, glycolic acid is the primary side product,[28] whereas Boor *et al.*[29] discovered that both glyoxylic acid and glycolic acid can be directly obtained through the electrochemical reduction of CO_2 on a lead

electrode. Recently, Marx *et al*.[30] conducted a re-evaluation of the electrochemical reduction of CO_2 to oxalate and oxalic acid using first-row transition metal complexes. They concluded that a significant number of earlier published studies are not replicable, primarily due to the lack of sufficient experimental and analytical details.

Furthermore, the application of various benzonitriles and alkyl/phenyl benzoates have been previously reported as homogeneous catalysts for the electrochemical reduction of CO_2 in non-aqueous aprotic solvents (e.g. dimethylformamide), generating oxalate as the overwhelmingly dominant product (see Table 3.1, Entries 7 and 8).[31,32] The proposed mechanism of this catalytic reaction involves the initial formation of the relatively stable $C_7H_5N^{-\bullet}$ anion radical through a one-electron reduction process. This radical then reacts with CO_2 in solution to form $CO_2^{-\bullet}$, which in turn undergoes dimerisation to form oxalates, as summarised in Equations 1.9 – 1.12 of section 1.3.5 Benzonitrile in Chapter 1:[31]

The reaction was conducted in dimethylformamide, serving as a non-aqueous medium. However, due to its toxic nature, the utilisation of dimethylformamide is anticipated to face stringent restrictions in numerous countries soon,[33] Therefore, propylene carbonate has been suggested as a potential replacement with lower toxicity.[34] The use of non-toxic catalysts in electrochemical reactions is essential for protecting the environment, ensuring human health and safety, promoting sustainability, complying with regulations, and maintaining product purity. It is a fundamental component of responsible and sustainable chemical practices.

In a comprehensive evaluation of CO_2 electroreduction to date, it is noteworthy that Boor *et al*.[29] reported the highest current densities and rates of oxalic acid formation through CO_2 electroreduction. (Table 3.1, Entry 13) in a $(CH_3)_4NCl$/propylene carbonate solvent system using lead as a working electrode. Consequently, we formed a hypothesis that the application of soluble electrocatalysts such as benzonitrile at a lead cathode might result in even greater current densities and accelerated rates of oxalate production in a tetramethylammonium chloride $(CH_3)_4NCl$/propylene carbonate solvent system. The optimal findings from our research are displayed in Table 3.1, alongside other results from various studies on the reduction of CO_2 to oxalates/oxalic acid.

Table 3.1: Summary of some recent studies on the electrochemical reduction of CO_2 to oxalate and oxalic acid in organic solvents using various electrodes and catholytes.

Entry	Applied Potential (V vs SHE)	Catholyte	Electrode	Catalyst (mM)	Average Current Density (mA/cm^2)	Average Faradaic Efficiency of Notable Products (%)	Formation rate ($mM\ cm^{-2}\ h^{-1}$)	Ref.
1	–2.40	$(CH_3)_4NClO_4$/ Propylene carbonate	Pb	No catalyst	Not reported	Oxalic acid (73.3) Glyoxylic acid (3.4) Formic acid (2.2) Carbon monoxide (11.0)	Not reported	[35]
2	–2.40	$(CH_3)_4NClO_4$/ Propylene carbonate	In	No catalyst	Not reported	Oxalic acid (0.1) Formic acid (1.3) Carbon monoxide (85.3)	Not reported	[35]
3	–1.80 to –2.80	$(CH_3)_4NCl$/ dimethylformamide	High-alloy steel	No catalyst	5	Oxalic acid (76)	Not reported	[36]
4	–2.50	$C_8H_2OClNO_4$/ Propylene carbonate	Pb	No catalyst	5.1	Oxalic acid (10)	Not reported	[36]
5	–1.80 to –2.80	C_8H_2ONF/ acetic anhydride	High-alloy steel	No catalyst	5.1	Oxalic acid (0.1)	Not reported	[36]
6	–2.80 to –3.80	$(CH_3)_4NCl$/ γ-butyrolactone	High-alloy steel	No catalyst	5	Oxalic acid (50)	Not reported	[36]
7	–1.96	n-Bu_4NClO_4/N,N-dimethylformamide	Hg	1.63 mM $C_6H_5COOCH_3$	1.6	Oxalic acid (84)	Not reported	[32]
8	–2.02	n-Bu_4NClO_4/N,N-dimethylformamide	Hg	2.1 mM C_6H_5CN	1.6	Oxalic acid (80)	Not reported	[32]

9	–2.20	$(C_2H_5)_4N(ClO_4)$/ Acetonitrile	Pb	No catalyst	1.92	Oxalic acid (<80)	Oxalic acid (0.0065)	[37]
10	–2.40	$(C_2H_5)_4N(BF_4)$/ Acetonitrile	Pb	No catalyst	5.967	Oxalic acid (13)	Oxalic acid (0.1113)	[38]
11	–2.40	$C_{16}H_{36}F_6NP$/ Acetonitrile	Pb	No catalyst	0.423	Oxalic acid (3)	Oxalic acid (0.00011)	[38]
12	–2.40	$[(C_2H_5)_4N(C_{11}H_{16}O_3Si)]$/ Acetonitrile	Pb	No catalyst	9.03	Oxalic acid (86)	Oxalic acid (0.1684)	[38]
13	–2.50	$(CH_3)_4NCl$/Propylene carbonate	Pb	No catalyst	14.0	Oxalic acid (60) Glyoxylic acid (3.2) Glycolic acid (6.3) Formic acid (13.8)	Oxalic acid (0.70)	[29]
14	–2.46	$(CH_3)_4NCl$/Propylene carbonate	Pb	No catalyst	13.7	Oxalic acid (59.6) Glyoxylic acid (8.2) Glycolic acid (9.2)	Oxalic acid (0.72) Glyoxylic acid (0.14) Glycolic acid (0.15)	This work
15	–2.46	$(CH_3)_4NCl$/Propylene carbonate	Pb	C_6H_5CN	16.9	Oxalic acid (72.4) Glyoxylic acid (9.4) Glycolic acid (10.8)	Oxalic acid (0.90) Glyoxylic acid (0.17) Glycolic acid (0.20)	This work

Note: The formation rate provided is averaged over the duration of the experiment in each case (5 h).

In this research, carried out in propylene carbonate at ambient temperature with a simple H-cell setup, our hypothesis has been confirmed. Our findings show an enhanced current density of approximately 17 mA cm^{-2} and a Faradaic yield for oxalate of 72%, setting a new benchmark for the area-normalised rate of oxalate formation at 1.65 mM $cm^{-2}\,h^{-1}$ (averaged over the initial hour) and 0.90 mM $cm^{-2}\,h^{-1}$ (averaged over 5 hours).

3.2 Experimental

3.2.1 Materials

The following materials were obtained from their respective suppliers and used without further purification: anhydrous propylene carbonate ($C_4H_6O_3$, Sigma-Aldrich, 99.7%), tetraethylammonium chloride ($C_8H_{20}ClN$, Sigma-Aldrich, 99.0%), sulfuric acid (H_2SO_4, Fisher Chemical, 95.0%), lead wire (Pb, Alfa Aesar, 1.0 mm diameter, 99.99% metals basis), lead rod (Pb, Alfa Aesar, 5 mm diameter, 99.99% metals basis), platinum wire (Pt, Alfa Aesar, 1.0 mm diameter, 99.99%), platinum foil (Pt, Alfa Aesar, 0.25 mm, 99.99% metals basis), anhydrous benzonitrile, (C_7H_5N, Sigma-Aldrich, 99%), Nafion membrane (Nafion-117, manufactured by Fuel Cell Store). Argon and CO_2 were supplied by BOC (99.99%).

3.3 Electrochemical Methods and Products Analysis

3.3.1 Cyclic Voltammetry (CV)

The cyclic voltammetry measurements were performed in a single cell, using a Pb wire working electrode (area = 0.64 cm^2), a saturated calomel reference electrode (SCE) and a Pt wire counter electrode as depicted in Figure 3.1.

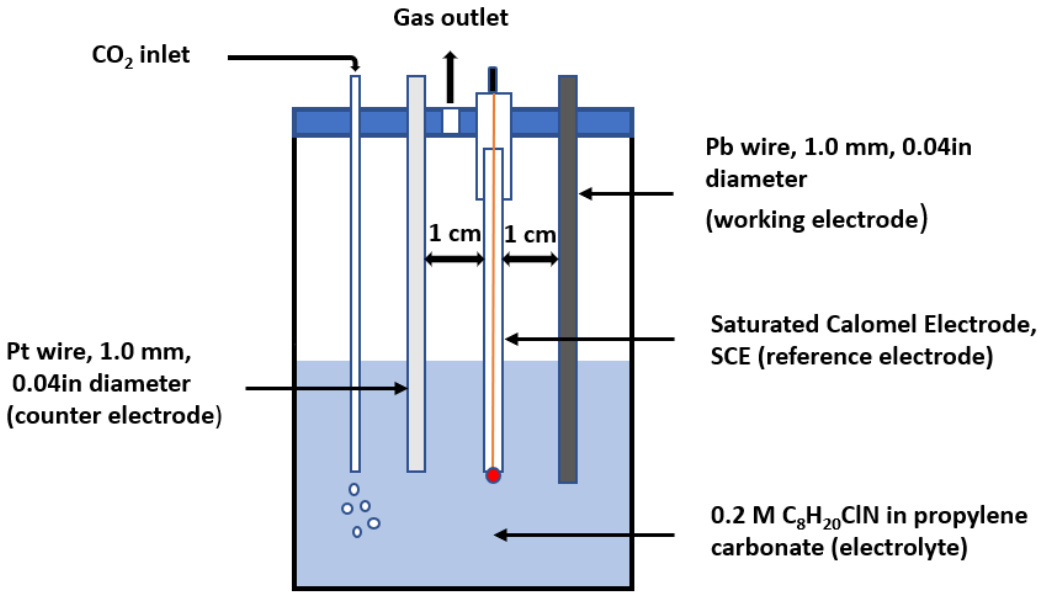

Figure 3.1: Schematic diagram of the single-cell experimental set-up used for the cyclic voltammetry experiments, using lead as a working electrode, platinum as a counter electrode and a saturated calomel electrode as the reference electrode at a temperature of 25 °C.

After setting up the cell as illustrated above (Figure 3.1), the electrolyte was purged with argon (Ar) for 20 minutes to remove any dissolved oxygen before running the cyclic voltammetry measurements using a CHI potentiostat. Following this control experiment, CO_2 was purged for an additional 20 minutes before taking another reading to observe the changes in the cyclic voltammograms due to a CO_2-saturated atmosphere. To assess the impact of benzonitrile on CO_2 reduction in the organic solvent, benzonitrile was introduced into the electrolytic solution, followed by an additional 20-minute purging with CO_2. Subsequently, cyclic voltammetry was conducted, and the results were recorded. To optimise the catalytic conditions within the system, various concentrations of benzonitrile (1 mM, 2 mM, 4 mM, 6 mM, 8 mM, and 10 mM) were examined. However, only marginal alterations were detected in the voltammograms when the benzonitrile quantity exceeded 2 mM, as depicted in Figure 3.2. Consequently, a concentration of 2 mM was consistently utilised in the subsequent results presented below.

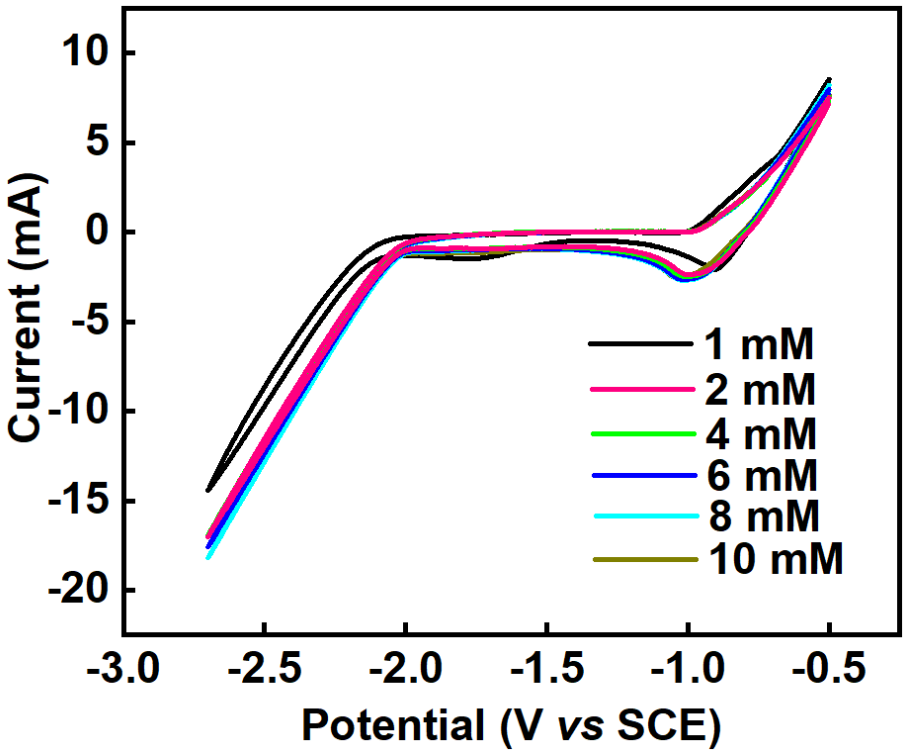

Figure 3.2: Cyclic voltammetry investigating the optimum concentration of the benzonitrile electrocatalyst needed for the electrochemical reduction of CO_2 in propylene carbonate, using lead as a working electrode with a surface area of 1.40 cm^2, platinum as a counter electrode and a saturated calomel electrode as the reference electrode at a temperature of 25 °C and scan rate of 50 mV/s.

3.3.2 Chronoamperometry

Chronoamperometric experiments (bulk electrolysis) were performed using three-electrode configurations in an H-cell having two compartments for the anolyte and catholyte separated by a Nafion membrane (Nafion-117), as shown in Figure 3.3. The working electrode is a Pb rod, having a surface area of 3.5 cm^2, and the reference electrode (Saturated Calomel Electrode) was placed in the catholyte (0.2 M tetraethylammonium chloride in propylene carbonate) while the counter electrode (platinum foil) was placed in the anolyte compartment containing 0.5 M H_2SO_4. The chronoamperometric measurement was conducted for 5 hours at each investigated potential. To compare the outcome with the previously reported findings made with different reference electrodes, the potentials measured against SCE in this work were converted to the standard hydrogen electrode (SHE) scale using the equation $E_{SHE} = E_{SCE} + 0.241V$, (where E_{SHE} = the potential relative to the Standard Hydrogen Electrode, E_{SCE} = the potential relative to the Saturated Calomel Electrode, 0.241 V = the standard potential difference between SCE and SHE),[39] while the potentials reported in other similar research, originally against Ag/AgCl and other reference electrodes, were also converted to SHE accordingly.[39,40]

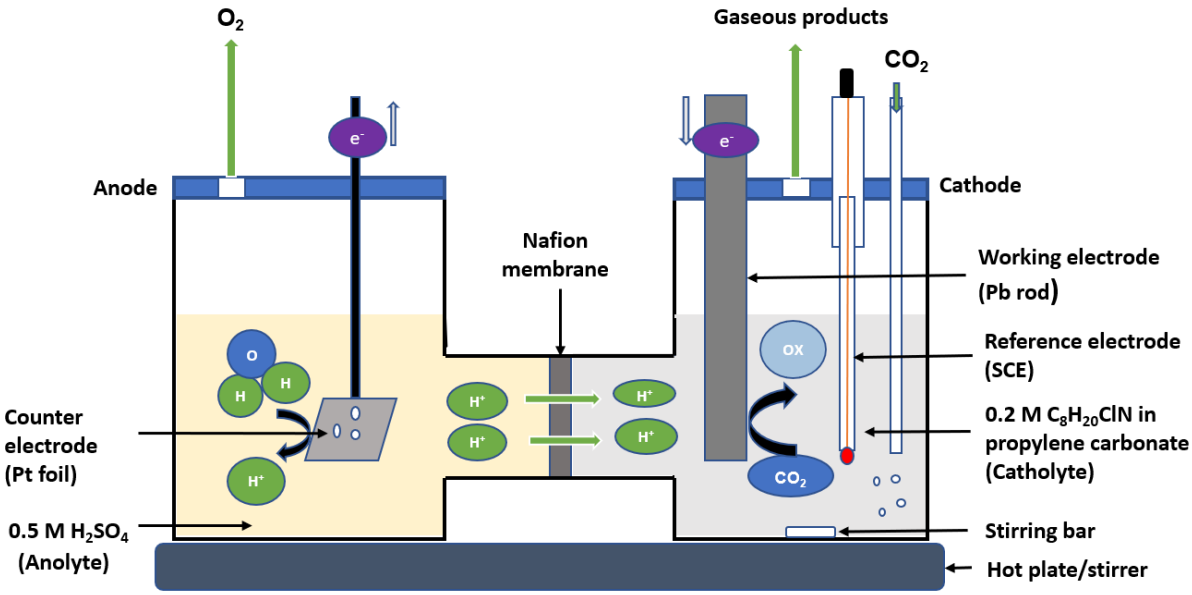

Figure 3.3: A schematic diagram of the H-cell used for bulk electrolysis of CO_2 in 0.2 M tetraethylammonium chloride and propylene carbonate. The right-hand compartment of the cell is the catholyte, where the working electrode (Pb rod with a surface area of 3.5 cm2) and a reference electrode (SCE) are placed, while the left-hand side contains the anolyte where the counter electrode (platinum foil with a surface area of 4 cm^2) was placed. The two compartments are separated by a Nafion membrane. The reaction was conducted at a temperature of 25 °C for 5 hours.

Figure 3.3 illustrates the configuration of the H-cell setup. Before each experiment, the Pb electrode was polished with sandpaper, sonicated in acetone for approximately 10 minutes, rinsed with anhydrous propylene carbonate, and dried under argon to eliminate any lead oxide impurities or moisture from the surface. The working electrode, with a total surface area of 3.5 cm^2, was immersed in 40 mL of the catholyte, while the counter electrode, with a total surface area of 4 cm^2, was immersed in 40 mL of the anolyte solution. The cathodic compartment was purged with Ar for 20 minutes to eliminate any dissolved oxygen, followed by an additional 20-minute purge with CO_2 to saturate the electrolyte. Chronoamperometric measurements were then initiated under a continuous supply of CO_2. The measurement was carried out in a closed cell at a range of applied potentials for 5 hours at each potential, starting from −2.2 V and ranging to −2.7 V (vs SCE) for both (1) 0.2 M tetraethylammonium chloride in propylene carbonate and (2) 0.2 M tetraethylammonium chloride in propylene carbonate with 2 mM benzonitrile. During the electrolysis, samples of

the electrolyte solution were collected hourly for product analysis using high-performance liquid chromatography-mass spectrometry (HPLC-MS).

3.3.3 High-Performance Liquid Chromatography-Mass Spectrometry (HPLC-MS)

The products were analysed by an Agilent high-performance liquid chromatography-mass spectrometry (HPLC-MS) using an Aminex HPX-87H, 300 mm × 7.8 mm column. The mobile phase used was 0.1% formic acid in HPLC grade acetonitrile and 0.1% formic acid in water in a ratio of 30:70, respectively. The HPLC machine was set at a flow rate of 0.6 mL/min, at a temperature of 55 ^{o}C, and at a detector wavelength of 210 – 230 nm. Before analysing the experimental products, the standard solutions of each target product were analysed to establish standard calibration curves. Once the LC-MS peaks were identified from the sample solutions, the peak areas corresponding to each product (oxalic, glyoxylic, and glycolic acids) were inserted into the equations of the graphs in the standard calibration curves depicted in Figure 3.4 (a-c). This allowed us to determine the actual concentration of the respective products.

Figure 3.4 (d) depicts an example HPLC chromatogram confirming the reduction of CO_2 to the three detectable liquid products in a catalysed and uncatalyzed system at an applied potential of −2.2 (V vs. SCE).

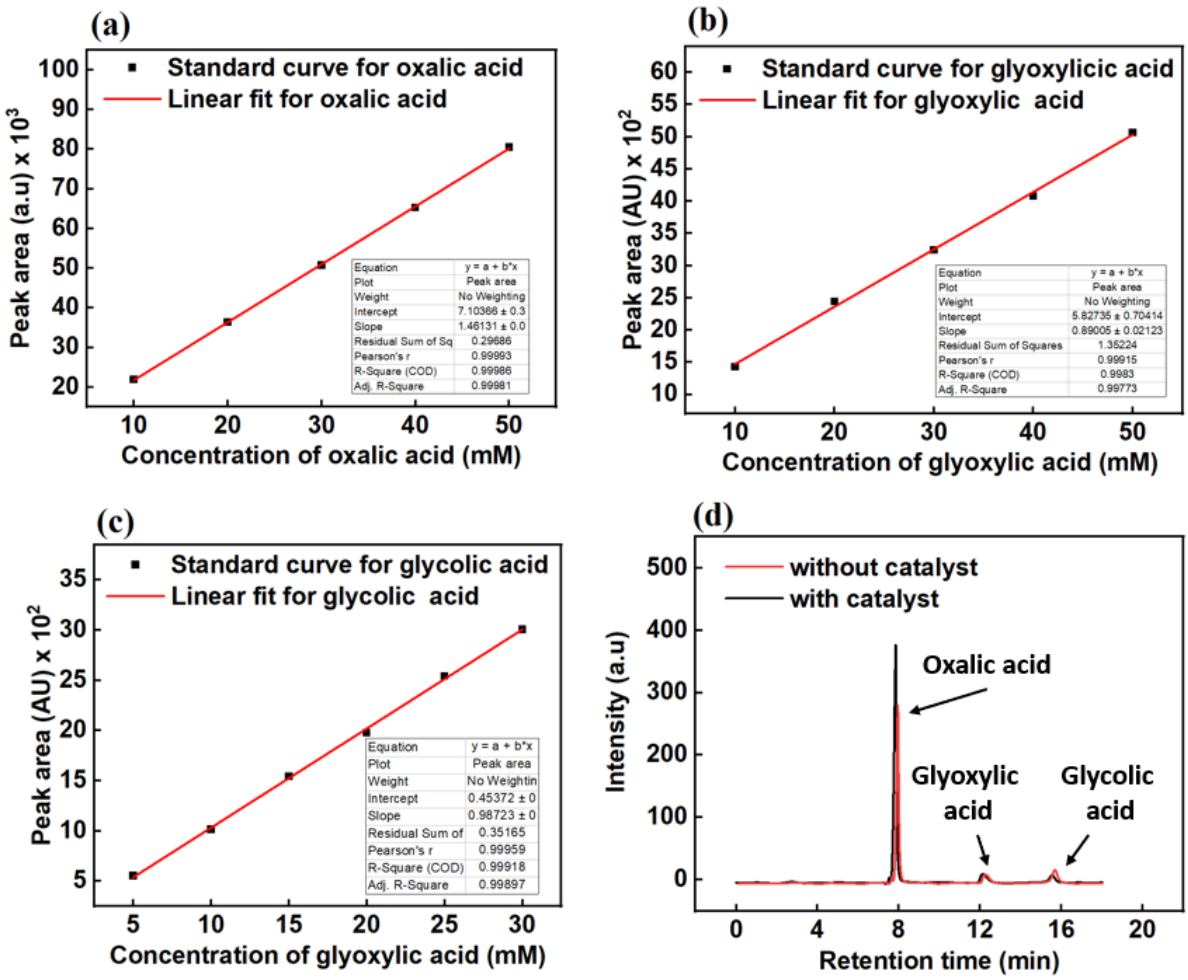

Figure 3.4: Standard calibration curves for (a) oxalic acid, (b) glyoxylic acid, (c) glycolic acid, and (d) HPLC signal showing the chromatograms′ retention time and the peak intensity for the carboxylic acids detected in propylene carbonate (red) and propylene carbonate/benzonitrile (black) at an applied potential of −2.2 (V vs SCE).

3.4 Results and Discussion

Figure 3.5 presents cyclic voltammograms of the Pb electrode in an electrolyte saturated with Ar and CO_2, ranging from −0.5 V to −2.8 V (vs. SCE) at a sweep rate of 50 mV/s. The cyclic voltammograms were recorded under four different conditions: (i) 0.2 M tetraethylammonium chloride in propylene carbonate under argon (black line), (ii) 0.2 M tetraethylammonium chloride in propylene carbonate with 2 mM benzonitrile under argon (red line), (iii) 0.2 M tetraethylammonium chloride in propylene carbonate under CO_2 (blue line) and (iv) 0.2 M tetraethylammonium chloride in propylene carbonate with 2 mM benzonitrile under CO_2 (green line). The cyclic voltammograms in Figure 3.5 demonstrate an increased current density across all measured potentials under CO_2 compared to Ar. Additionally, introducing benzonitrile to the cell further enhances the current density.

Together, these results suggested that CO_2 reduction occurred when CO_2 was purged into the electrolyte, and that benzonitrile could be catalysing this reaction.

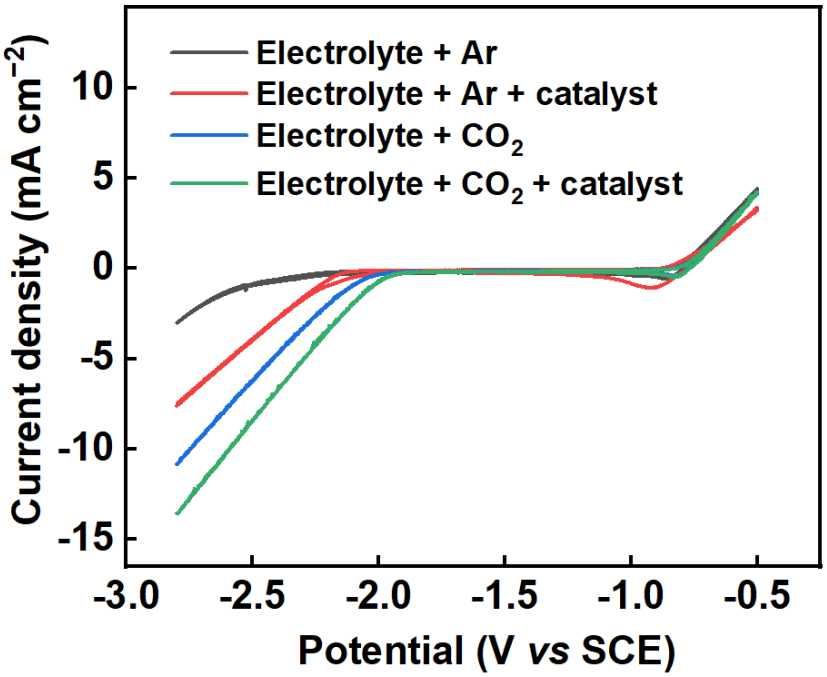

Figure 3.5: Cyclic voltammograms showing the effects of benzonitrile on the reduction potential of CO_2 in 0.2 M tetraethylammonium chloride in propylene carbonate, using lead wire as a working electrode with a surface area of 0.64 cm^2, platinum wire as a counter electrode, and a saturated calomel electrode as the reference electrode at a temperature of 25 °C and scan rate of 50 mV/s. Colour codes are as follows: 0.2 M tetraethylammonium chloride in propylene carbonate under argon (black line), 0.2 M tetraethylammonium chloride in propylene carbonate with 2 mM benzonitrile under argon (red line), 0.2 M tetraethylammonium chloride in propylene carbonate under CO_2 (blue line) and 0.2 M tetraethylammonium chloride in propylene carbonate with 2 mM benzonitrile under CO_2 (green line).

3.4.1 Probing CO_2 Reduction

To determine whether CO_2 reduction was occurring and to identify possible reaction products, we carried out bulk electrolysis at six fixed potentials (ranging from −2.2 V to −2.7 V versus SCE) for 5 hours each. The current densities were evaluated relative to the surface area of the working electrodes submerged in the electrolyte solution, measured in mA/cm^2. Each experiment was conducted three times at each set potential for the same duration to confirm reproducibility and to establish the error boundaries for the average values of current density, Faradaic efficiency, and product yield. Error bars were determined based on the standard deviations from the average values of each parameter. Figure 3.6 presents the mean

current densities from the three repeated experiments, along with their error bars for all set potentials. Generally, current densities tend to rise with increased applied potentials.

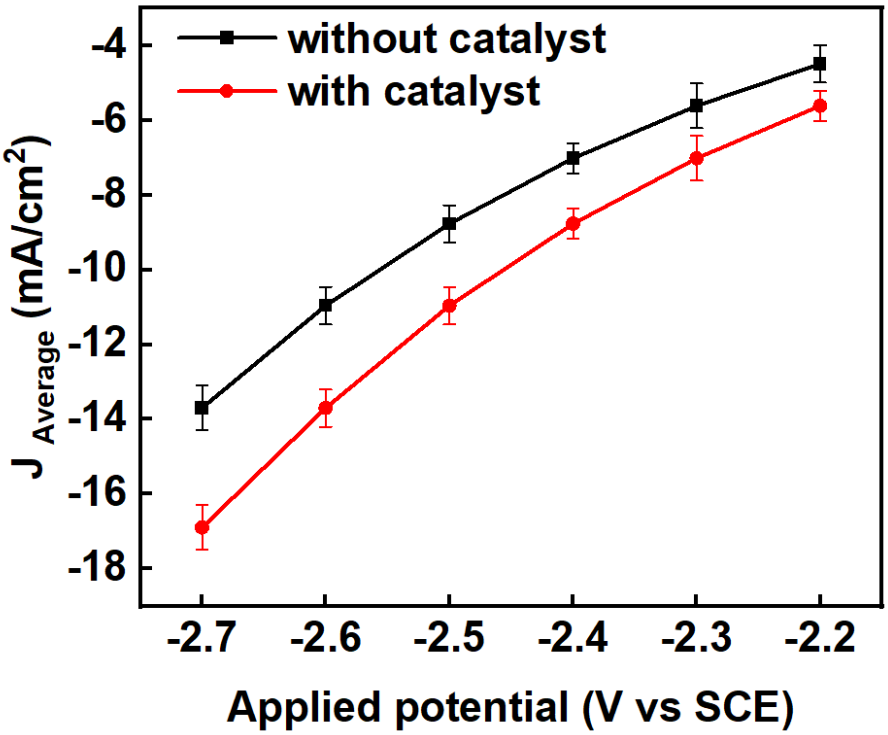

.

Figure 3.6: Showing the effect of benzonitrile on the average current densities of triplicate experiments across the applied potentials in propylene carbonate (black line) and propylene carbonate plus 2 mM benzonitrile (red line), using Pb as a working electrode with a surface area of 3.5 cm^2, Pt foil as counter electrode and SCE as a reference electrode. The experiments were conducted at a temperature of 25 °C and current densities were averaged over 5 hours for each applied potential; the error bars were calculated as standard deviation from the mean of the triplicate experiment (n = 3).

3.4.2 Faraday Efficiency and Yield

Figures 3.7-3.12 graphically present the average Faradaic efficiencies and the corresponding oxalic acid concentrations obtained at each applied potential (from –2.2 to –2.7 V vs SCE). The Faradaic efficiency for oxalic acid generally increased with the magnitude of the applied potential, reaching its peak at −2.5 V vs SCE (−2.26 V vs SHE). Beyond this point, the Faradaic efficiencies declined for both the catalyzed and uncatalyzed reactions. This decrease could be attributed to the hydrogen evolution reaction or the conversion of the primary product (oxalic acid) into secondary products like glyoxylic and glycolic acid.

The Faradaic efficiency of the various products was calculated using Equation 1.9 in section 1.3.4 Kinetics of CO2 Electroreductionof Chapter 1. The Faradaic efficiency for oxalic acid and

other secondary products obtained across all the applied potentials are presented in Figures 3.7 – 3.12:

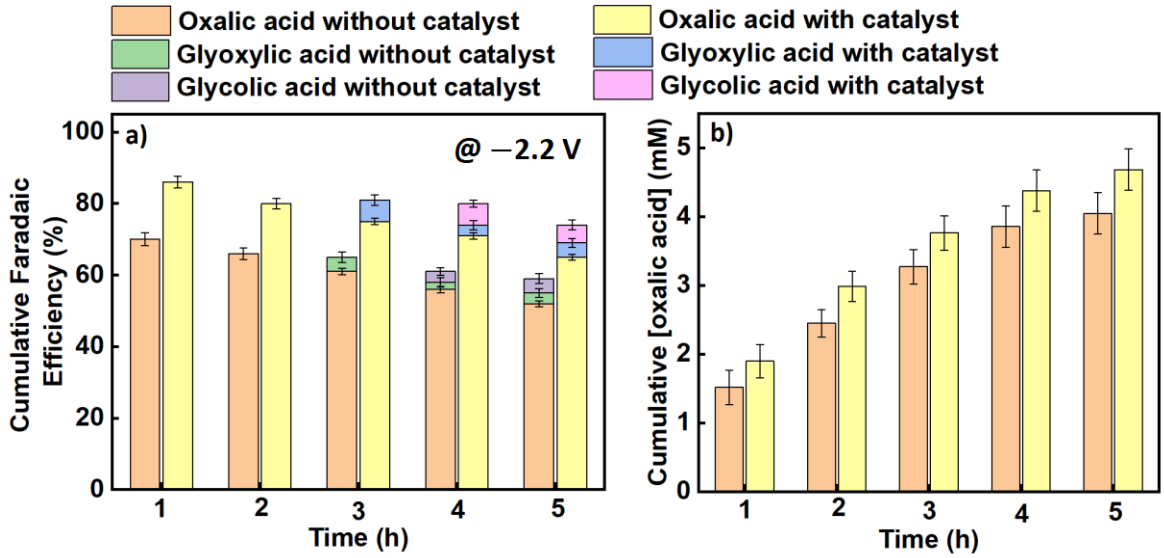

Figure 3.7: The effect of benzonitrile on (a) the Faradaic efficiencies for the production of oxalic acid and its accompanying by-products in propylene carbonate, (b) the concentration of oxalic acid formed using Pb as a working electrode and Pt foil as a counter electrode at an applied potential of –2.2 V vs SCE in an H-cell at a temperature of 25 °C. Triplicate experiments were performed to obtain the error margin and the results are calculated as the mean ± standard deviation (n = 3).

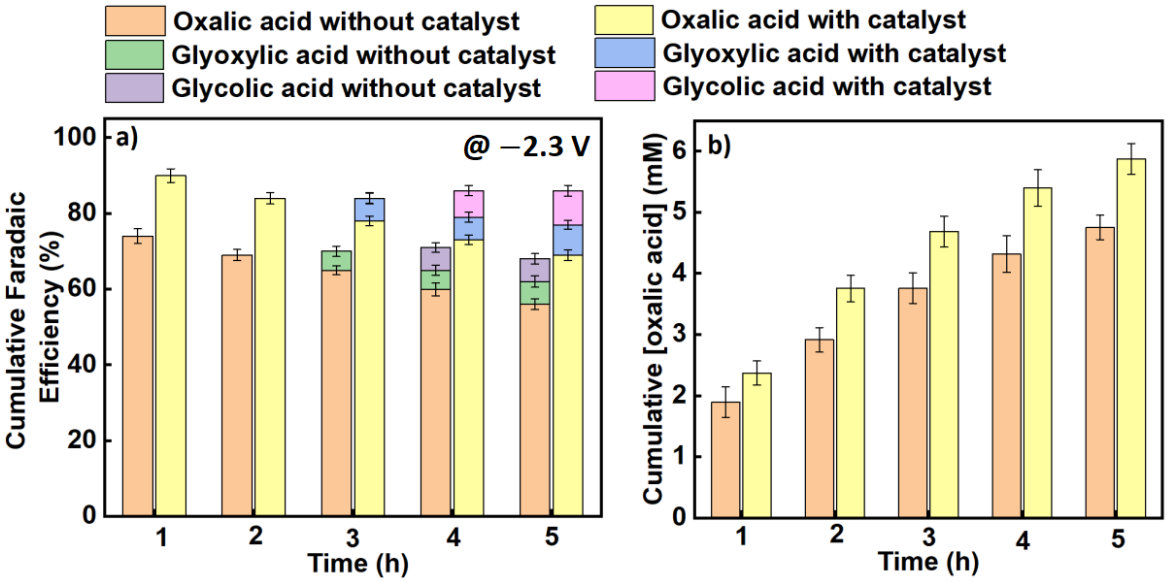

Figure 3.8: The effect of benzonitrile on (a) the cumulative Faradaic efficiencies for the production of oxalic acid and its accompanying by-products in propylene carbonate, (b) the cumulative concentration of oxalic acid formed using Pb as a working electrode and Pt foil as a counter electrode at an applied potential of –2.3 V vs SCE in an H-cell at a temperature of 25 °C. Triplicate experiments were performed to obtain the error margin, and the results are calculated as the mean ± standard deviation (n = 3).

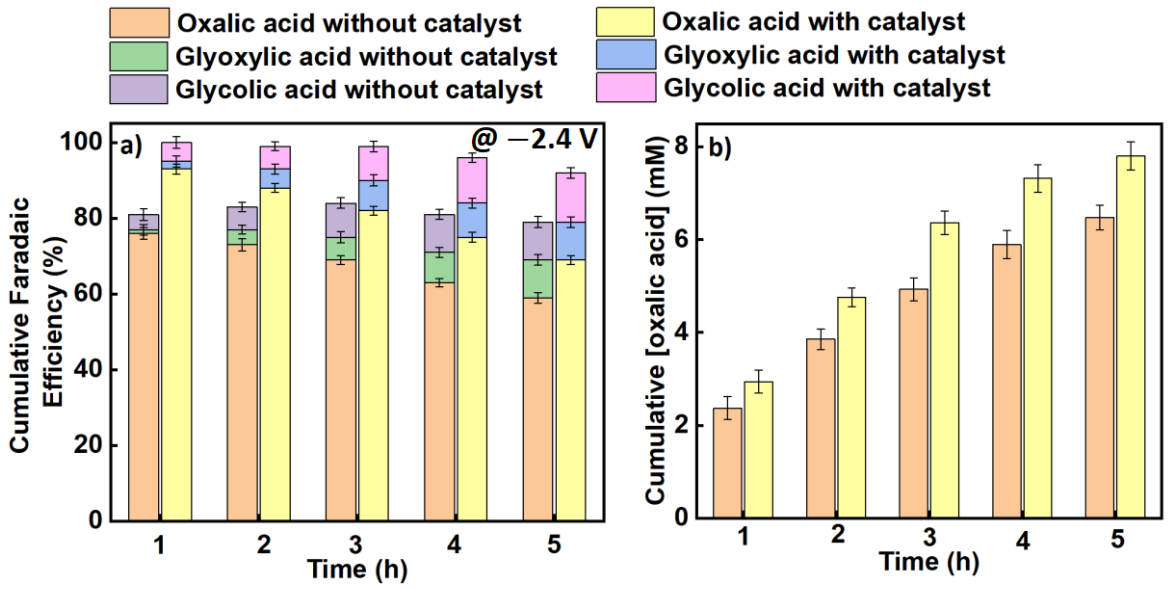

Figure 3.9: The effect of benzonitrile on (a) the cumulative Faradaic efficiencies for the production of oxalic acid and its accompanying by-products in propylene carbonate, (b) the cumulative concentration of oxalic acid formed using Pb as a working electrode and Pt foil as a counter electrode at an applied potential of –2.4 V vs SCE in an H-cell at a temperature of 25 °C. Triplicate experiments were performed to obtain the error margin and the results are calculated as the mean ± standard deviation (n = 3).

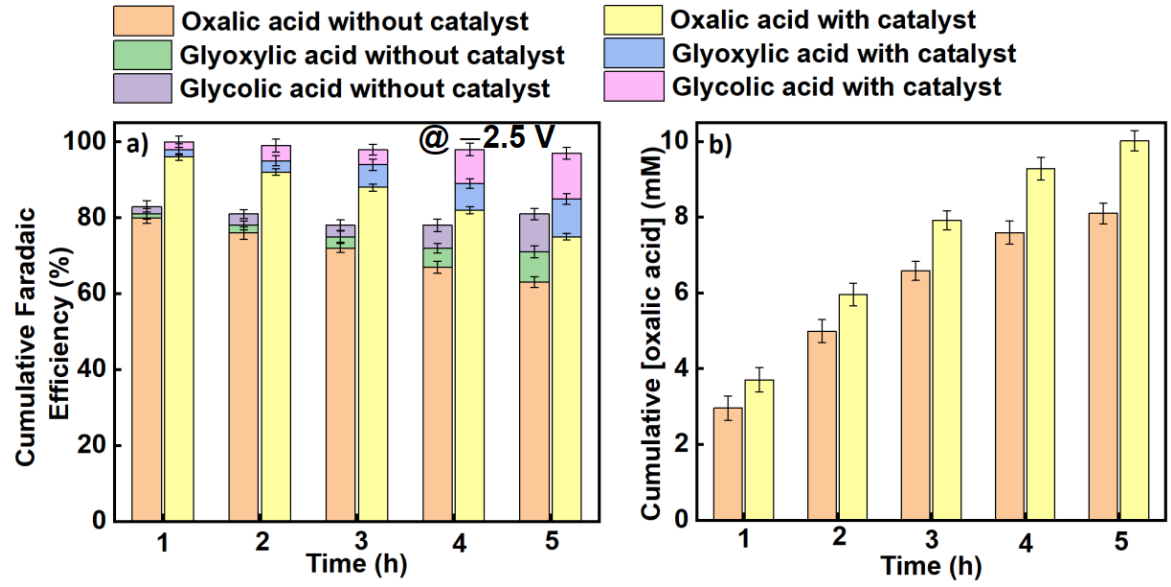

Figure 3.10: The effect of benzonitrile on (a) the cumulative Faradaic efficiencies for the production of oxalic acid and its accompanying by-products in propylene carbonate, (b) the cumulative concentration of oxalic acid formed using Pb as a working electrode and Pt foil as a counter electrode at an applied potential of –2.5 V vs SCE in an H-cell at a temperature of 25 °C. Triplicate experiments were performed to obtain the error margin and the results are calculated as the mean ± standard deviation (n = 3).

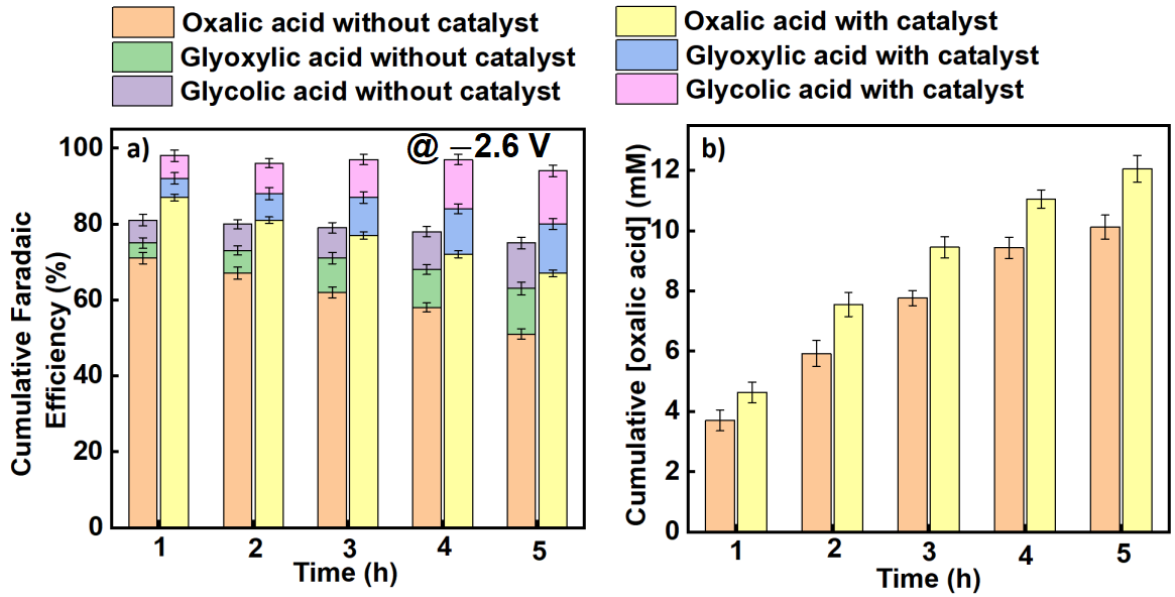

Figure 3.11: The effect of benzonitrile on (a) the cumulative Faradaic efficiencies for the production of oxalic acid and its accompanying by-products in propylene carbonate, (b) the cumulative concentration of oxalic acid formed using Pb as a working electrode and Pt foil as a counter electrode at an applied potential of –2.6 V vs SCE in an H-cell at a temperature of 25 °C. Triplicate experiments were performed to obtain the error margin and the results are calculated as the mean ± standard deviation (n = 3).

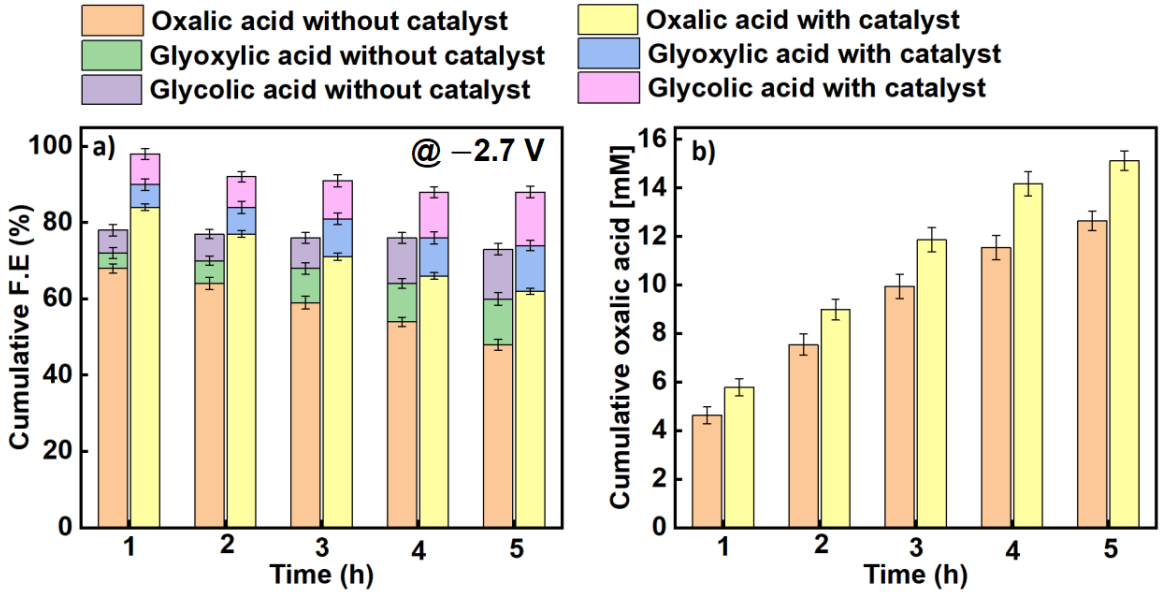

Figure 3.12: The effect of benzonitrile on (a) the Faradaic efficiencies for the production of oxalic acid and its accompanying by-products in propylene carbonate, (b) the concentration of oxalic acid formed using Pb as a working electrode and Pt foil as a counter electrode at an applied potential of –2.7 V vs SCE in an H-cell at a temperature of 25 °C. Triplicate experiments were performed to obtain the error margin, and the results are calculated as the mean ± standard deviation (n = 3).

Table 3.2 presents the average Faradaic efficiency for oxalic acid and the identifiable by-products at each potential. In every instance, the total Faradaic efficiency falls short of 100%, probably because of the competing hydrogen evolution. This occurrence could also be linked to two specific factors. Primarily, as the reaction time extends, a portion of the produced oxalic acid is transformed into secondary products. Subsequently, the water concentration in the catholyte progressively escalates over time, a result of the electro-osmotic pull of water from the aqueous anolyte solution to the cathode side of the cell.[29,41] Consequently, this will result in a heightened frequency of competing hydrogen evolution reactions. Thus, the observed trends in Faradaic efficiency concerning potential and reaction time align with findings from prior literature on this phenomenon.[29]

Table 3.2: Showing the effect of benzonitrile on the average Faradaic efficiencies of the notable products of electrochemical reduction of CO_2 to oxalic acid in propylene carbonate on a Pb cathode at an applied potential of −2.2 to −2.7 (V vs. SCE) in an H-cell at 25 °C, averaged over 5 hours.

Entry	Applied Potential (V vs SCE)	Average Faradaic Efficiency of the Products (%)					
		Oxalic Acid		Glyoxylic Acid		Glycolic Acid	
		Without catalyst	With catalyst	Without catalyst	With catalyst	Without catalyst	With catalyst
1	−2.2	61.17	75.40	1.80	2.60	1.40	2.25
2	−2.3	64.40	78.84	3.20	4.0	2.40	3.20
3	−2.4	68.22	82.25	5.80	6.83	7.80	9.01
4	−2.5	71.60	86.60	3.80	5.60	4.8	6.20
5	−2.6	63.80	77.80	8.2	9.40	8.60	10.20
6	−2.7	59.60	72.40	8.2	9.40	9.2	10.8

3.4.3 Yield of Carboxylic Acids Detected

Table 3.3 illustrates the average concentrations of different carboxylic acids obtained under varying applied potentials. The main solution-phase products identified include oxalic, glyoxylic, and glycolic acids. Across all scenarios, employing benzonitrile as a catalyst enhances the production yields of oxalate/oxalic acid, with marginal upticks in glyoxylic and glycolic acid yields. The rise in glyoxylic and glycolic acid concentrations over time stems from the transformation of a portion of the initially generated oxalic acid into secondary products.

Table 3.3: Showing the effect of benzonitrile on the yield of the notable products of electrochemical reduction CO_2 in propylene carbonate on a Pb cathode at an applied potential of −2.2 to −2.7 (V vs. SCE) in an H-cell at 25 °C, averaged over 5 hours.

Entry	Applied Potential (V vs SCE)	Product Concentration [mM]					
		Oxalic Acid		Glyoxylic Acid		Glycolic Acid	
		Without catalyst	With catalyst	Without catalyst	With catalyst	Without catalyst	With catalyst
1	−2.2	4.05	4.68	0.23	0.31	0.35	0.39
2	−2.3	4.75	5.88	0.56	0.75	0.60	0.84
3	−2.4	6.47	7.81	1.09	1.11	1.09	1.45
4	−2.5	8.10	10.12	1.12	1.35	1.21	1.62
5	−2.6	10.14	12.05	2.38	2.45	2.38	2.64
6	−2.7	12.65	15.81	2.53	3.06	2.65	3.57

3.4.3 Formation Rate

The initial formation rate of oxalate/oxalic acid obtained after the first 1 hour of bulk electrolysis at a potential of −2.70 V versus SCE at 25 °C as a function of electrode area is 1.32 mM cm^{-2} h^{-1} an uncatalysed medium and 1.65 mM cm^{-2} h^{-1} in a catalysed medium, as shown in Figure 3.13. However, the formation rates decrease with reaction time, resulting in an average formation rate of 0.72 mM cm^{-2} h^{-1} and 0.9 mM cm^{-2} h^{-1} (averaged over 5 hours) for the catalysed and uncatalysed reaction, respectively (see the last two entries of Table 3.1). Comparatively, the average formation rate of 0.9 mM cm^{-2} h^{-1} recorded in this research under optimal conditions (−2.70 V versus SCE at 25 °C with catalyst is a significant improvement from the highest reported value of 0.70 mM cm^{-2} h^{-1} reported by Boor *et al.*,[29] under similar conditions but using a slightly more negative applied potential of −2.70 V versus Ag/AgCl (−2.75 V versus SCE). Figure 3.13 illustrates the initial formation rates for both the uncatalysed and catalyzed systems across the range of applied potentials (−2.2 V to −2.7 V vs SCE).

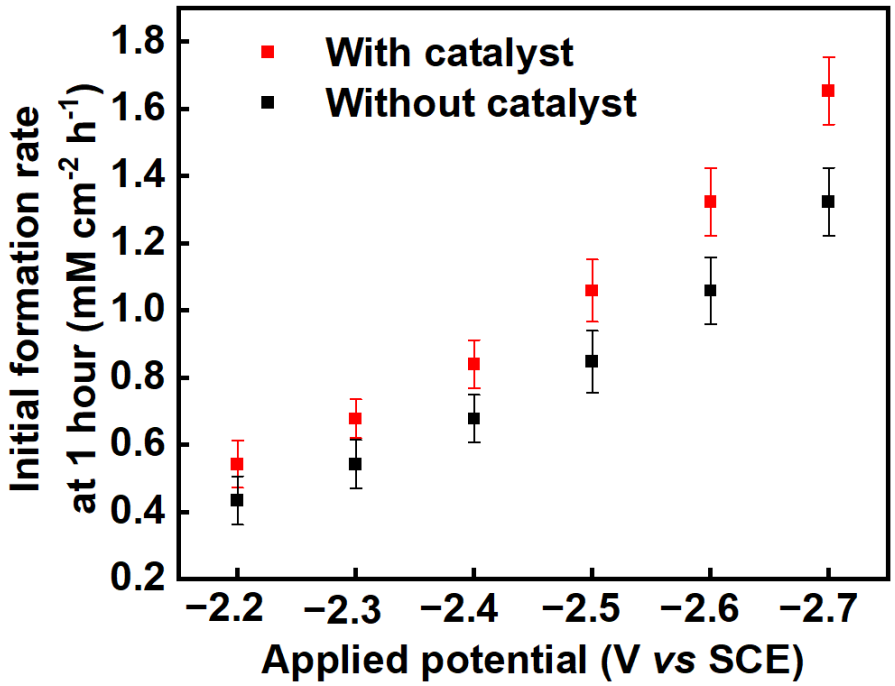

Figure 3.13: The formation rates of oxalic acid on a Pb cathode in propylene carbonate over the first hour of electrolysis across the range of applied voltages from −2.2 V to −2.7 V vs SCE in an uncatalysed system (black squares) and a system catalysed using benzonitrile (red squares).

3.4.4 Analysis of Secondary Products

Figure 3.14 shows the graphical representation of the average yield of the secondary products obtained across all the applied potentials in the presence and absence of a catalyst.

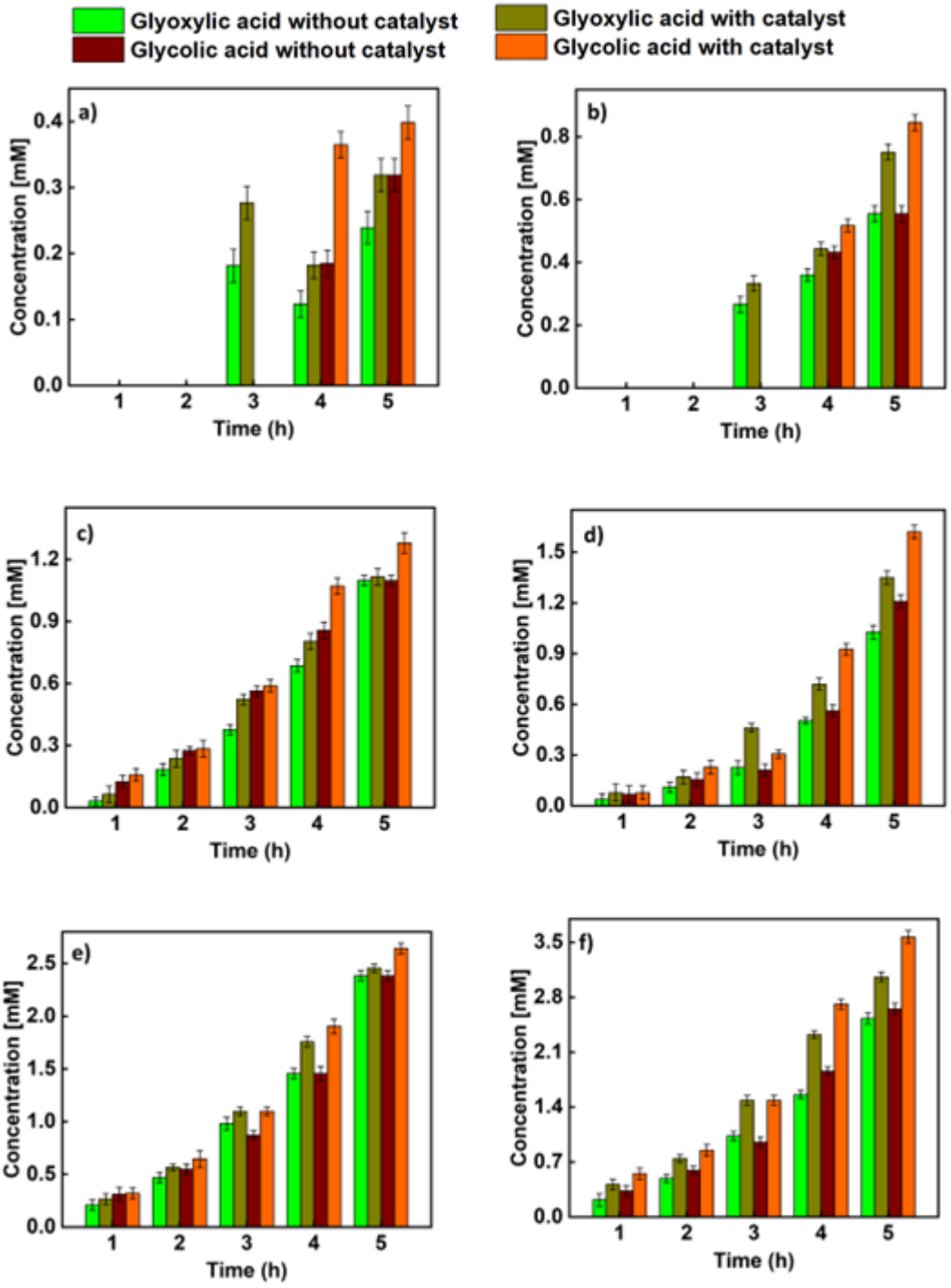

s

Figure 3.14: The concentration of notable by-products accompanying the electrochemical reduction of CO_2 to oxalic acid in propylene carbonate and propylene carbonate/benzonitrile on a Pb cathode at an applied potential of a) −2.2 V, b) −2.3 V, c) −2.4 V, d) −2.5 V, e) −2.6 V, f) −2.7 V vs. SCE in an H-cell at 25 °C for 5 hours.

3.5 Conclusion

In this study, we investigated the electrochemical reduction of carbon dioxide in propylene carbonate electrolytes on a Pb cathode, both with and without benzonitrile as a homogeneous catalyst. Our findings without the catalyst align well with those previously reported by Boor *et al.*,[29] also obtained on a Pb cathode in propylene carbonate. Interestingly, we have recorded a slight increase in the formation rate after the introduction of the benzonitrile catalyst to the system, as indicated in the last three (3) entries of Table 3.1. Therefore, our investigation validates the previous findings and suggests that under these conditions, consistent carbon dioxide reduction can be achieved in terms of current densities, product distributions, and formation rates. These results will be invaluable to researchers in the electrochemical carbon dioxide reduction field, offering dependable model reactions for further exploration.

The use of benzonitrile as a homogeneous electrocatalyst was found to boost both the Faradaic and reaction yields for the production of oxalate/oxalic acid, while also speeding up its rate of formation. Furthermore, these enhancements were also observed, albeit to a lesser degree, for the by-products, glyoxylic acid and glycolic acid. These boosts in Faradaic yield were achieved at the expense of the competing hydrogen evolution reaction, which is undesirable in the process.

The use of benzonitrile as a homogeneous catalyst for the electrochemical reduction of CO_2 in organic solvent exhibits some level of performance that improves the process. The current densities and percentage yield of the product are generally higher in the system with benzonitrile. A new record rate of formation of oxalate/oxalic acid of 0.9 ± 0.35 mM cm^{-2} h^{-1} was obtained at a voltage of –2.7 V vs SCE (–2.46 V vs SHE) using a benzonitrile electrocatalyst, at which potential a current density of nearly 17 mA cm^{-2} could be obtained, delivering oxalate with a Faradaic yield of 72%. These metrics represent some of the most notable achievements documented thus far for this conversion, signalling the potential for further advancement in the electrochemical reduction of carbon dioxide to C_{2+} products using oxalate.

3.6 References

1 L. Sun, G. K. Ramesha, P. V Kamat and J. F. Brennecke, *Langmuir*, 2014, **30**, 6302–6308.

2 J. Schneider, H. Jia, J. T. Muckerman and E. Fujita, *Chem. Soc. Rev.*, 2012, **41**, 2036–2051.

3 M. König, J. Vaes, E. Klemm and D. Pant, *Science*, 2019, **19**, 135–160.

4 S. Langsdorf, *Green Eur. Found.,* 2011,**1**, 9

5 D. T. Whipple and P. J. A. Kenis, *J. Phys. Chem. Lett.*, 2010, **1**, 3451–3458.

6 D. Chu, G. Qin, X. Yuan, M. Xu, P. Zheng and J. Lu, *ChemSusChem Chem. Sustain. Energy Mater.*, 2008, **1**, 205–209.

7 N. S. Spinner, J. A. Vega and W. E. Mustain, *Catal. Sci. Technol.*, 2012, **2**, 19–28.

8 Y. Chen, C. W. Li and M. W. Kanan, *J. Am. Chem. Soc.*, 2012, **134**, 19969–19972.

9 E. E. Barton, D. M. Rampulla and A. B. Bocarsly, *J. Am. Chem. Soc.*, 2008, **130**, 6342–6344.

10 B. A. Rosen, A. Salehi-Khojin, M. R. Thorson, W. Zhu, D. T. Whipple, P. J. A. Kenis and R. I. Masel, *Science (80-.).*, 2011, **334**, 643–644.

11 B. Eneau-Innocent, D. Pasquier, F. Ropital, J.-M. Léger and K. B. Kokoh, *Appl. Catal. B Environ.*, 2010, **98**, 65–71.

12 I. A. Novoselova, S. V Kuleshov and A. A. Omel'chuk, *Sustainable Energy and Fuels*, 2021, pp. 113–136.

13 A. R. Paris and A. B. Bocarsly, *ACS Catal.*, 2019, **9**, 2324–2333.

14 J. S. Yoo, R. Christensen, T. Vegge, J. K. Nørskov and F. Studt, *ChemSusChem*, 2016, **9**, 358–363.

15 J. T. Feaster, C. Shi, E. R. Cave, T. Hatsukade, D. N. Abram, K. P. Kuhl, C. Hahn, J. K. Nørskov and T. F. Jaramillo, *Acs Catal.*, 2017, **7**, 4822–4827.

16 P. Duarah, D. Haldar, V. S. K. Yadav and M. K. Purkait, *J. Environ. Chem. Eng.*, 2021, **9**, 106394.

17 S. D. Rihm, M. K. Kovalev, A. A. Lapkin, J. W. Ager and M. Kraft, 2023, 1697–1710.

18 C. Ampelli, C. Genovese, D. Cosio, S. Perathoner and G. Centi, *Chem. Eng. Trans.*, 2019, **74**, 1285–1290.

19 S. E. Jerng and B. M. Gallant, *science*, 2022, 104558.

20 H. Ooka, M. C. Figueiredo and M. T. M. Koper, *Langmuir*, 2017, **33**, 9307–9313.

21 C. Chen, J. F. Khosrowabadi Kotyk and S. W. Sheehan, *Chem*, 2018, **4**, 2571–2586.

22 Y. Chen, L. Wang, Z. Yao, L. Hao, X. Tan, J. Masa, A. W. Robertson and Z. Sun, *Wuli Huaxue Xuebao/ Acta Phys. Chim. Sin.*, 2022, **38**, 1–20.

23 K. Kang, M. Zhang, L. Yue, W. Chen, Y. Dai, K. Lin, K. Liu, J. Lv, Z. Guan and S. Xiao, *Cells*, 2023, **12**, 771.

24 P. Santawaja, S. Kudo, A. Mori, A. Tahara, S. Asano and J. Hayashi, *ACS Sustain. Chem. Eng.*, 2020, **8**, 13292–13301.

25 E. Schuler, M. Demetriou, N. R. Shiju and G. M. Gruter, *ChemSusChem*, 2021, **14**, 3636–3664.

26 National Center for Biotechnology Information. "PubChem Compound Summary for ACID 971, Oxalic Acid" *PubChem*, https://pubchem.ncbi.nlm.nih.gov/compound/Oxalic-Acid. Accessed 30 August, 2023.

27 Oxalic acid specific uses, http://www.lubonchem.com/blog/?p=993, Accessed 30th August, 2023.

28 A. C. Garcia, C. Sánchez-Martínez, I. Bakker and E. Goetheer, *ACS Sustain. Chem. Eng.*, 2020, **8**, 10454–10460.

29 V. Boor, J. E. B. M. Frijns, E. Perez-Gallent, E. Giling, A. T. Laitinen, E. L. V. Goetheer, L. J. P. Van Den Broeke, R. Kortlever, W. De Jong, O. A. Moultos, T. J. H. Vlugt and M. Ramdin, *Ind. Eng. Chem. Res.*, 2022, **61**, 14837–14846.

30 M. Marx, H. Frauendorf, A. Spannenberg, H. Neumann and M. Beller, *JACS Au*, 2022, **2**, 731–744.

31 G. Filardo, S. Gambino, G. Silvestri, A. Gennaro and E. Vianello, *J. Electroanal. Chem.*, 1984, **177**, 303–309.

32 A. Gennaro, A. A. Isse, J. M. Savéant, M. G. Severin and E. Vianello, *J. Am. Chem. Soc.*, 1996, **118**, 7190–7196.

33 T. E. Commission, *Off. J. Eur. Union*, 2021, **16**, 1–4.

34 H. L. Parker, J. Sherwood, A. J. Hunt and J. H. Clark, *ACS Sustain. Chem. Eng.*, 2014, **2**, 1739–1742.

35 S. Ikeda, T. Takagi and K. Ito, *Bull. Chem. Soc. Jpn.*, 1987, **60**, 2517–2522.

36 J. Fischer, T. Lehmann and E. Heitz, *J. Appl. Electrochem.*, 1981, **11**, 743–750.

37 L. Sun, G. K. Ramesha, P. V. Kamat and J. F. Brennecke, *Langmuir*, 2014, **30**, 6302–6308.

38 Y. Yang, H. Gao, J. Feng, S. Zeng, L. Liu, L. Liu, B. Ren, T. Li, S. Zhang and X. Zhang, *ChemSusChem*, 2020, **13**, 4900-4905.

39 P. R. Roberge, *Corrosion Engineering*, McGraw-Hill Education, 2008, pp. 62−66.

40 V. V. Pavlishchuk and A. W. Addison, *Inorganica Chim. Acta*, 2000, **298**, 97–102.

41 S. Subramanian, K. R. Athira, M. Anbu Kulandainathan, S. Senthil Kumar and R. C. Barik, *J. CO_2 Util.*, 2020, **36**, 105–115.

Evaluating the Catalytic Effect of the Native Oxides of Titanium for the Electrochemical Reduction of Oxalic Acid

Published as: Evaluating the native oxide of titanium as an electrocatalyst for oxalic acid reduction, *Chem. Commun.*, 2024, **60**, 6003-6006.

Acknowledgements and Declaration

Halilu Sale performed all the experimental work for this chapter, except for some of the electrode characterisations where HS in collaboration with Zeliha Ertekin performed the electrochemical impedance spectroscopy (EIS), X-ray diffraction pattern (XRD), and X-ray photoelectron spectroscopy (XPS). Paula L. Lalaguna performed the atomic force microscopy (AFM) and ellipsometry. Mark Symes conceived the idea, assisted with data analysis, and supervised the project. The authors co-wrote the manuscript.

4.1 Introduction

Titanium (Ti) is a low-cost, stable, biocompatible material widely used in mechanical engineering, medicine, and electrochemical analysis. In addition, titanium possesses several distinct characteristics compared to conventional electrode materials[1]. It has a higher susceptibility to oxidation, leading to the spontaneous formation of a thin layer of titanium oxides (Ti_xO_y) consisting of Ti(II), Ti(III), and Ti(IV) species on the initial layers at the interface with the atmosphere or aqueous solutions[2]. The layer of titanium is partially amorphous and possesses self-healing properties. In the event of damage to the oxide coating, such as through scratching, a comparable layer forms on the newly exposed titanium surface in less than 1 second.[3] The presence of adherent coating of Ti_xO_y provides chemical inertness to the titanium surfaces, providing some level of protection. This feature enables electrochemical processes to be conducted even in harsh environments without causing degradation or deterioration to the electrode surface.[4–6]

Significant advancements in the field of electrochemistry have demonstrated the valuable electrochemical and electrocatalytic properties of titanium electrodes.[7] Additionally, Ti_xO_y films have garnered attention as an electrocatalyst, particularly in the realm of organic synthesis.[8,9]

The rising interest in using titanium sub-oxide (TixOy) as an electrode or a support material for electrochemical applications is due to its unique physical and chemical properties, exceptional metal support interaction for noble metals of group VIII, such as Pd, Rh, Pt, and Ir, excellent corrosion stability in both alkaline and acidic environments, low cost, and toxicity.[10–12] Electrochemical methods prove useful in breaking chemical bonds within organic molecules while producing organic materials. Examples include maleic acid, nitrobenzene, and nitroanilines.[13,14]

To describe the reaction occurring during the electrochemical reduction of oxalic acid on titanium electrode, Amin et al[15], proposed a hypothesis stating that glyoxylic acid is the first reduced form of oxalic acid. Depending on the reaction's selectivity and duration, the reaction could go on to produce glycolic acid or other C_2 chemicals in a sequence of concerted two-proton, two-electron transfers (Fig 4.1)[16].

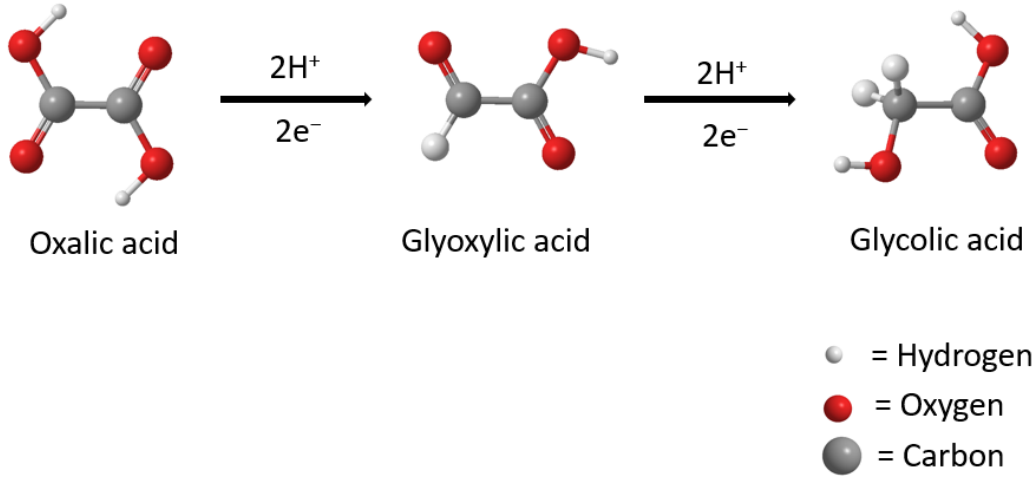

Figure 4.1: A pathway showing the reduction of oxalic acid to glyoxylic and glycolic acid, as described by Halilu *et al*.[17]

Glyoxylic and glycolic acids, which are high-add-value chemicals with an attractive potential market, are of particular interest in oxalic acid reduction products.[18] It is interesting to mention that the global markets for glyoxylic acid and glycolic acid are expected to reach a combined value of over one billion US dollars by 2025.[19] These potentials indicate that both glyoxylic acid and glycolic acid command a higher market value compared to the average for other petrochemical intermediates. The higher value of glyoxylic and glycolic acid can be attributed to several factors, including their specific chemical properties, versatile applications, and demand in specialised industries.[19]

Glyoxylic acid is extensively used as an intermediary component in the production of pharmaceuticals, dyes, plastics, agrochemicals, personal care products, cosmetics, and many other important chemicals.[20,21] Glycolic acid is used in several industries as an α-hydroxy acid. Firstly, it is utilised in the textile industry as a whitening and tanning agent. Secondly, it serves as a flavouring agent in the food industry. Thirdly, it is employed as a monomer in the polymers industry for the synthesis of polyglycolic acid (PGA), a biodegradable and thermoplastic polymer, as well as poly(lactic-co-glycolic) acid (PLGA), a biodegradable and biocompatible copolymer used in the production of therapeutic devices.[19,22]

Currently, the electrocatalytic reduction of oxalic acid is one of the major commercially employed electro-organic processes for glyoxylic acid synthesis because the process can be carried out at more moderate conditions (room temperature and pressure) than other synthetic methods that require high temperature and pressure. It also allows for precise control over reaction conditions and product selectivity compared to other methods of CO_2

reduction like chemical and thermal conversion, where high temperatures and pressures are mostly required, leading to increased energy consumption.[23]

Similarly, the production of glycolic acid involves a complex multistep process, including raw material preparation, chemical reactions, optimisation, separation, and purification. It is industrially produced either by the hydrative carbonylation of formaldehyde or by chlorination of acetic acid followed by hydrolysis of the resulting chloroacetic acid in the presence of sodium hydroxide.[19] It is worth noting that many cathode materials, such as lead, graphite, and various metal electrodes, were investigated in oxalic acid reduction.[24] However, these methods and cathode materials still have some drawbacks; the major limitation is that the cathode material (Pb), easily gets deactivated, while the other cathode materials investigated suffer from low efficiency and poor selectivity towards the target products[23,25], these problems result in the generation of low-yield and unwanted products which renders the process inefficient.[19]

Alternative methods to produce glyoxylic and glycolic acids are continually being researched to improve efficiency, sustainability, and environmental friendliness. These include enzymatic processes, microbial fermentation, electrochemical methods and other innovative approaches[26]. To this end, various forms of titanium-based electrodes like modified titanium oxides and titanium nanotube arrays have been investigated and suggested as alternative catalysts due to their exceptional stability in an acid environment.[27,28] However, the prepared titanium oxide catalysts also exhibit severe problems such as insufficient conductivity due to the thickness of the film, unfavourable electrode-solvent interactions and low catalytic activities when the film degrades into particles (film-particle transition).[29] Considering the limitations of the prepared titanium oxide catalysts highlighted above, we tend to explore a viable option that could achieve the synergistic effect of good electrical conductivity from the titanium metal and catalytic effect from the corresponding oxides. Herein, we examined the catalytic effect of the native oxides of titanium in oxalic acid reduction within a range of applied potentials (−0.5 to −0.7 V vs RHE). The outcome of our finding at an optimal potential is presented in Table 4.1 together with some previous results from the literature on oxalic acid reduction on different forms of titanium electrodes.

Table 4.1: Summary of some recent studies on the electrochemical reduction of oxalic acid to glyoxylic and glycolic acid on different titanium electrodes at room temperature for 2 hours

Entry	Applied potential (V *vs* RHE)	Oxalic acid Conc. (M)	Working electrodes	Oxalic acid conversion (%)	Faraday efficiency (%)		Yield (%)		Average current density (mA/cm^2)	Ref.
					Glyoxylic	Glycolic	Glyoxylic	Glycolic		
1	−0.8	0.1	TNT	-	45	38	-	-	−7.0	[25]
2	−0.9	0.1	TNF	-	17	38	-	-	−9.0	[25]
3	−1.0	0.1	TNP	-	20	22	-	-	−6.0	[25]
4	−0.9	0.03	TiNT-60	6.8	51.1	43.8	4.7	2.1	−1.4	[19]
5	−1.0	0.03	TiNT-HS	25.5	25.0	61.0	11.3	14.2	−2.6	[19]
6	−0.8	0.03	TiO_2/Ti-M	23.0	-	50	-	-	-	[30]
7	−0.6	0.16	PTS-500	-	49	51	16	8	-	[31]
8	−0.8	0.03	TiO_2-NTF	-	26	15	-	-	−4.0	[32]
9	−1.0	0.03	g-C_3N_4/TiO_2-NTF	-	12	76	-	-	−4.5	[32]
10	−0.6	0.03	Ti/ native oxides	38.4	43.0	32.8	27.3	10.5	−5.1	This work

Key: TiO_2/Ti-M = Titanium oxide-titanium mesh electrode, TNT = TiO_2 nanotubes, TNF = TiO_2 nano-flakes structures, TNP = TiO_2 nano-powders, TiNT-60 = Titanium nanotubes, prepared by anodic oxidation with ageing time of 60 minutes, TiNT-HS = Titanium nanotubes hydrothermally synthesised, PTS-500 = Porous titanium oxide sphere calcined at 500 °C, TiO_2-NTF = Titanium oxide nanotubes ordered thin films, g-C_3N_4/TiO_2-NTF = Titanium oxide nanotubes ordered in thin films mixed with graphitic carbon nitride.

4.2 Experimental

4.2.1 Materials and Methods

The following materials were obtained from their respective suppliers and used without further purification: oxalic acid (anhydrous for synthesis, Sigma-Aldrich, 99.0%), sulfuric acid (H_2SO_4, Fisher Chemical, 95.0%), acetone (technical grade, VWR chemicals, ≥ 99.0%), sodium sulfate (Na_2SO_4, Sigma-Aldrich, 99.0%), argon (Ar, supplied by BOC, 99.99%), titanium foil (Thermo-Scientific, 0.25mm thick, 99.5% metal basis), platinum foil (Pt, Alfa Aesar, 0.25 mm, 99.99% metals basis), Nafion membrane (Nafion-117, manufactured by Fuel Cell Store).

The titanium foil obtained from Thermo-Scientific was mechanically cut into 1 × 1 cm (2 cm^2) and 2 × 1 cm (4.0 cm^2) for cyclic voltammetry and bulk electrolysis respectively, thereafter the electrodes were ultrasonically cleaned in deionised water with a resistivity of 15 MΩ-cm for 5 minutes each. The prepared titanium electrodes were kept under air to dry and served as cathode materials while platinum foil of the same surface area with the cathode was used as anode. All electrolyte solutions were prepared with ultrapure deionised water (15 MΩ-cm resistivity). All other materials were obtained as stated in the text.

Ellipsometry and Atomic Force Microscopy were performed to evaluate the thickness and roughness of the native oxides on the electrode surface, respectively. Ellipsometry was performed using a variable-angle ellipsometer (M-2000XI Ellipsometer, J. A. Woollam) to measure the amplitude and phase changes in the wavelength range 210-1690 nm at different angles of incidence, while atomic force microscopy (AFM) was done using a Dimension Icon Atomic Force Microscope System with ScanAsyst using a silicon tip (ScanAsyst-Air-HPI) and peak force tapping. A scan size of 10 mm, a scan rate of 0.3 Hz and 512 samples/lines were used for all the measurements.

4.3 Electrochemical Methods and Products Analysis

4.3.1 Cyclic Voltammetry (CV)

Cyclic voltammetry measurements were conducted using a Gamry potentiostat/galvanostat (Gamry Instruments, interface 1010E). The electrochemical measurement was performed in a conventional three-electrode glass cell. The working electrode was titanium foil with a surface area of 2 cm^2, while the counter electrode was platinum foil of the same dimension as the working electrodes. A saturated calomel electrode (SCE) served as the reference

electrode. All potentials were measured relative to SCE. The experiments were conducted at 25 °C.

4.3.2 Bulk Electrolysis

The experiment was conducted by chronoamperometric techniques, 40 mL of 0.03 M oxalic acid in 0.2 M Na_2SO_4 solution (pH = 2.2) was applied in the cathodic compartment. The solution's pH was measured with a pH meter (Hanna Instruments, HI 9025). At the anodic section, a solution of 0.2 M Na_2SO_4 was employed, and the pH of the anodic compartment was adjusted by adding 1 M H_2SO_4 dropwise until it reached the same pH as the cathodic compartment. The measurement was conducted using Gamry potentiostat/galvanostat (Gamry Instruments, interface 1010E) for two hours at each applied potential, within the range of −0.5 to −0.7 V *vs* RHE at a temperature of 25 °C. For easy comparison with some previously reported outcomes in oxalic acid reduction, all the potentials measured against SCE in bulk electrolysis were converted to RHE using the relation $E_{RHE} = E_{SCE} + 0.244\ V + 0.0591 \times pH$ while the potential measured against Ag/AgCl by other researchers in the literature were also converted to RHE using the relation $E_{RHE} = E_{Ag/AgCl} + 0.1976\ V + 0.0591 \times pH$.[33] The bulk electrolysis setup is presented in Figure 4.2.

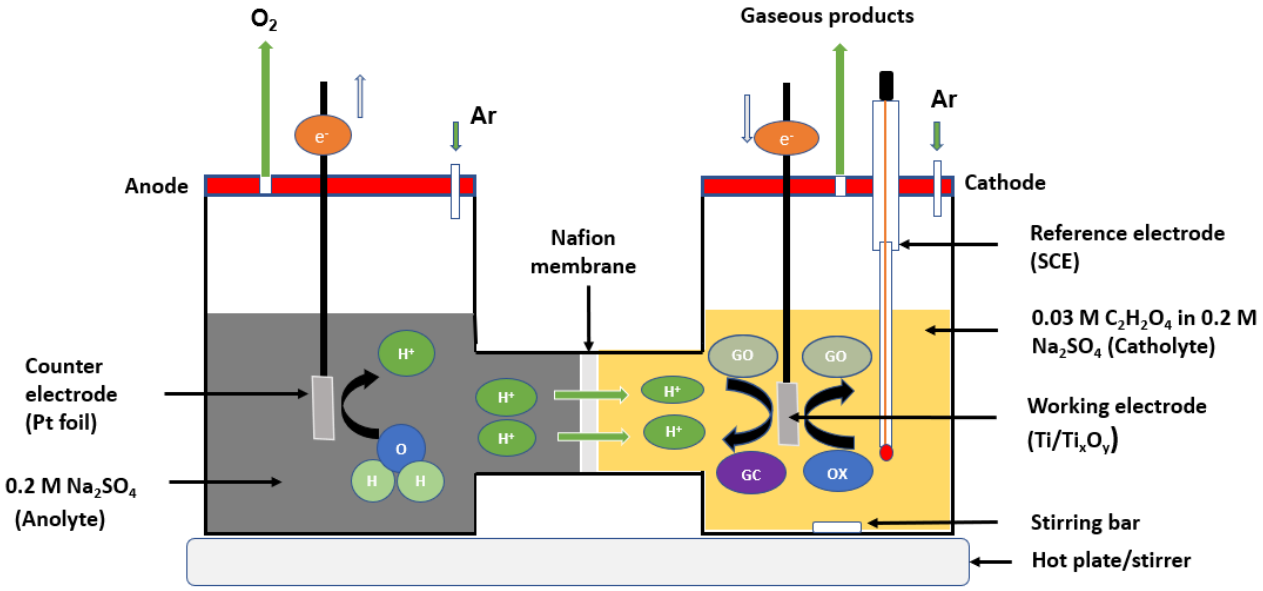

Figure 4.2: H-cell set up for the electrochemical reduction of oxalic acid (OX) to glyoxylic acid (GO) and glycolic acid (GC). The right-hand compartment of the cell is where the working electrode (Ti foil with a surface area of 4 cm^2) and a reference electrode (SCE) were placed, while the left-hand side contains the anolyte where the counter electrode (platinum foil) was placed. The two compartments are separated by a Nafion membrane. The experiment was conducted at a temperature of 25 °C for 2 hours at each applied potential.

4.3.2.1 High-Performance Liquid Chromatography-Mass Spectrometry (HPLC-MS)

The liquid products were analysed by high-performance liquid chromatography-mass spectrometer (Agilent 6125B Single Quad LC-MS), using an Aminex HPX-87H, 300 mm × 7.8 mm column. The mobile phase used was 0.1% formic acid in acetonitrile (HPLC grade) and 0.1% formic acid in water in a ratio of 30:70, respectively. The HPLC machine was set at a flow rate of 0.6 mL/min, at a temperature of 60 °C, and with a detector wavelength of 210 – 230 nm.

4.3.3 Electrochemical Impedance Spectroscopy (EIS)

Electrochemical impedance spectroscopy (EIS) was performed to study possible changes in the electrode's electrical properties. The measurements were conducted using a Gamry potentiostat/galvanostat (Gamry Instruments, interface 1010E) with three electrode settings ranging from 1×105 to 1×10^{-1} Hz. A constant polarisation potential (−0.6 V) was applied during the EIS measurements. The equivalent circuit's model parameters were determined using Gamry Echem Analyst software.

4.4 Results and Discussion

4.4.1 Cyclic Voltammetry Studies

Figure 4.3 shows the cyclic voltammograms of the oxalic acid reduction on the titanium foil electrode, which are used to determine the reduction potential of oxalic acid on the titanium electrode. The measurements were taken both in the absence (black line) and presence of oxalic acid (red line) under Ar-saturated electrolyte between the potential of 0 to −1.5 V (*vs* SCE) at a sweep rate of 50 mV/s. The cyclic voltammograms of the electrode revealed a steep increase in the current density upon adding oxalic acid to the electrolyte. The result indicated that the reductive currents originated from oxalic acid reduction when the cycle went beyond −0.8 V *(vs* SCE).

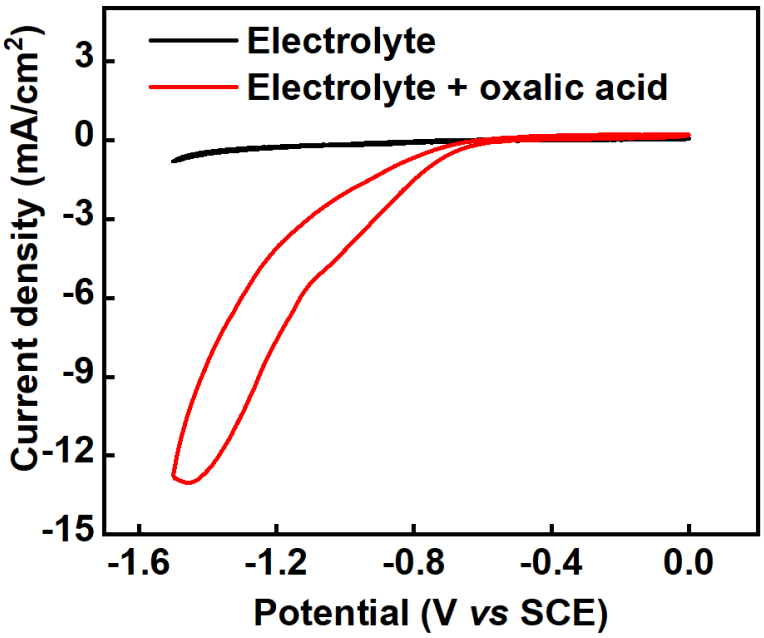

Figure 4.3: Cyclic voltammetry of titanium foil electrode having a surface area of 2 cm^2 in (a) 0.2 M Na_2SO_4 (black line) and (b) 0.03 M oxalic acid in 0.2 M Na_2SO_4 (red line). Platinum foil is the counter electrode, while SCE is the reference electrode. The measurements were taken at a temperature of 25 °C and a scan rate of 50 mV s^{-1}.

4.4.2 Chronoamperometric Studies

The electrochemical reduction of oxalic acid was conducted in a H-cell set-up having three electrode configurations as depicted in Figure 4.2. Chronoamperometric experiments were performed for 2 hours at each applied potential. At the end of every experiment, the liquid products from the cathodic compartment were sampled and analysed by Agilent high-performance liquid chromatography (HPLC). An example of the HPLC signal showing the chromatograms for the electrochemical reduction of oxalic acid to glyoxylic acid and glycolic acid is shown in Figure 4.4.

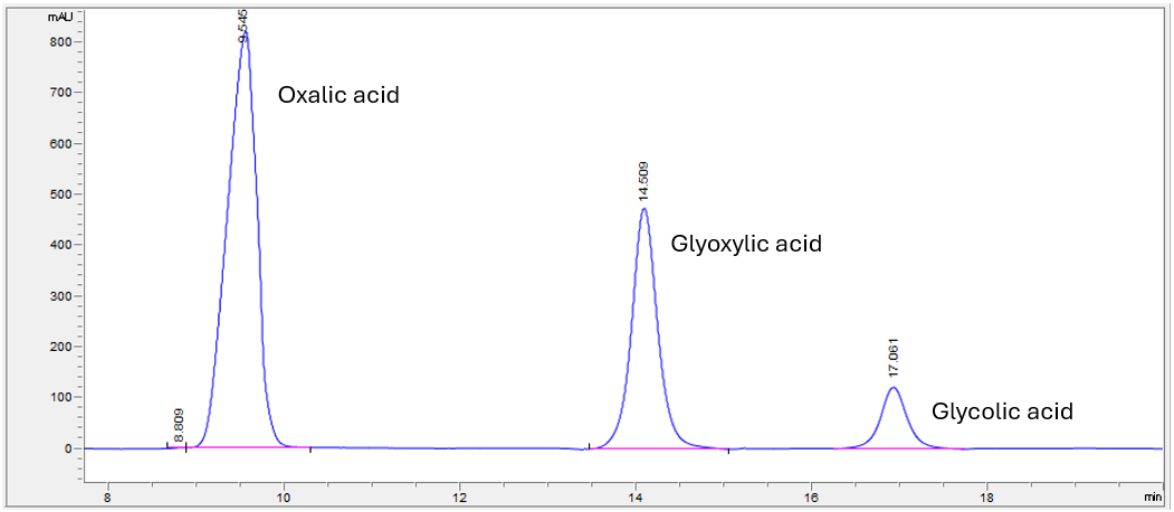

Figure 4.4: HPLC signal showing the chromatograms and retention time for electrochemical reduction of oxalic acid to glyoxylic acid and glycolic acid at an applied potential of −0.6 V vs SCE at 25 °C.

Based on the molar concentration of the oxalic acid used as the starting material for the reduction process, Faraday efficiency was evaluated using Equation 1.9 in section 1.3.4 Kinetics of CO2 Electroreduction3.4.2 Faraday Efficiency and Yield of Chapter 1, while the following equations (4.1 – 4.3)[19] are used in evaluating the performance of the titanium electrode and its native oxides (Ti/Ti_xO_y) in the cell.

The degree of oxalic acid conversion in the experiment was computed thus:

$$Oxalic\ Acid\ conversion\ (\%) = \frac{[OX]_i - [OX]_t}{[OX]_i} \times 100 \qquad (Equation\ 4.1)$$

Where $[OX]_i$ = the initial concentration of oxalic acid and $[OX]_t$ = the concentration of oxalic acid at the end of the electrolysis.

The yield (Y) of the respective products is calculated as follows:

$$Yield\ to\ m_{[GO]}\ (\%) = \frac{[GO]_t}{[OX]_i} \times 100 \qquad (Equation\ 4.2)$$

$$Yield\ to\ m_{[GC]}\ (\%) = \frac{[GC]_t}{[OX]_i} \times 100 \qquad (Equation\ 4.3)$$

Where $[GO]_t$ = the concentration of $m_{[GO]}$ after 2 h of reaction time,

$[GC]_t$ = the concentration of $m_{[GC]}$ after 2 h of reaction time,

$[OX]$, $[GO]$ and $[GC]$ are the molar concentrations of oxalic, glyoxylic and glycolic acids respectively.

After obtaining the data for the chronoamperometric experiments and HPLC analysis of the liquid products, the resulting current densities, Faradaic efficiencies, oxalic acid conversion and percentage yield of the products were computed using Equations 4.1 – 4.3, the results are presented in Table 4.2.

Table 4.2: Average Faraday efficiency, oxalic acid conversion, percentage yields and current densities for electrochemical reduction of oxalic acid on titanium electrodes for 2 hours at 25 °C.

Potentials (V vs RHE)	Faraday efficiency (%)		Oxalic Acid Conversion (%)	Yield (%)		Current Density (mA/cm^2)
	Glyoxylic	Glycolic		Glyoxylic	Glycolic	
−0.5	47.0 ± 2.3	38.0 ± 2.8	31.0 ± 2.2	20.5 ± 1.5	8.3 ± 0.9	−3.5
−0.6	43.0 ± 2.6	32.8 ± 2.2	38.4 ± 1.9	27.3 ± 1.9	10.5 ± 0.6	−5.1
−0.7	23.6 ± 2.4	19.2 ± 2.7	34.2 ± 1.7	22.3 ± 1.6	9.1 ± 0.8	−7.6

Analysis of the experimental data (chronoamperometric) revealed that the current densities generally increase with increasing potential, as illustrated in Figure 4.5. However, the optimal performance of the titanium electrode (Ti/Ti_xO_y) in terms of oxalic acid conversion and product yield was recorded at an applied potential of −0.6 vs RHE. This suggests that −0.6 V is the optimal potential for efficiently reducing oxalic acid.

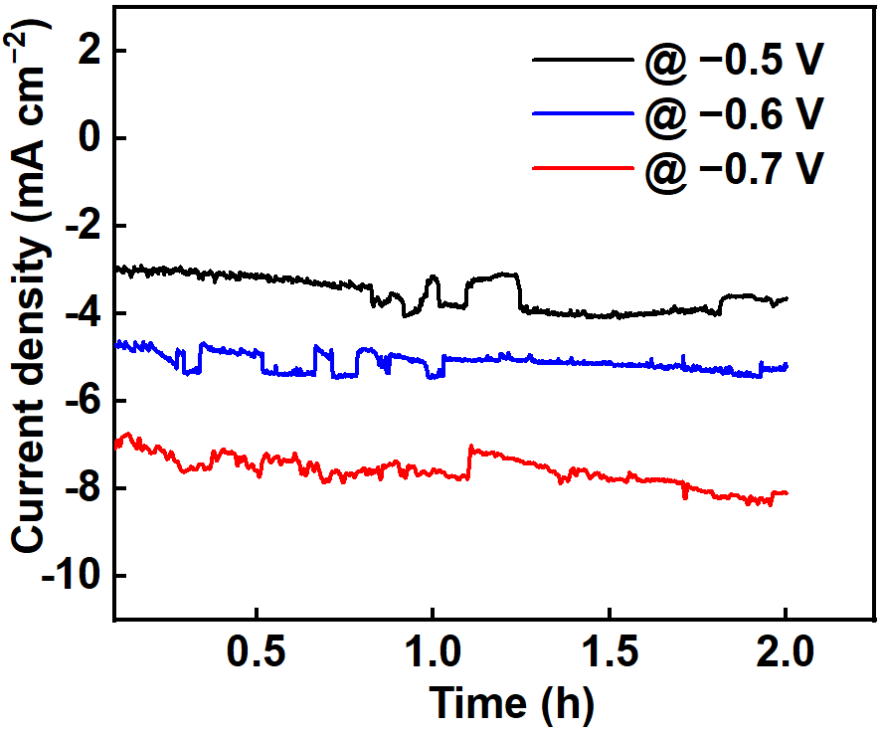

Figure 4.5: Current densities of titanium electrode during bulk electrolysis in 0.03 M oxalic acid at three different applied potentials (−0.5 V, −0.6 V and −0.7 V vs RHE) for two 2 hours at 25 °C.

On the other hand, the Faradaic efficiency tends to drop with increasing potential, as depicted in Figure 4.6. It is essential to mention that the hydrogen evolution reaction usually competes with the oxalic acid reduction reactions; this partly accounts for why the Faradaic efficiencies are generally less than 100%.[34] Hence, the declining efficiency could be largely attributed to the hydrogen evolution reaction or conversion of the product to by-products.

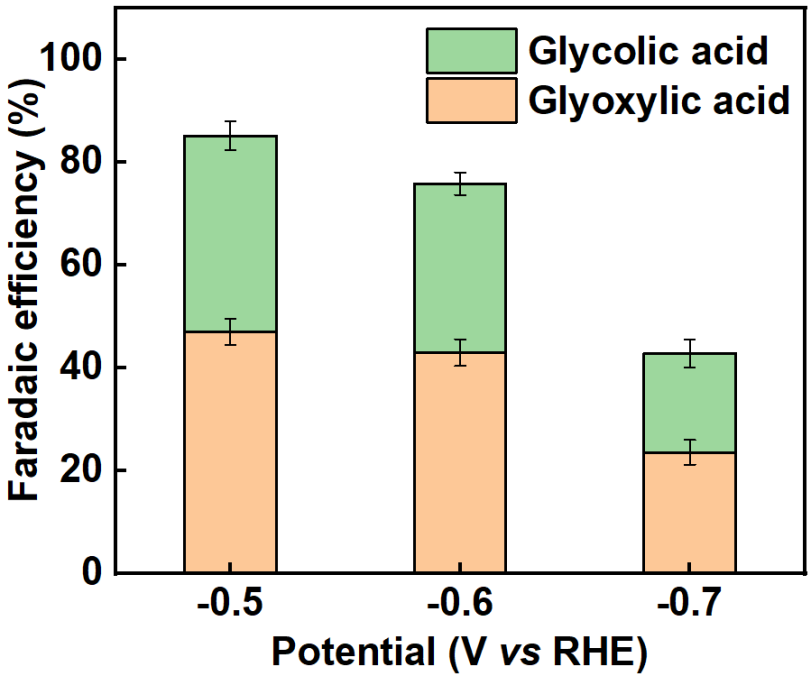

Figure 4.6: Showing the average Faradaic efficiency of glyoxylic and glycolic acids during bulk electrolysis of 0.03 M oxalic acid for two hours, using titanium foil as a working electrode and platinum foil as a counter electrode in an H-cell at 25 °C.

Herein, the catalytic effect of native oxides of titanium in oxalic acid reduction has been established. The most efficient performance was recorded at an applied potential of −0.6 V versus RHE; the optimal result is presented in Table 4.1 (entry 10). From the result, it could be noticed that the conversion rate of oxalic acid was 38.4% ± 1.85 and a cumulative Faraday efficiency of 75.8% was achieved, corresponding to 43.0% ± 2.58 for glyoxylic acid and 32.8% ± 2.16 for glycolic acid production, respectively. The conversion rate of 38.4% achieved at a potential of −0.6 *vs* RHE in this work is slightly higher than the highest reported value of 25.5% (Table 4.1, entry 5) previously reported by Abramo *et al.*[19] on a modified titanium electrode at a comparatively higher applied current (−1.0 *vs* RHE). Similarly, the cumulative product yield of 37.8% achieved in this work is the highest reported value. Evaluating the systems' performances in terms of energy requirement and conversion efficiency, the catalytic effect of the native oxide is quite remarkable because the highest conversion of oxalic acid was achieved at a lower applied potential.

4.5 Characterisation of the Titanium Electrode

4.5.1 Ellipsometry

Ellipsometry was performed to evaluate the thickness of the native oxides.[35] The Ellipsometry measurement was achieved from various angles of incidence; 45°, 50°, 55°, 60°, 65°and 70°. This was done at nine (9) different positions on the sample, before and after electrolysis. The ellipsometry data were fitted using a Lorentz model to extract information on the Ti substrate and a B-Spline model for the native oxide, from which the thickness was extracted. The B-Spline model measures the thickness of the surface oxides independent of the thickness of the bulk material. The Ellipsometry technique provides an independent measurement of the thickness of an adsorbed film. It relies on the principle that the polarisation state of light changes upon reflection from a surface. When elliptically polarised light reflects off a bare surface, both the amplitude ratio and the phase difference of the light's components are altered. The distinct phase difference between the oxides and the bulk material enables the measurement of the thickness or properties of the surface layer independently.[36,37]

A fitting model for one of the positions on the sample compared to experimental Psi and Delta at different angles before and after electrolysis is shown in Figure 4.7.

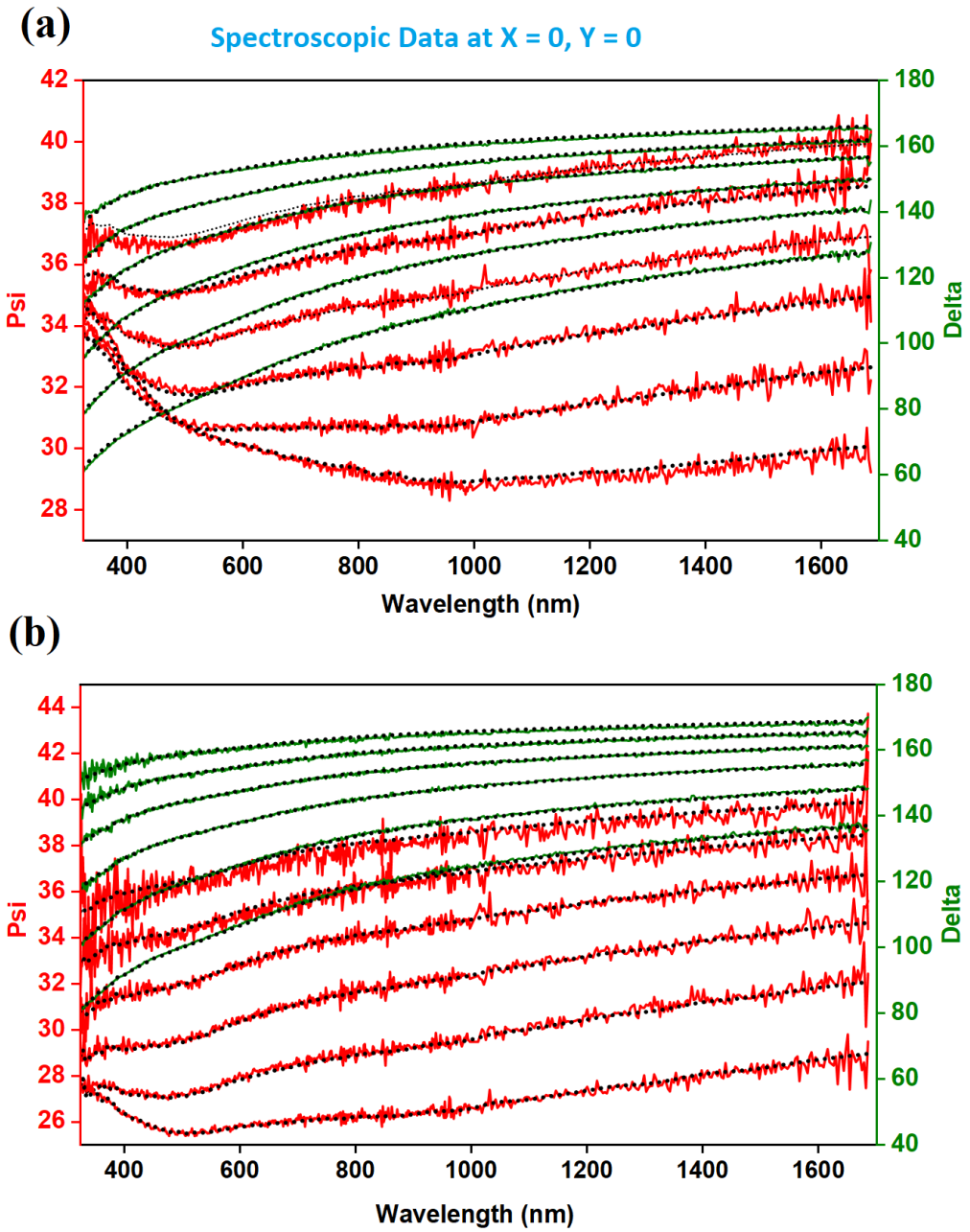

Figure 4.7: The ellipsometry fitting model (black) and experimentally measured Ψ (Psi) and Δ (Delta) (red and green, respectively) at different angles for the titanium electrode (a) before and (b) after electrolysis.

The ellipsometry outcomes in Table 4.3 suggested a decrease in the thickness of the native oxide after the electrolysis. The reduction in the thickness of the native oxides of titanium after the electrolysis could be attributed to the likely etching of the oxides by the acid,[38] or parts of the oxides nearest to the metal have been reduced during electrolysis.

Table 4.3: The average thickness of native oxides obtained from the ellipsometry data of all the angles analysed.

Electrode	Thickness of the native oxides (nm)
Before electrolysis	48.417± 0.4477
After electrolysis	17.793 ± 1.4775

4.5.2 Atomic Force Microscopy (AFM)

Atomic force microscopy was performed to assess the roughness of the electrode surface before and after the electrolysis. After obtaining data from the atomic force microscopic analysis of the electrode. The surface roughness was obtained using Gwyddion software. Samples of the AMF 3D-topography of the surface of the titanium electrode before and after the electrolysis are presented in Figure 4.8(a and b).

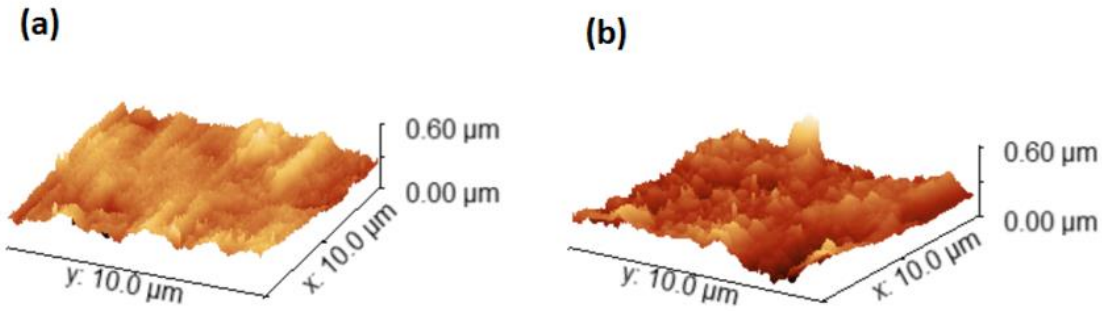

Figure 4.8: AFM analysis of titanium electrode surfaces (a) before and (b) after electrolysis

The surface layer of the electrode before the electrolysis is assumed to be composed of Ti and TiO_2 as the primary oxide. However, the TiO_2 may undergo some changes due to either reduction or further oxidation on the surface. The roughness value of the surface of the electrode before and after electrolysis is presented in Table 4.4. As expected, the rough morphology of the surface increases after the electrolysis due to the mass transfer and diffusion process on the surface of the electrode.[38,39]

Table 4.4: Atomic force microscopy data showing the roughness value of the electrode surface before and after electrolysis.

Electrode	Average height of the peak, S_h (nm)	Average roughness, R_a (nm)	Root mean square roughness, R_q (nm)
Before electrolysis	143	26.2	35.2
After electrolysis	317	38.3	49.7

4.5.3 Electrochemically Active Surface Area (ECSA)

The ECSA was determined through the cyclic voltammetry technique, which is one of the most effective and commonly used methods in evaluating the activity of electrocatalysts.[40,41] First, a non-Faradaic potential range was identified from the cyclic voltammograms of titanium electrodes, as depicted in Figure 4.3. Under the region (−0.05 to −0.40 V), which is depicted in Figure 4.9(a), a series of CV scans were performed at different scan rates (10, 50, 100, 200, 300, 400, 600, 800 1000 mV s^{-1}). The electrode's electrochemically active surface area (ECSA) was calculated using Equation 4.4.

$$ECSA = \frac{C_{DL}}{C_S} \qquad (Equation\ 4.4)$$

Where, C_{DL} = Double layer capacitance, C_S = Specific capacitance

To measure the electrode's capacitance, it is assumed that all the measured current in the non-Faradaic region is due to double-layer charging of Ti/Ti_xO_y.[41] Based on this assumption, the charging current (i_c) is measured from the cyclic voltammograms of the multiple scan rates in Figure 4.12(a). The current obtained is equal to the product of the electrochemical double-layer capacitance (C_{DL}) and the scan rate (v), as shown in Equation 4.5.

$$i_c = vC_{DL} \qquad (Equation\ 4.5)$$

A plot of i_c against v gives a straight-line graph with a slope equal to C_{DL} (Figure 4.9b).

Thus, the electrochemical double-layer capacitance of the electrode, $C_{DL} = 0.18 \times 10^{-3}$ As V^{-1} (0.18 mF).

Thus, the specific capacitance (C_S) values can be calculated from the cyclic voltammograms by using Equation (4.6)[42]

$$C_S = \frac{1}{\Gamma v\,(V_2 - V_1)} \int_{V_1}^{V_2} I(V)dV \qquad (Equation\ 4.6)$$

Where $\boldsymbol{\Gamma}$ is the area of the working electrode in cm^2, v is the scan rate in V s^{-1} and ($V_2 - V_1$) is the potential window expressed in V. The specific capacitance at a scan rate of 1 V s^{-1} was

found to be 1.21 × 10^{-4} As V^{-1} cm^{-2}. By substituting the values of capacitance and the specific capacitance into equation 5, an ECSA value of 1.488 cm^{-2} was obtained.

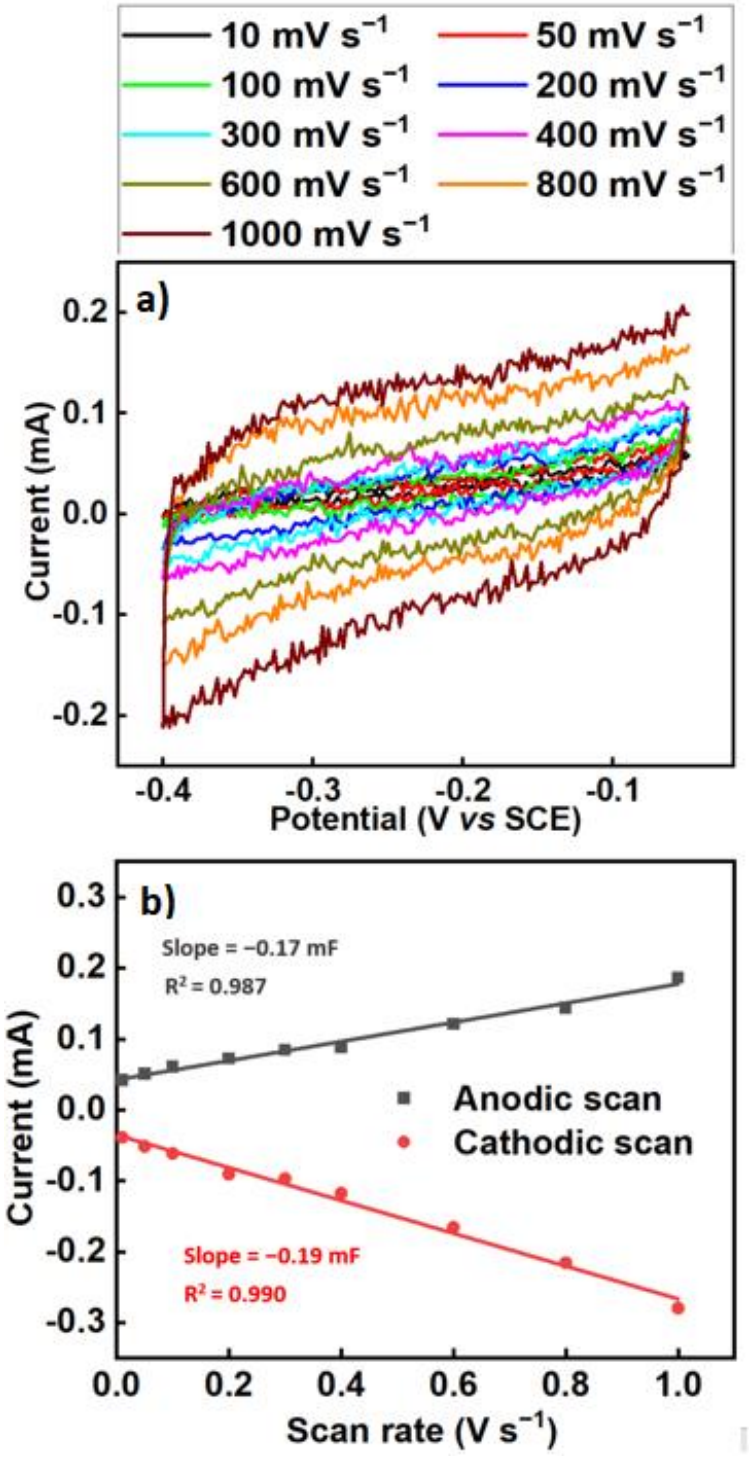

Figure 4.9: Double-layer capacitance measurements for determining the electrochemically active surface area of a titanium electrode (Ti/Ti_xO_y) in 0.3 mM oxalic acid and 0.2 M tetraethyl ammonium chloride as supporting electrolyte. (a) Cyclic voltammograms of the non-Faradaic region at different scan rates using platinum foil as a counter electrode and SCE as a reference electrode. (b) The anodic (black cubes) and cathodic (red circles) charging currents measured at −0.23 V vs SCE were plotted

against the scan rate. The determined double-layer capacitance of the electrode is taken as the average of the absolute value of the slope of the linear fits of the data.

4.5.4 Electrochemical impedance spectroscopy (EIS)

The electrochemical impedance spectra of the native oxide films were used to understand interfacial behaviour and to determine some electrochemical parameters on the surface of the electrodes.[7] The typical Nyquist plot was employed to understand the electrochemical stability information of the native oxides on the titanium electrodes before and after the electrolysis. The impedance response of titanium electrodes was evaluated at optimal potential (−0.6 V). The Nyquist plots resulting from the electrochemical impedance spectroscopy (EIS) measurements were then analysed using an equivalent circuit model, as illustrated in Figure 4.10. The electrical equivalent circuit model that describes the electrode process was determined by fitting the experimental impedance data using Gamry Echem Analyst software. Various equivalent circuit models were examined to describe the electrode processes (Ti/Ti_xO_y /electrolyte junction) and the simplest circuit with the smallest chi-squared (χ^2) value was chosen, which was applied according to the methods developed in the literature.[7,43–45] The electrical parameters of the proposed equivalent circuits obtained after fitting results of EIS tests for the titanium electrodes are presented in Table 4.5. In the equivalent circuit model, R_s refers to the solution resistance while R_1 and R_2 represent charge transfer resistance. CPE_1 and CPE_2, represent the constant phase elements commonly used to describe nonhomogeneous surfaces.[46] Obviously, the two semicircles in the Nyquist plots (Figure 4.11) indicate two different responses of the working electrodes before and after the electrolysis, respectively. Additionally, the electrode exhibits smaller semicircles after electrolysis compared to their pre-electrolysis state. This reduction suggests better conductance of the electrodes after the electrolysis. This phenomenon could be attributed to the fact that some of the oxide layer has been removed, perhaps by in situ reduction at the applied cathodic potentials. In addition, the layer's total resistance (R_{total}), representing the sum of all resistance values, is also calculated (Table 4.5). The R_{total} value for the titanium electrode before electrolysis is 88.32 Ω, whereas it decreases to 59.21 Ω after electrolysis. This decrease shows that the electroactive area increases when the potential is applied, leading to improved electron transfer through the conductive layers. The observed reduction in R_{total} can be attributed to a potential decrease in the thickness of the titanium oxide layer after electrolysis. The alterations in film thicknesses and total resistances suggest notable changes in the composition and morphology of the electrode surfaces.

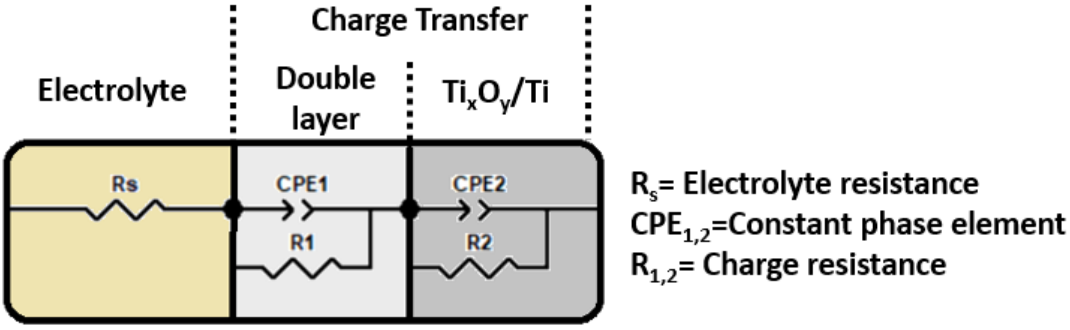

Figure 4.10: The equivalent circuit model used for modelling the EIS data of the titanium electrode.

Table 4.5: Electrical parameters of the proposed equivalent circuits obtained after fitting results of EIS tests for titanium electrodes.

Electrodes	R_s/ Ω	R_1/ Ω	CPE_1 mF	n_1	R_2/ Ω	CPE_2 mF	n_2	R_{total}	Chi-squared $\chi 2$
Before	10.52	12.9	6.05	0.60	64.9	7.51	0.86	88.32	2.22×10^{-4}
After	10.29	13.01	8.98	0.59	35.91	7.60	0.89	59.21	1.77×10^{-5}

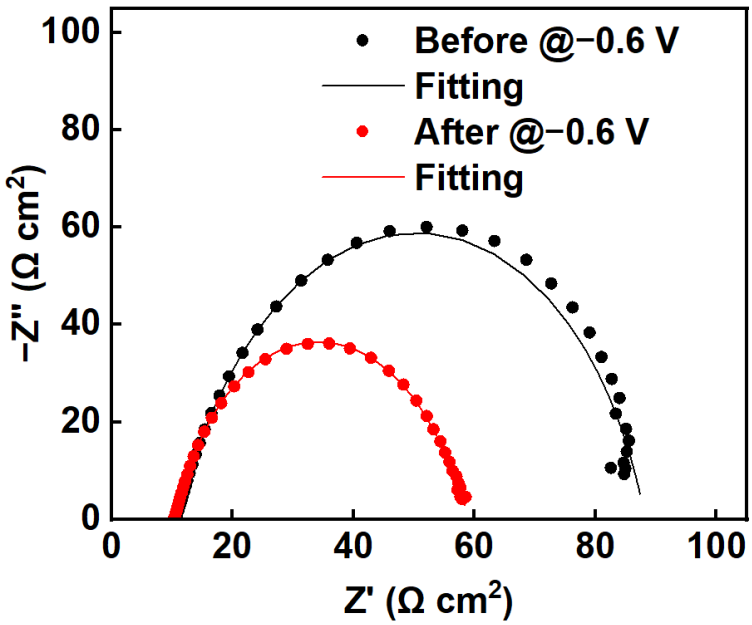

Figure 4.14: Nyquist plots obtained at −0.6 V vs RHE on titanium electrode in 0.03 M oxalic acid solution, (a) before electrolysis and (b) after electrolysis for 2 hours at 25 °C. Cycle points represent the experimental data, and continuous curves represent the model fitting.

4.6 Conclusion

In this work, we have for the first time evaluated the catalytic effect of the native oxides of titanium (Ti/Ti_xO_y) in the electrochemical reduction of oxalic acid. The performance of the electrodes in terms of percentage conversion of the oxalic acid and yield of the products revealed better performance compared to other modified titanium electrodes. We have reported the highest conversion of oxalic acid (38.4%) and cumulative product yield of 27.3% and 10.5% corresponding to glyoxylic and glycolic acid, respectively, which are attributed to the catalytic effects exerted by the native oxides in the electrochemical reaction.

To elucidate the behaviour and stability of the native oxides, different physicochemical and electrochemical analyses have been carried out on the electrodes before and after electrolysis. The electrochemically active surface area of the electrode was established as 1.488 cm^{-2}. According to the combined results, a series of relationships exist between the outcomes of these analyses. The Ellipsometry result shows a decrease in the thickness of the native oxides from 48.4 to 17.8 nm, this is partly responsible for the increase in the surface roughness of the electrodes from 35.2 to 49.7 nm, as evidenced by the Atomic Force Microscopy result. In addition, the Electrochemical Impedance Spectroscopy revealed an increase in the electrode conductivity after electrolysis.

Overall, our results show that the direct reduction of oxalic acid to glyoxylic and glycolic acid can be achieved with high yield at room temperature with the aid of native oxides of Ti on titanium electrodes (Ti/Ti_xO_y) for a better, cost-effective and more sustainable process.

4.7 References

1 F. Terzi and N. Dossi, *Anal. Bioanal. Chem.*, 2015, **407**, 7257–7261

2 S. Guo, Z. Xu, W. Hu, D. Yang, X. Wang, H. Xu, X. Xu, Z. Long and W. Yan, *Catal.*, 2022, **12**, 618.

3 A. Balasankar, S. E. Arthiya, S. Ramasundaram, P. Sumathi, S. Arokiyaraj, T. Oh, K. Aruchamy, G. Sriram and M. D. Kurkuri, *Energies,* 2022, **15**, 9495.

4 W. Ke, C. C. Stoumpos, J. L. Logsdon, M. R. Wasielewski, Y. Yan, G. Fang and M. G. Kanatzidis, *J. Am. Chem. Soc.*, 2016, **138**, 14998–15003.

5 J. E. Carrera-Crespo, J. Ghilane, H. Randriamahazaka, S. Ammar and I. González, *J. Electrochem. Soc.*, 2017, **164**, H286–H292.

6 N. P. Shetti, D. S. Nayak, S. J. Malode and R. M. Kulkarni, *J. Electrochem. Soc.*, 2017, **164**, B3036–B3042.

7 S. Popescu, C. Ungureanu, A. Albu, C. Pirvu, *Progress in Organic Coatings,* (2014), **77**, 1890–1900

8 L. Liu, X. Gu, Z. Ji, W. Zou, C. Tang, F. Gao and L. Dong, *J. Phys. Chem. C*, 2013, **117**, 18578–18587.

9 W. Xu, Y. Cheng, J. Hou and P. Kang, *ChemCatChem*, 2023, **15**, e202201687.

10 M. Molina-Torres, O. Hernández-Cristóbal and R. Mendoza-Cruz, *Front. Nanotechnol.*, 2023, **5**, 1–17.

11 S. K. S. Hossain, J. Saleem, S. U. Rahman, S. M. J. Zaidi, G. McKay and C. K. Cheng, *Catalysts*, 2019, **9**, 1–19.

12 R. Daghrir, P. Drogui and D. Robert, *Ind. Eng. Chem. Res.*, 2013, **52**, 3581–3599.

13 F. Xiao, S. Hung, J. Miao, H. Wang, H. Yang, B. Liu, 2015, *Wiley Online Libr.*, 2014, **11**, 554–567.

14 L. Hao, Q. Ren, J. Yang, L. Luo, Y. Ren, X. Guo, H. Zhou, M. Xu, X. Kong, Z. Li and M. Shao, *ACS Appl. Mater. Interfaces*, 2023, **15**, 13176–13185.

15 M. A. Farkhondehfal, U. Savino, A. Chiodoni, C. F. Pirri and A. Sacco, *Electrocatalysis*, 2023, **14**, 195–201.

16 S. Im, S. Saad and Y. Park, *Electrochem. commun.*, 2022, **135**, 107204.

17 H. Sale, Z. Ertekin, P. Laborda Lalaguna, M. Kadodwala and M. D. Symes, *Chem. Commun.*, 2024, 4–7.

18 S. Perathoner and G. Centi, *Catal. Today*, 2019, **330**, 157–170.

19 F. P. Abramo, F. De Luca, R. Passalacqua, G. Centi, G. Giorgianni, S. Perathoner and S. Abate, *J. Energy Chem.*, 2022, **68**, 669–678.

20 Y. L. Niu and L. J. Zhai, *Monatshefte fur Chemie*, 2014, **145**, 201–207.

21 Q. shan Wang, Y. chao Yuan, C. fan Li, Z. rui Zhang, C. Xia, W. guo Pan and R. tang Guo, *Small*, 2023, **19**, 2301892.

22 M. Valderrama, R. van Putten, G. J. M. Gruter, *European Polymer Journal*, 2019, 119, 445 - 468.

23 F. Zhao, F. Yan, Y. Qian, Y. Xu, C. Ma, *Journal of Electroanalytical Chemistry*, 2013, **698**, 31–38.

24 F. Goodridge, K. Lister, R. E. Plimley and K. Scott, *J. Appl. Electrochem.*, 1980, **10**, 55–60.

25 M. A. Farkhondehfal, U. Savino, A. Chiodoni, C. F. Pirri and A. Sacco, *Electrocatalysis*, 2023, **14**, 195–201.

26 X. Nie, S. Yin, W. Duan, Z. Zhao, L. Li and Z. Zhang, *Nano*, 2021, **16**, 2130002.

27 K. Lee, A. Mazare and P. Schmuki, *Chem. Rev.*, 2014, **114**, 9385–9454.

28 X. Hou, Y. Zhao and Y. Li, *Int. J. Hydrogen Energy*, 2023, **48**, 14279–14286.

29 F. Zhao, F. Yan, Y. Qian, Y. Xu and C. Ma, *J. Electroanal. Chem.*, 2013, **698**, 31–38.

30 M. Sadakiyo, S. Hata, X. Cui and M. Yamauchi, *Sci. Rep.*, 2017, **7**, 2–3.

31 R. Watanabe, M. Yamauchi, M. Sadakiyo, R. Abe and T. Takeguchi, *Energy Environ. Sci.*, 2015, **8**, 1456–1462.

32 F. de Luca, R. Passalacqua, F. P. Abramo, S. Perathoner, G. Centi and S. Abate,

Chem. Eng. Trans., 2021, **84**, 37–42.

33 L. Fan, C. Xia, P. Zhu, Y. Lu and H. Wang, *Nat. Commun.*, 2020, **11**, 1–9.

34 W. Song, Y. Zhang, H. Jin, M.-R. Kim, S. Kim and I. Kim, *J. Electrochem. Soc.*, 2017, **164**, E260–E264.

35 W. Navarrini, T. Brivio, D. Capobianco, M. V. Diamanti, M. Pedeferri, L. Magagnin and G. Resnati, *J. Coatings Technol. Res.*, 2011, **8**, 153–160.

36 I. D. Robb, 24 Adsorption, *Unilever Research, Port Sunlight, UK,* 733-750*,* accessed on 07/06/2024.

37 E. Seyrek and G. Decher, *Layer-by-Layer Assembly of Multifunctional Hybrid Materials and Nanoscale Devices*, 2012, 1–10.

38 P. Vlcak, J. Fojt, J. Drahokoupil, V. Brezina, J. Sepitka, T. Horazdovsky, J. Miksovsky, F. Cerny, M. Lebeda and M. Haubner, *Mater. Sci. Eng. C*, 2020, **115**, 111065.

39 M. Diamanti, M. Pedeferi, *Corrosion Science*, 2007, **49**, 939–948.

40 C. C. L. McCrory, S. Jung, J. C. Peters and T. F. Jaramillo, *J. Am. Chem. Soc.*, 2013, **135**, 16977–16987.

41 C. C. L. McCrory, S. Jung, I. M. Ferrer, S. M. Chatman, J. C. Peters and T. F. Jaramillo, *J. Am. Chem. Soc.*, 2015, **137**, 4347–4357.

42 K. M. Thulasi, S. T. Manikkoth, A. Paravannoor, S. Palantavida and B. K. Vijayan, 2021, **112**, 937–944.

43 I I.C.P. Margarit-Mattos, *Electrochimica Acta*, 2020, 354, 136725.

44 M. R. Jakeria, R. J. Toh, X. B. Chen and I. S. Cole, *J. Appl. Electrochem.*, 2022, **52**, 1021–1044.

45 A. Faqeeh, M. D. Symes, *Electrochimica Acta*, 2023, **444**, 142030.

46 A. C. Alves, F. Wenger, P. Ponthiaux, J. P. Celis, A. M. Pinto, L. A. Rocha and J. C. S. Fernandes, *Electrochim. Acta*, 2017, **234**, 16–27.

Optimising Ultrasound Parameters for Efficient Sonoelectrochemical CO_2 Reduction

Published as: Manuscript under review.

Acknowledgements and Declaration

Halilu Sale, Lukman Yusuf, Zeliha Ertekin, and Abhishek Rajput conceptualised and performed all the experiments for this chapter. Lukman Yusuf assisted with the sonoelectrochemical set-up. HS performed LC-MS analysis, SF performed UV-visible spectrometry, and ^{1}HNMR, GC and electrode characterisation using EIS were performed by ZE. Mark Symes assisted with data analysis and supervised the project. The authors co-wrote the manuscript.

5.1 Introduction

The rising concentration of carbon dioxide (CO_2) in the atmosphere, primarily resulting from the extensive use of fossil fuels as a major energy source, has led to global energy-related CO_2 emissions reaching 31.5 billion tons in 2020.[1] Additionally, emissions from the grey production of hydrogen and ammonia further impact our environment adversely.[2] This situation has resulted in detrimental effects such as global warming, rising sea levels, polar ice melting, and an intensified greenhouse effect.[3,4] To maintain a healthy and sustainable environment, we must reduce the concentration of CO_2 in the atmosphere. One effective approach is to convert this gas into useful and valuable chemical products. Electrochemical CO_2 reduction (ECR) is a promising method for reducing CO_2 to produce hydrocarbon fuels and other beneficial chemical products.[5,6] However, the efficiency of electrochemical CO_2 reduction is typically hindered by factors such as overpotential, limited ion mobility, and low yield. Various modifications, including the selection of suitable electrodes, the utilisation of modified electrodes, the incorporation of catalysts, and the use of stirrers, are often employed to enhance the yield and efficiency of this process. Recently, integrating ultrasonic irradiation with electrochemical cells, termed the sonoelectrochemical technique, has been reported to offer significant advantages compared to traditional electroanalytical methods. The sonoelectrochemical process offers numerous advantages, including the activation and cleaning of electrode surfaces, the elimination of gas bubbles at the electrode interface, the prevention of potential-induced damage, and the enhancement of the mass transport of ions.[7,8] These benefits are facilitated by producing acoustic cavitation bubbles during the sonoelectrochemical process, which occurs due to irradiated ultrasound.[9] The cavitation induces acoustic streaming and shockwave phenomena,[10] which helps to reduce issues associated with traditional electrochemical methods.[11] Previous studies have demonstrated the positive influence of ultrasound on various electrochemical reactions, showcasing its potential as a tool for improving reaction kinetics and selectivity.[9] Sonoelectrochemical processes can also result in the formation of reactive species and loc

alised heating, which facilitates electron transfer processes and alters reaction pathways.[9,12]

Despite these advantages, our comprehension of how ultrasonic parameters affect CO_2 reduction remains limited partly due to scanty literature in this area. Consequently, this study delves into the sonoelectrochemical reduction of CO_2 on a copper plate electrode in a CO_2-saturated 0.1 M potassium hydroxide aqueous solution under varying ultrasound-assisted conditions such as frequency (37 and 80 kHz), input power (40, 60, 80, and 100% of power setting), and bulk temperature (25 °C and 4 °C). Through systematic exploration of these

parameters, we aim to elucidate their impact on reaction efficiency, selectivity, and the underlying mechanisms. Such insights are crucial for optimising CO_2 electroreduction processes and advancing the development of sustainable energy technologies. Moreover, the findings of this study may contribute to the broader understanding of sonoelectrochemical processes and their potential applications in other catalytic reactions and energy conversion processes. It is worth mentioning that this is the first time such varying ultrasound parameters have been investigated in the sonoelectrochemical reduction of CO_2.

5.2 Experimental

5.2.1 Materials

The following materials were obtained from their respective suppliers and used without further purification: Copper foil (0.5 mm thick, 99.9985%, Thermo Scientific), potassium hydroxide (Fluka), and CO_2 (99.8%, Industrial Grade, BOC Limited), D_2O (99.9% D, Goss Scientific), dimethyl sulfoxide-D6 (99.9% D, Cambridge Isotope Laboratories, Inc), phenol (≥ 99.0%, Sigma Aldrich), HPLC-grade ultra-pure water with a conductivity of 18 MΩ-cm (Sigma-Aldrich), and HPLC-grade acetonitrile (≥99.9%, Sigma-Aldrich), potassium iodide (99%, Alfa Aesar), ammonium molybdate (para) tetrahydrate (99%, Thermo Scientific), and hydrogen peroxide (30% w/w, Sigma Aldrich) were utilised without any further purification steps. All solutions were prepared using ultrapure water (resistivity = 15 MΩ-cm).

5.2.1 Electrochemical Set-up for CO_2 Reduction

Electrochemical measurements were conducted using a Gamry potentiostat/galvanostat (Gamry Instruments, interface 1010E). The experiments were performed in a gas-tight, custom-made round three-electrode glass cell. The copper foil was mechanically cut into dimensions of 1.0 x 2.5 cm (5 cm^2), with a portion of 1.0 x 1.5 cm (3.0 cm^2) immersed in the electrolyte solution and utilised as the working electrode. A graphite rod or platinum wire was used as the counter electrode, while a saturated calomel electrode (SCE) functioned as the reference electrode. The electrodes were rinsed with ultrapure water before being placed into the sonoelectrochemical cell. A 0.1 M potassium hydroxide solution served as the electrolyte, and it underwent a 15-minute CO_2 purging process before the electrochemical experiments to ensure CO_2 saturation within the cell. The cell was placed at the center of the ultrasonic bath (Elmasonic P, Turbex) and filled with 400 ml of water, as illustrated in Figure 5.1. The experiments were conducted at room temperature (~ 25°C) and 4°C. The cell temperature was regulated by adding ice while continuously monitoring it with a

thermocouple connected to a data logger (USB TC-08, Pico Technology). The ultrasonic bath can operate independently at a frequency of 37 kHz and 80 kHz. To optimise performance, four electrical input power levels (40%, 60%, 80%, and 100%) were investigated in this study.

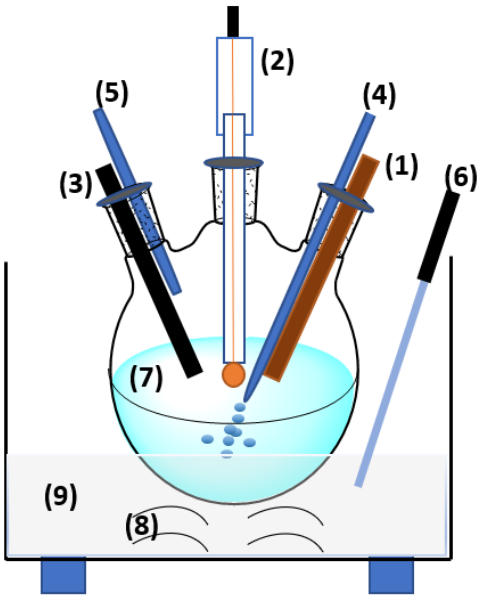

Figure 5.1: Sonoelectrochemistry set-up for electrochemical CO_2 reduction

5.3 Electrochemical Measurement and Characterization

5.3.1 Cyclic Voltammetry (CV) and Linear Sweep Voltammetry (LSV)

Cyclic voltammetry (CV) curves of the copper plate electrode were recorded in 0.1 M KOH solution with and without ultrasound. The scan rate was set to 50 mV/s within the voltage range of 0 to -2.3 V vs. SCE. Linear sweep voltammetry curves were obtained for the copper plate electrode within the same voltage range and electrolyte, employing a scan rate of 5 mV/s. Thereafter, bulk electrolysis experiments were conducted for 15 minutes at an applied potential of −2.3V vs SCE for the sonoelectrochemical reduction of CO_2.

5.3.2 Electrochemical impedance spectroscopy (EIS)

Electrochemical impedance spectroscopy (EIS) was conducted to investigate the variation in the electrical properties of the electrolytic set-up. It was carried out at a frequency range of 1×10^{5} to 1×10^{-1} Hz, with an amplitude of 5.00 mV applied at open circuit potential. The equivalent circuit model parameters were determined using Gamry Echem Analyst software.

The model with the smallest chi-squared (χ^2) value was selected to elucidate the electrochemical processes occurring on the electrode surface.

5.3.3 Analysis of Gas and Liquid Products

The gaseous products resulting from sonoelectrochemical reduction of CO_2 were analysed using gas chromatography (GC). The measurements utilised an Agilent 8860 gas chromatograph system outfitted with a thermal conductivity detector. This system was configured with two Porapak Q columns and a MoleSieve 13X column. Before the analysis, the GC system was calibrated utilising certified standards of gas mixtures (5% H_2, 1% CO, 0.25% C_2H_4, 0.2% CH_4, and 0.15% C_2H_6, sourced from CK Gas Product Limited, U.K.). Fig. 5.2 represents an example of a gas chromatogram obtained using this standard gas mixture.

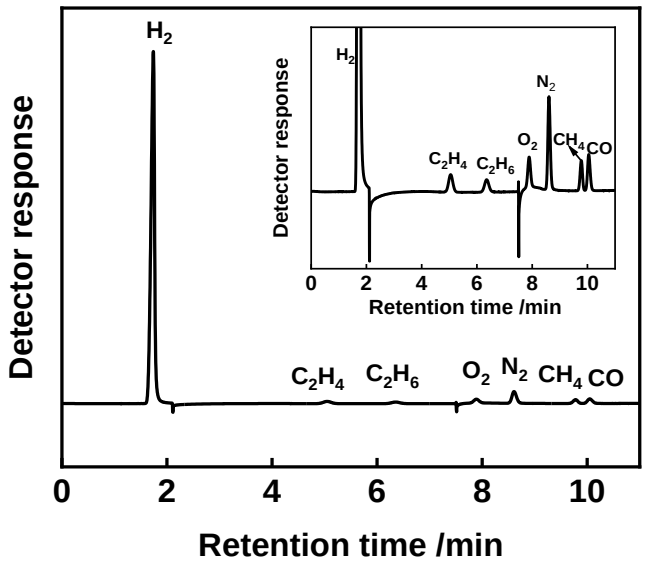

Figure 5.2: An example gas chromatogram of the gaseous mixtures (H_2, CO, CH_4, C_2H_4, and C_2H_6) with inset zoom of the chromatogram.

The quantification of liquid-phase products was conducted using ^1H nuclear magnetic resonance (NMR) spectroscopy (400 MHz, Bruker). ^1H NMR standards were prepared by making solutions of known concentration, mixing them with the internal standards solution, and collecting a ^1H NMR spectrum with the same parameters to be used to quantify experimental samples. To record ^1H NMR spectra, the water suppression technique was applied for all samples. A mixture of 640 µL of the post-electrolysis electrolyte solution, 70 µL of D_2O, and 30 µL of an internal standard solution (comprising 10 mM dimethyl sulfoxide-D6 and 50 mM phenol) was prepared for analysis. The obtained peaks are

identified and integrated, and their areas are expressed relative to the respective peak areas of the internal standards (phenol peaks at 7.32 and 6.91 ppm; DMSO peak (2.50 ppm)). Figure 5.3 shows a ^{1}H NMR spectrum illustrating potential liquid-phase CO_2 reduction products, including a formic acid peak at 8.40 ppm. Additionally, the spectrum includes an internal standard comprising dimethyl sulfoxide-D6 and phenol. Product concentrations were determined by comparing the ratio of each internal standard peak area to the obtained product.

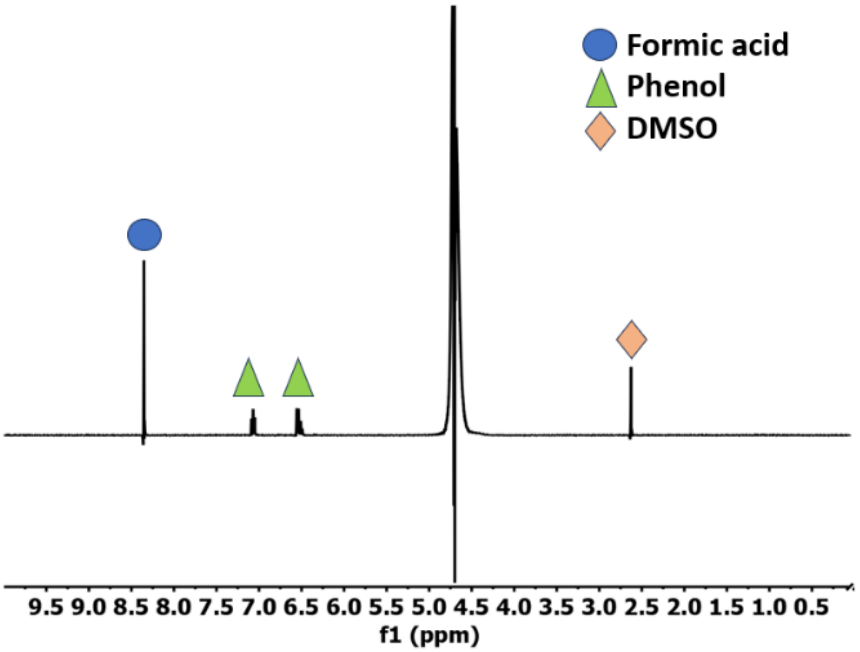

Figure 5.3: An example ^{1}H NMR spectrum illustrating liquid-phase CO_2 reduction product: formic acid with internal standard dimethyl sulfoxide-D6 (DMSO) and phenol.

5.4 Results and Discussion

The acoustic power generated at different input power percentages of 40, 60, 80, and 100% settings for the two examined frequencies (37 and 80 kHz) was measured using the calorimetry method.[9,13] The acoustic power of the ultrasonic bath was assessed by measuring the rate of temperature increase using a commercial thermocouple connected to a data logger (USB TC-08, Pico Technology). The thermocouple was placed in a fixed position within a water sample, as illustrated in Figure 5.1 and sonicated for 150 seconds. The outcomes of our findings in this study are presented in Table 5.1.

Table 5.1: Faradaic efficiency results from the bulk electrolysis of a CO_2 saturated 0.1 M KOH electrolyte on a Cu plate electrode in the absence and presence of ultrasound.

Entry	Reduced Gas	Ultrasound	Acoustic power density (Watt/Liter)	Temperature	Applied potential (V *vs* SCE)	Time (minute)	Charge (Columb)	Faradaic efficiency (FE) %					FE_{total} (%)
								H_2	CO	CH_4	C_2H_4	HCOOH	
1	CO_2	Absent	-	25 °C	−2.3	15	80.6	91± 3.9	1.1± 0.11	-	-	2.7± 0.21	94.9± 4.2
2	CO_2	37 kHz	155.62 ± 29.2	25 °C	−2.3	15	91.4	86.6± 3.8	1.2± 0.13	1.9± 0.16	0.6± 0.05	1.5± 0.14	91.7± 4.3
3	CO_2	80 kHz	81.69 ± 3.7	25 °C	−2.3	15	148.1	90.2± 3.5	0.3± 0.02	-	-	1.6± 0.15	92.1± 3.7
4	CO_2	Absent	-	4 °C	−2.3	15	90.9	80.0± 3.1	1.0± 0.10	0.4± 0.03	0.1± 0.01	0.7± 0.04	82.3± 3.3
5	CO_2	37 kHz	155.62 ± 29.2	4 °C	−2.3	15	185.5	76.1± 2.8	0.5± 0.04	0.2± 0.02	-	2.2± 020	78.9± 3.1
6	CO_2	80 kHz	81.69 ± 3.7	4 °C	−2.3	15	184.9	62.6± 2.4	2.1± 0.19	0.3± 0.02	-	0.2± 0.02	65.3± 2.6

Furthermore, after careful examination of the obtained Faraday efficiency in Table 5.1 (generally less than 100%), we inferred there are other possible side products which were not captured from the used assays. Therefore, we went further to investigate potential products such as hydrogen peroxide and oxalate. This investigation was prompted by the fact that ultrasound irradiation of water can lead to the production of H_2O_2.[9]

H_2O_2 can be produced from water through two steps; Water breaks down into hydroxyl radicals ($^{\bullet}OH$) and hydrogen (H). Hydroxyl radicals combine to form hydrogen peroxide through the following reactions:

$$H_2O \longrightarrow {}^{\bullet}OH + H \qquad (\textit{Equation 5.1})$$

$$2{}^{\bullet}OH \longrightarrow H_2O_2 \qquad (\textit{Equation 5.2})$$

As outlined in the reference, a well-established method utilising iodometry techniques was employed to determine the amount of H_2O_2 produced.[7,9,12] This method involves the oxidation of iodide ions (I^-) by H_2O_2 in the presence of a molybdate catalyst, leading to the formation of iodine (I_2). Subsequently, the generated iodine reacts with excess iodide to produce triiodide (I^{3-}), which exhibits a strong ultraviolet absorbance peak at 350 nm (with an extinction coefficient, ε, approximately 26,000 L mol^{-1} cm^{-1}). Thus, the concentration of triiodide indicates the amount of H_2O_2 generated during bulk electrolysis, offering insights into the sonoelectrochemical processes. The formation of the $CO_2^{-\bullet}$ radical anion is thermodynamically challenging due to the energy required for structural reorganisation from a linear molecule to a bent radical anion. In sonoelectrochemistry experiments, the ultrasonic effect may provide extra impetus to overcome the activation barrier, thereby facilitating the transformation of CO_2 into the $CO_2^{-\bullet}$ anion radical (equation 5.3). This anion radical subsequently undergoes dimerisation to form oxalates (equation 5.4):[8]

$$CO_2 + e^- \longrightarrow CO_2^{-\bullet} \qquad \textit{(Equation 5.3)}$$

$$2CO_2^{-\bullet} \longrightarrow C_2O_4^{2-} \qquad \textit{(Equation 5.4)}$$

To quantify oxalic acid, the post-electrolysis solution was analysed using an Agilent high-performance liquid chromatography (HPLC) system equipped with an Aminex HPX-87H column (300 mm × 7.8 mm). The mobile phase consisted of 0.1% formic acid in acetonitrile (HPLC grade) and 0.1% formic acid in water, mixed in a 30:70 ratio, respectively. The HPLC system operated at a flow rate of 0.6 mL/min, a temperature of 60°C, and sustained a pressure of 55.5 bar. Detection occurred within a wavelength range of 210 - 230 nm to enable precise determination of oxalic acid in the samples.

The Faradaic efficiencies (FE) of the gaseous and liquid products resulting from CO_2 reduction were calculated using Equation 1.9 in section 3.4.2 Faraday Efficiency and YieldChapter 1.

The experiments were conducted in triplicate for each setting, and the mean ± standard deviation was calculated. The mean temperature was plotted against time, and the acoustic power was estimated using equation 5.5.[13]

$$P_{ac} = \left(\frac{dT}{dt}\right)_{t=0} m\, C_p \qquad (Equation\ 5.5)$$

Where P_{ac} is the estimated acoustic power; $\left(\frac{dT}{dt}\right)_{t=0}$ is the rate of change in the temperature of the water sample due to heat dissipated because of energy conversion; m and C_p are the mass and specific heat capacity of the water sample, respectively.

Figure 5.4 illustrates that the acoustic power at a lower frequency of 37 kHz exceeds that at a higher frequency of 80 kHz. The distinction in acoustic power between the two frequencies may be attributed to the characteristics of the cavitation regime. Since the mean bubble size is inversely proportional to the ultrasound frequency, bubbles generated from lower frequencies are often larger.[14] Bubbles generated at lower frequencies undergo more vigorous collapse (inertial cavitation) than those at higher frequencies, which typically experience stable cavitation.[15]

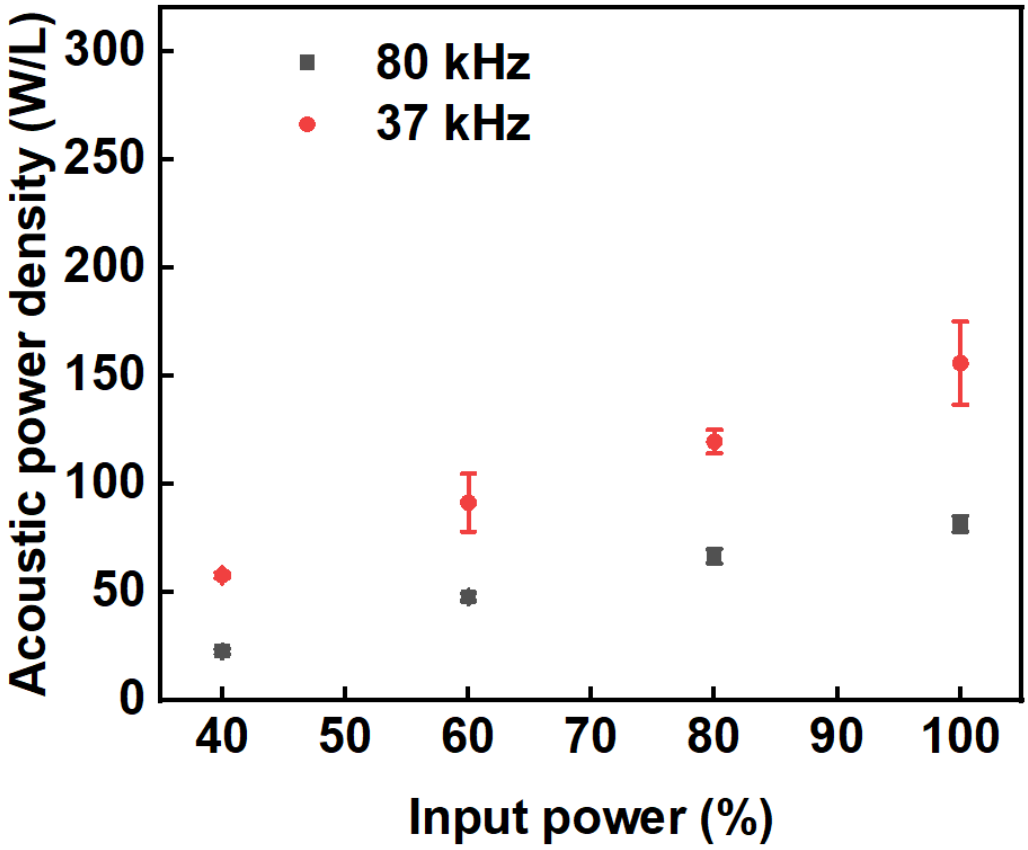

Figure 5.4: The variation of acoustic power density obtained at two different frequencies (37 and 80 kHz) against the percentage input power setting.

At both frequencies, the observed acoustic power density increased with an increase in the percentage of electrical input power to the ultrasonic bath. The maximum acoustic power density under both frequencies occurs when the percentage of electrical input is 100%. However, the acoustic power density obtained at 37 kHz was found to be higher than the corresponding acoustic power density at 80 kHz, as seen in Figure 5.4. Therefore, the 100% power setting was chosen at the power setting value that was used for the bulk sonoelectrochemical reduction of CO_2.

We explore the combined impact of frequency and power by conducting a linear sweep voltammetry experiment in CO_2-saturated 0.1 M KOH solution at a scan rate of 5 mV/s. The frequencies of 80 kHz and 37 kHz were tested separately, each at different input electrical power settings (40, 60, 80, and 100%), all performed at room temperature, as shown in Figure 5.5. It was noted that a lower frequency (37 kHz) resulted in a correspondingly higher current density compared to an 80 kHz frequency (Figure 5.5a). This observation can be attributed to more efficient electron transfer processes at the electrode interface due to the higher acoustic power at 37 kHz.[16] Furthermore, when the acoustic power setting was raised to 100%, the subsequent increase in current density suggested enhanced mass transport of

charge ions and a more significant effect on electrode activation. Consequently, this led to greater electrochemical activity (refer to Figure 5.5b). Hence, combining a lower frequency and maximum power setting demonstrated the potential to achieve considerably higher current densities in the linear sweep voltammetry experiment.

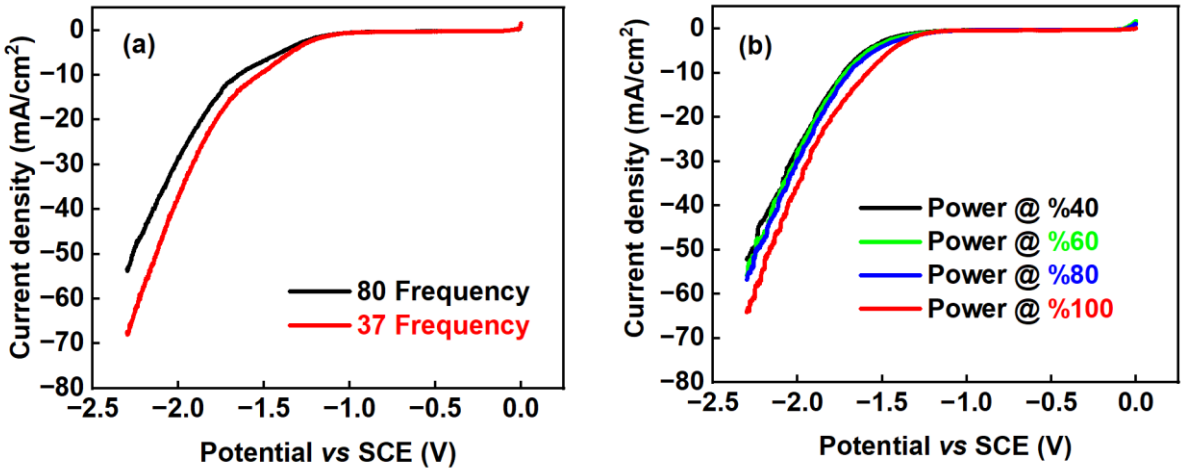

Figure 5.5: Linear sweep voltammogram curves of the copper plate electrode in CO_2-saturated 0.1 M KOH at 5 mV s^{-1}: (a) 80 kHz and 37 kHz, (b) at different percentages of acoustic power setting at room temperature.

It is important to note that the influence of temperature on the hydrogen evolution reaction and the selectivity of the CO_2 reduction reaction is a well-established fact. Rafaël *et. al*,[17] observed that at lower temperatures, as temperature increases, the production of certain products rises while maintaining a consistent preference for hydrogen generation. However, with further temperature increases, hydrogen becomes the primary product, leading to a decrease in the efficiency of CO_2 conversion on copper substrate.

Hence, the impact of temperature on both the hydrogen evolution reaction (HER) and the CO_2 reduction reaction (CO2RR), in the absence and presence of ultrasound, was investigated through linear sweep voltammetry conducted at both room temperature and 4°C. The observations under both conditions are depicted in Figure 5.6(a and b).

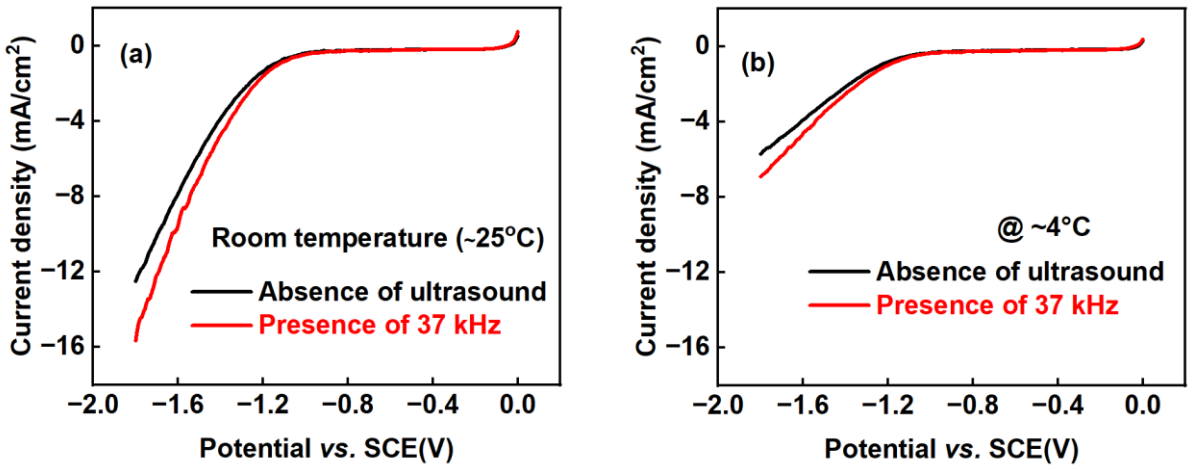

Figure 5.6: Linear sweep voltammogram curves of the copper plate electrode in CO2-saturated 0.1 M KOH at 5 mV s−1 in the absence and presence of 37 kHz at 100 % acoustic power setting under two different temperature conditions: (a) at room temperature and (b) at 4°C.

The acquired LSV curves distinctly indicate that, at both room temperature and 4 °C (Figure 5.6(a and b)), the current density is higher in the presence of ultrasound. This is attributed to ultrasound enhancing the movement of protons from the solution to the electrode. Nevertheless, at room temperature (Figure 5.6a), a shift in the onset potential for CO_2 reduction towards more positive potentials was noted compared to 4°C (Figure 5.6b). This alteration may be potentially influenced by an increase in the hydrogen evolution reaction.[16,18]

Electrochemical impedance spectroscopy (EIS) measurements were also performed to elucidate the charge transfer behaviour and ascertain the electrochemical parameters on the copper electrode surface, both with and without ultrasound at room temperature. For comparison, the EIS results are depicted in the form of Nyquist plots in Figure 5.7, along with electrical equivalent circuit models of the copper electrode. The electrical equivalent circuit model, which describes the electrode process, was developed by fitting the experimental impedance data using Gamry Echem Analyst, as illustrated in Figure 5.7.[19]

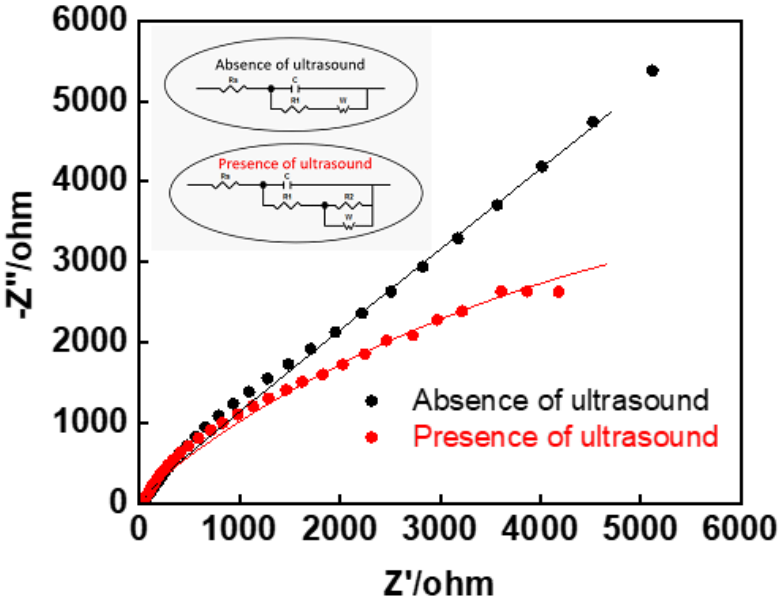

Figure 5.7: Nyquist plots for copper plate electrode in saturated CO_2 0.1 M KOH at 5 mV/s in the absence and presence of 37 kHz at 100 % acoustic power setting at room temperature. The cycle points represent experimental data, while the continuous curves depict model fitting. (Inset: the electrical equivalent circuit models of the copper electrode in the absence/presence of ultrasound).

Table 5.2 summarises the electrical parameters and corresponding percentage errors derived from fitting the electrochemical impedance spectroscopy measurements for the copper electrodes.

Table 5.2: The obtained electrical equivalent parameters employed for modelling the EIS data of copper electrodes in the absence and presence of 37 kHz, 100% acoustic power at room temperature.

Ultrasound	R_s [Ω cm^{-2}]	C [$\mu F cm^{-2}$]	R_1 [Ωcm^{-2}]	R_2 [Ωcm^{-2}]	W [$\Omega s^{-1} cm^{-2}$]	R_{total} [Ω cm^{-2}]	Chi-squared ($\chi 2$)
Absent	26.5	6.60×10^{-6}	1.10×10^{-2}	-	1.80×10^{-4}	26.5	1.10×10^{-2}
Present	9.9	1.28×10^{-5}	2.25×10^{-2}	7.82	3.70×10^{-4}	17.8	9.20×10^{-3}

In the equivalent circuit model, R_s refers to the solution resistance, while R_1 and R_2 represent charge transfer resistances. The C, which represents the constant phase element, is commonly employed to describe the double-layer capacitance, and W indicates the Warburg impedance associated with the diffusion process, playing an important role during the electrochemical reduction of CO_2. From the Nyquist plot, it can be seen that the charge transfer resistance of the Cu electrode during sonication is smaller, with a lesser enclosed area of a semicircle than without sonication. Additionally, the total resistance of the layer (R_{total}), indicating all resistance values, is also calculated (see Table 5.2). Remarkably, this value decreases from 26.5 Ω cm^{-2} in the absence of ultrasound to 17.8 cm^{-2} in its presence. Hence, ultrasound improves charge transfer at the semiconductor/electrolyte interface during sonoelectrochemistry. To the best of our knowledge, this is the first experimental evidence supporting this theory.

The bulk sonoelectrochemical reduction of CO2 was performed in CO2-saturated 0.1 M KOH for 15 minutes under different conditions (with and/or without ultrasound at frequencies of 37 kHz and 80 kHz and at temperatures of 25°C and 4°C) while maintaining an applied potential value of −2.3 V vs SCE. After each experiment, gas products from the headspace of the electrochemical cell were analysed using gas chromatography, while liquid products were examined using ^{1}H NMR, LC-MS, and UV–vis spectrometer. The resulting data of current density vs. time is illustrated in Figure 5.8. During the ultrasound-assisted experimental conditions, the current density increases at the onset of the experiment, attributed to ultrasound facilitating the transfer of a substantial quantity of dissolved CO_2 from the bulk solution to the surface of the copper electrode.[16] Under ultrasonic conditions, the initial increase in current density was more noticeable owing to improved charge transfer, as mentioned earlier. Over time, the current density stabilises, possibly due to the deposition of carbon or copper oxide on the electrode, indicated by the black colour deposit observed on the Cu electrode's surface post-electrolysis.

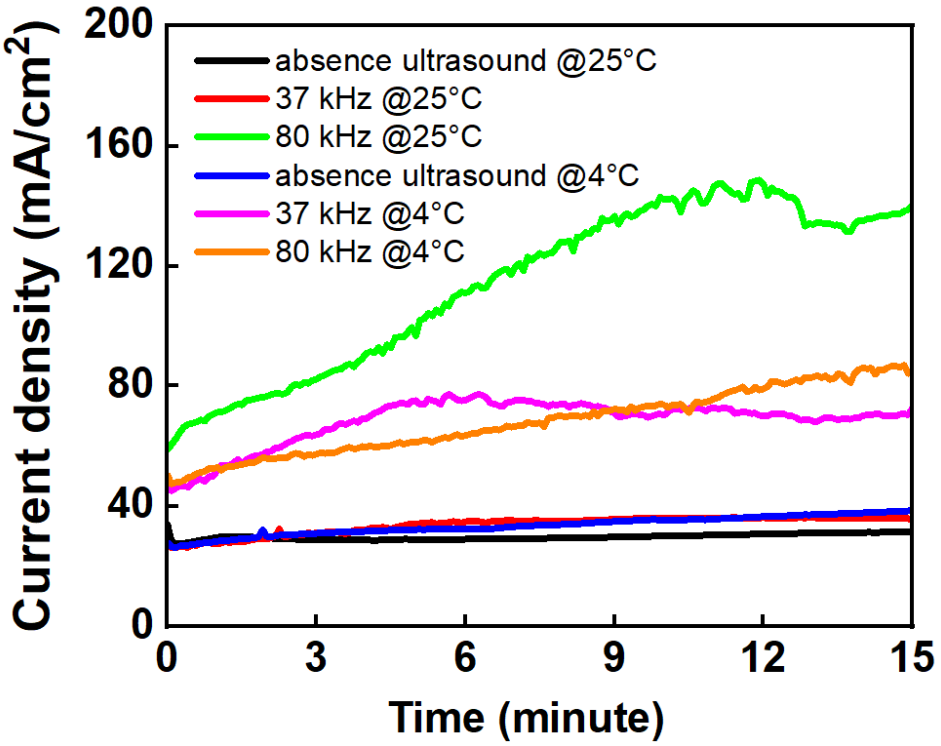

Figure 5.8: The obtained current densities vs time for copper electrodes from the bulk electrolysis of a CO_2 saturated 0.1 M KOH electrolyte at –2.3 V *vs* SCE on a Cu plate electrode in the absence/presence (37 kHz, 80 kHz) of ultrasound at 25 ° C and 4°C.

The different liquid and gas products from bulk sonoelectrolysis are outlined in Table 5.1. The specifics of the liquid and gaseous products obtained are delineated in Figures 5.9 and 5.10, respectively. The products obtained from the sonoelectrochemical reduction of CO2 may necessitate varying numbers of electrons, contingent upon the type and characteristics of the product. For example, products such as CO/HCOOH, CH_4, and C_2H_4 require 2, 8, and 12 electrons transfer, respectively. This implies that products like C_2H_4 require a greater reduction of CO_2 than CO, HCOOH and CH_4. Figure 5.9 shows the characteristic ^{1}HNMR spectra from the bulk electrolysis of a CO_2-saturated 0.1 M KOH electrolyte at –2.3 V *vs* SCE. For ^{1}HNMR peaks representing the areas of internal standard and the products as represented in Figure 5.9, phenol peaks are at 7.32 and 6.91 ppm, DMSO peak at 2.50 ppm, and formate peak at 8.40 ppm.

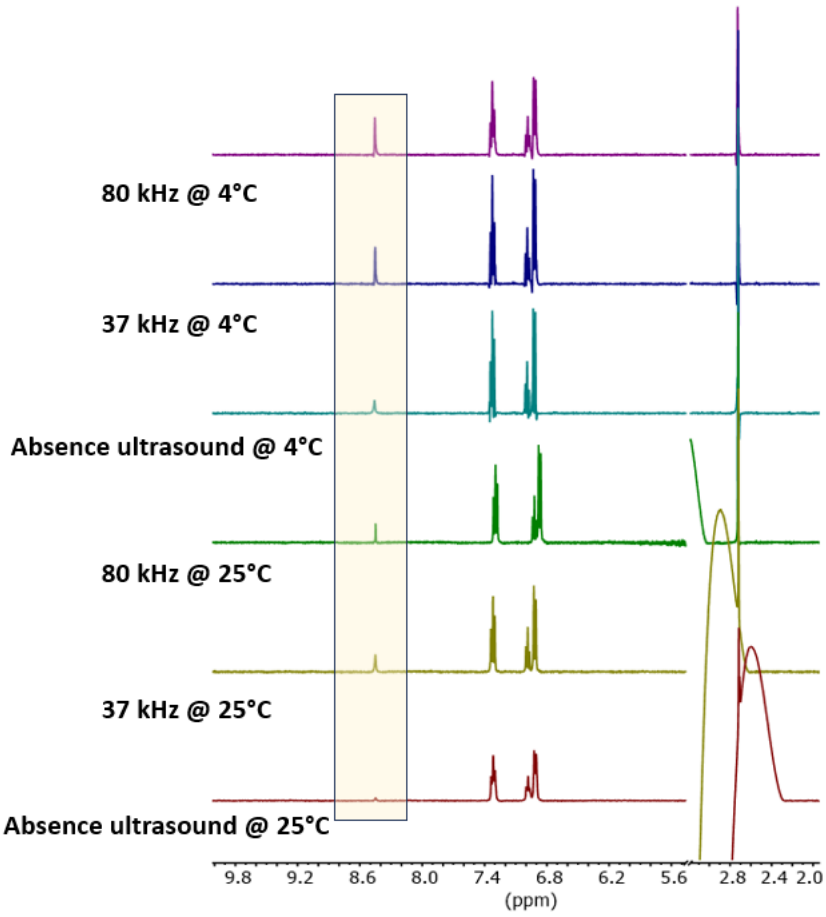

Figure 5.9: ^{1}H NMR spectra from the bulk electrolysis of a CO_2 saturated 0.1 M KOH electrolyte at –2.3 V vs SCE on a Cu plate electrode in the absence/presence (37 kHz, 80 kHz) of ultrasound at 25 ° C and 4°C. (The gap in the x-axis eliminates the water peak).

When comparing Faradaic efficiencies, as indicated in Table 5.1, it is notable that the presence of ultrasound resulted in improved Faradaic efficiency across all CO2 reduction products, particularly with 37 kHz ultrasound. Conversely, in the absence of ultrasound, the hydrogen evolution reaction predominated over the reduction of CO2, consistently observed at both temperatures (25°C and 4°C). Throughout the sonoelectrochemical experiment, substantial energy is produced by cavitation bubbles, notably influenced by temperature. This energy can potentially trigger the homolytic fission of molecular H_2, leading to the formation of hydrogen radical ($H^{\bullet}$), which is subsequently utilised in the reduction process.[16] Hence, hydrogen's Faradaic efficiency is lower in the presence of ultrasound. Figure 5.10 illustrates the gas chromatography outcomes obtained from the bulk electrolysis of a CO_2-saturated 0.1 M KOH electrolyte at −2.3 V vs SCE on a Cu plate electrode, both in the absence and presence (at 37 kHz and 80 kHz) of ultrasound at 25°C and 4°C.

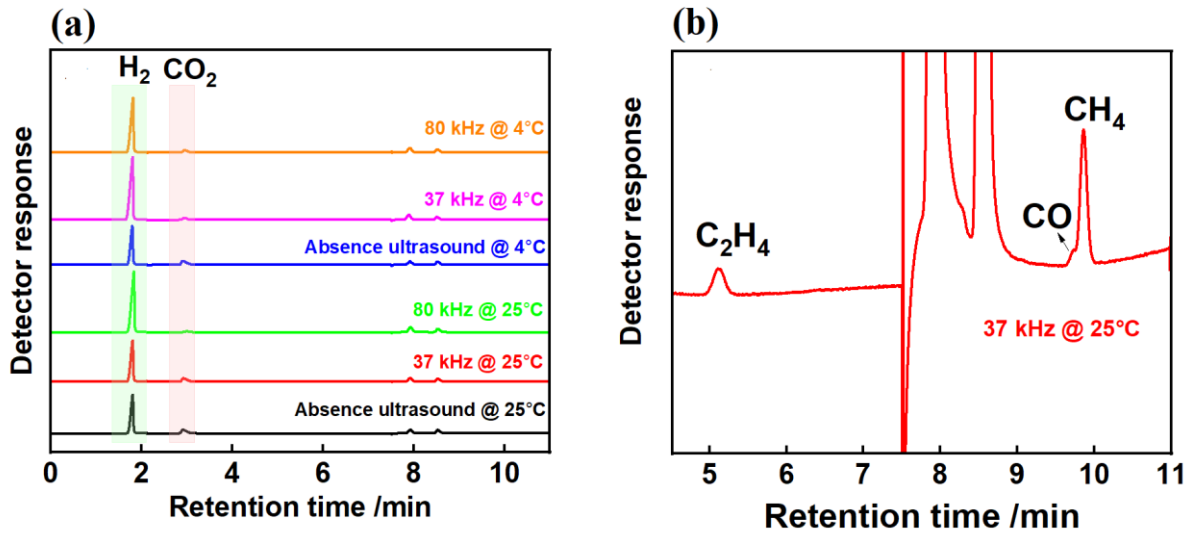

Figure 5.10: Gas chromatography results from the bulk electrolysis of a CO_2 saturated 0.1 M KOH electrolyte at –2.3 V vs SCE on a Cu plate electrode in the absence/presence (37 kHz, 80 kHz) of ultrasound at 25 ° C and 4°C (a), example zoomed gas chromatogram obtained in the presence of 37 kHz ultrasound at 25 ° C.

In the electrochemical reduction process assisted by ultrasound, a beneficial synergy arises at the interface between the electrode and electrolyte, facilitating the generation of more profound CO_2 reduction products. As mentioned earlier, additional analyses were performed on the liquid products using LC-MS to potentially detect the presence of oxalate ions, as it cannot be directly identified using ^{1}H NMR. Also, UV-vis spectrometry was performed on the liquid product to detect possible hydrogen peroxide. Figures 5.11 and 5.12 provide additional insights and detailed descriptions regarding determining oxalate ion and hydrogen peroxide concentrations in the post-electrolysis solution.

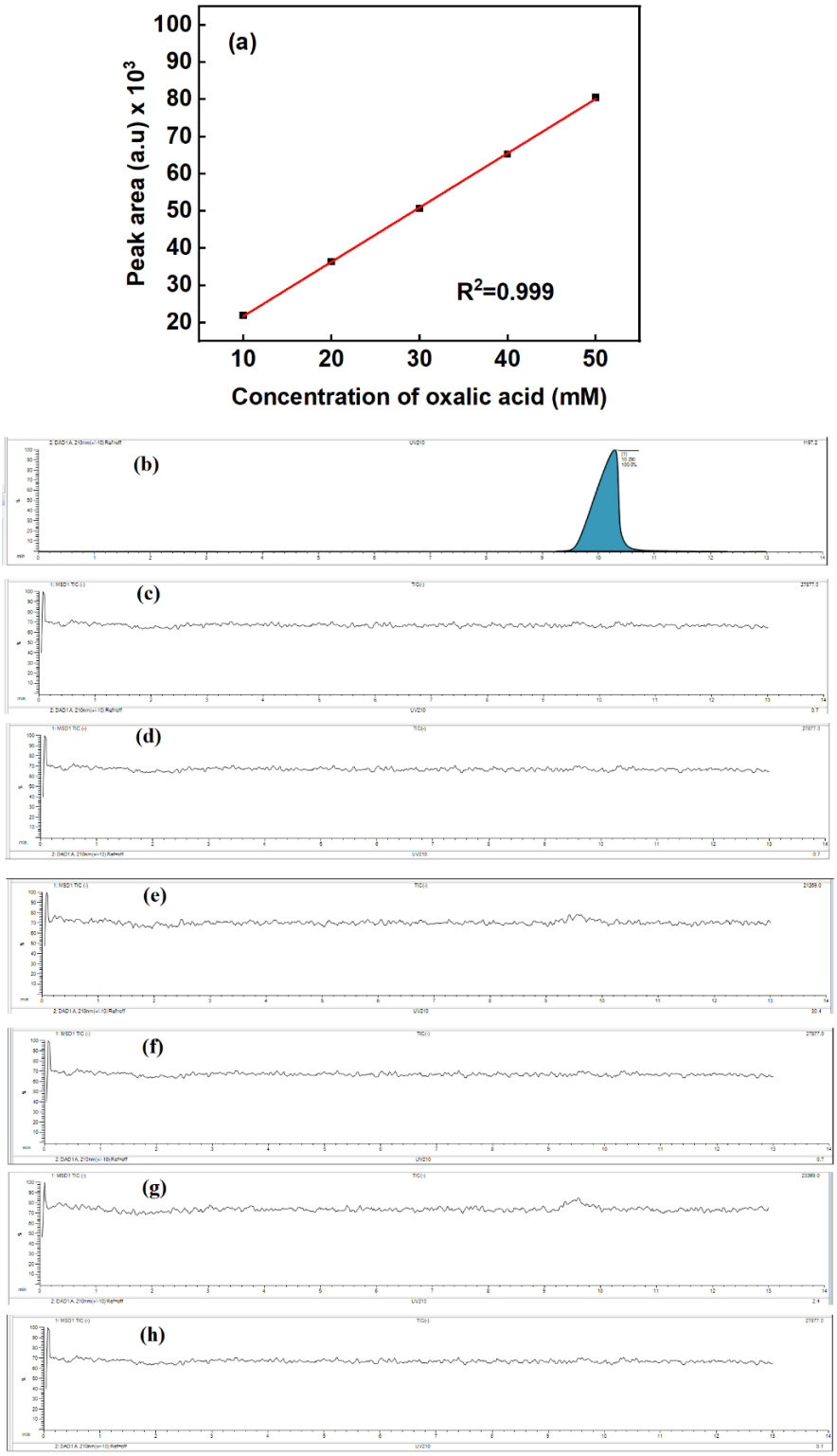

Figure 5.11: LC-MS calibration curve for oxalic acid (a), an LC-MS chromatogram example for oxalic acid (b), and LC-MS chromatograms obtained from the bulk electrolysis of a CO_2-saturated 0.1 M KOH electrolyte at –2.3 V vs SCE on a Cu plate electrode: without ultrasound at room temperature (c); with ultrasound at 37 kHz at room temperature (d); with ultrasound at 80 kHz at room temperature (e); without ultrasound at 4°C (f); with ultrasound at 37 kHz at 4°C (g); and with ultrasound at 80 kHz at 4°C (h).

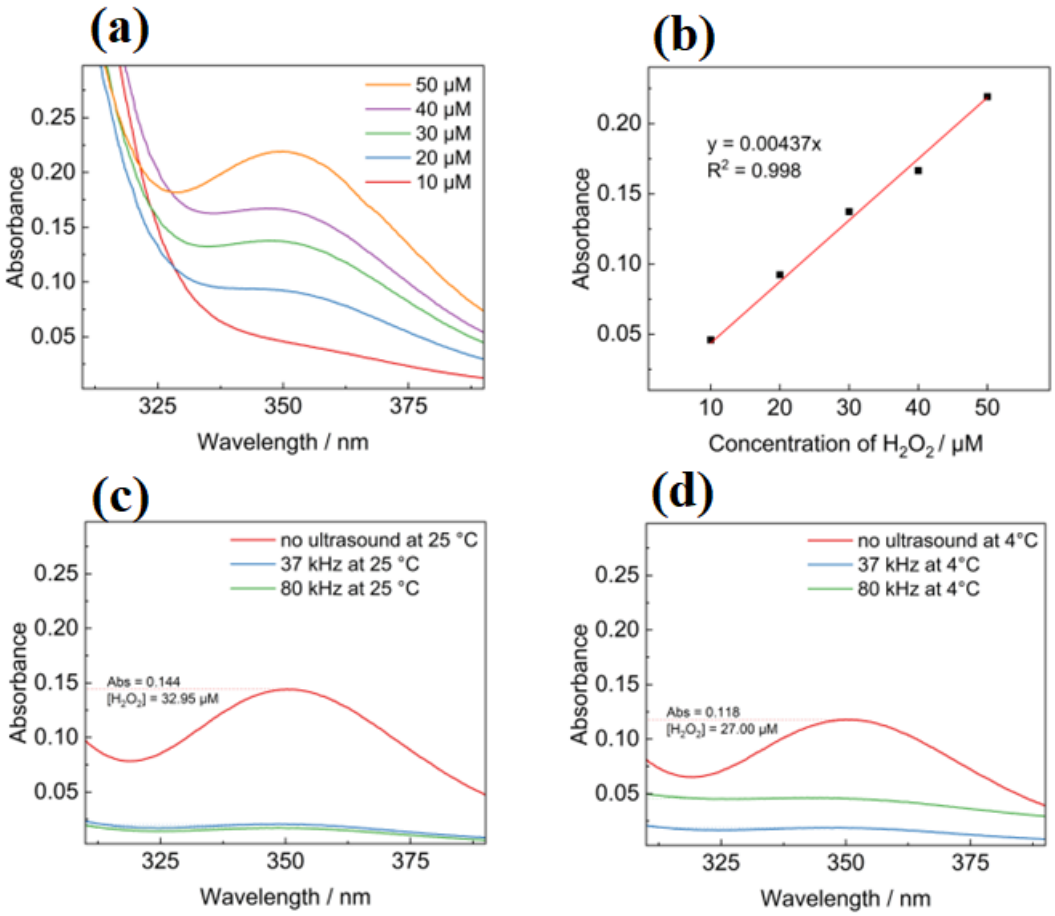

Figure 5.12: Hydrogen peroxide testing of sonoelectrochemically treated samples using iodometry: UV-vis spectra of standard H_2O_2 solutions (a), calibration curve for absorbance at λ = 350 nm *vs.* H_2O_2 concentration (b), results from hydrogen peroxide tests on CO_2-saturated 0.1 M KOH solution following bulk electrolysis at −2.3 V *vs.* SCE on a Cu plate electrode for 30 min with no ultrasound, 37 kHz ultrasound, and 80 kHz ultrasound at room temperature (c), and 4 °C (d).

Figures 5.11 and 5.12 also present the respective individual calibration curves for oxalic acid and H_2O_2 analysis. Regrettably, no substantial product amount of oxalate ion was detected during the sonoelectrochemical reduction of CO_2 under all experimental conditions (refer to Figure 5.11). In contrast, for hydrogen peroxide, yields of 32.95 and 29.00 µM were obtained at 25°C and 4°C, respectively, from bulk electrolysis of CO_2-saturated electrolyte without ultrasonic irradiation (see Figure 5.12). In experiments with ultrasound, yields in all instances were below the limit of detection of the iodometric test method. Although hydrogen peroxide is indeed a byproduct of the recombination of hydroxyl radicals formed during acoustic cavitation, probably, more of the hydroxyl radicals generated in the presence of ultrasound contribute to further reduction processes, potentially leading to deeper

reduction, as illustrated in the proposed mechanism in Figure 5.13 [20] Recent research has also proposed that the presence of CO_2 may enable an alternative electrochemical pathway for water oxidation to produce H_2O_2.[21] It is likely that any electrochemically generated H_2O_2 is cleaved by ultrasonic irradiation, as shown in Equation 5.6:[22]

$$H_2O_2 \xrightarrow{\textbf{ultrasound}} 2^{\bullet}OH \qquad (\textit{Equation 5.6})$$

Thus, this results in a decreased peroxide concentration in sonoelectrochemically treated solutions, most likely due to sonochemically induced dissociation and hydroxyl radical consumption. We suspect that there may be additional potential side products formed during sonoelectrochemical CO_2 reduction, which could account for the Faradaic efficiencies being less than 100%. Therefore, further research in this area is warranted to acquire deeper insights. Hence, alterations in both ultrasound frequency and temperature markedly influence the distribution of CO_2 reduction products. Particularly noteworthy is the pronounced effect observed at 37 kHz ultrasound and room temperature, which enhances the Faradaic efficiency of carbon monoxide (CO), methane (CH_4), and ethylene (C_2H_4) formation while diminishing the Faradaic efficiency of molecular hydrogen (H_2) and formic acid (HCOOH). In the presence of ultrasound, water generates hydroxyl radicals ($^{\bullet}OH$) and hydrogen radicals ($H^{\bullet}$). These radicals are capable of breaking or synthesising aliphatic compounds, facilitating CO_2 reduction processes. Therefore, the proposed pathways for CO_2 reduction facilitated by ultrasound-generated hydrogen radicals ($H^{\bullet}$) are given in Fig 5.13.[16] [20] The disparity in Faradaic efficiency observed when CO_2 is more profoundly reduced with ultrasound could stem from the electrochemically produced molecular hydrogen utilised in the radical-induced sonoelectrochemical CO_2 reduction reaction. The red arrow in Figure 5.13 depicts the alteration in the reduction pathway with ultrasound.

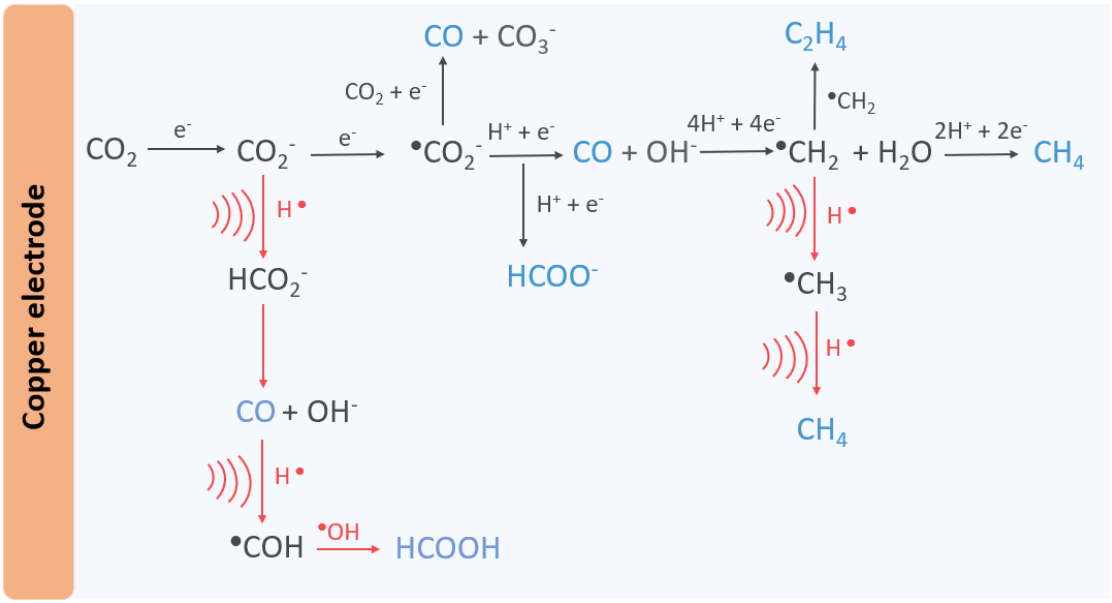

Figure 5.13: Proposed mechanism for electrochemical reduction of CO_2 on copper electrode in the absence/presence of ultrasound.

5.5 Conclusion

This research has explored the optimisations of sonoelectrochemical CO2 reduction across different ultrasound parameters (frequency and power). Across all percentage input power settings, it was observed that the acoustic power observed at a lower frequency of 37 kHz surpassed that of a higher frequency of 80 kHz, attributed to a more vigorous bubble collapse at 37 kHz. Furthermore, at a lower frequency of 37 kHz and the maximum power setting (100%), the linear sweep voltammetry experiment exhibited the highest current density among all ultrasound-assisted conditions. The experimental temperature has shown a distinct impact on the observed current density during linear sweep voltammetry experiments, with a higher current density recorded at room temperature than 4 °C. According to the results of electrochemical impedance spectroscopy, it was demonstrated that the total charge resistance value decreases in the presence of ultrasound, suggesting that ultrasound enhances charge transfer at the semiconductor/electrolyte interface during sonoelectrochemistry. This enhancement facilitates the reduction of CO_2 into deeper products. From GC and ^{1}H NMR analyses, it was observed that there could be alterations in the faradaic efficiency of CO, CH_4, and C_2H_4 formation under ultrasound. On the other hand, ultrasound leads to a decrease in the faradaic efficiency of H_2 and HCOOH, as indicated in Table 5.1. Moreover, it was observed that ultrasound diminishes the formation of H2O2, corroborating the consumption of hydroxyl radicals during the reduction process. This phenomenon aids in comprehending

further reduction processes, potentially resulting in deeper reductions as proposed by the new mechanism. Intriguingly, the anticipated electrochemical CO_2 reduction products of oxalate ions were not detected under any experimental conditions. To sum up, this study highlights important parameters and suggests potential improvements for enhancing reduction processes in future applications.

5.6 References

1 J. Zhang, C. Guo, S. Fang, X. Zhao, L. Li, H. Jiang, Z. Liu, Z. Fan, W. Xu, J. Xiao and M. Zhong, *Nat. Commun.*, 2023, **14**, 1–11.

2 D. Saygin, H. Blanco, F. Boshell, J. Cordonnier, K. Rouwenhorst, P. Lathwal and D. Gielen, *Sustain.*, , DOI:10.3390/su15021623.

3 K. Wiranarongkorn, K. Eamsiri, Y. S. Chen and A. Arpornwichanop, *J. CO2 Util.*, 2023, **71**, 102477.

4 S. C. Perry, P. ki Leung, L. Wang and C. Ponce de León, *Curr. Opin. Electrochem.*, 2020, **20**, 88–98.

5 Y. Yang, Y. Feng, K. Li, S. Ajmal, H. Cheng, K. Gong and L. Zhang, *Ultrason. Sonochem.*, 2021, **76**, 105623.

6 Z. Ma, Z. Yang, W. Lai, Q. Wang, Y. Qiao, H. Tao, C. Lian, M. Liu, C. Ma, A. Pan and H. Huang, *Nat. Commun.*, 2022, **13**, 1–11.

7 C. Kormann, D. W. Bahnemann and M. R. Hoffmann, *Environ. Sci. Technol.*, 1988, **22**, 798–806.

8 E. Schuler, M. Demetriou, N. R. Shiju and G. J. M. Gruter, *ChemSusChem*, 2021, **14**, 3636–3664.

9 L. A. Yusuf, Z. Ertekin, S. Fletcher and M. D. Symes, *Ultrason. Sonochem.*, 2024, **103**, 106792.

10 L. Yusuf, M. D. Symes and P. Prentice, *Ultrason. Sonochem.*, 2021, **70**, 105273.

11 D. L. Goldfarb, H. R. Corti, F. Marken and R. G. Compton, *J. Phys. Chem. A*, 1998, **102**, 8888–8893.

12 S. Merouani, O. Hamdaoui, F. Saoudi and M. Chiha, *J. Hazard. Mater.*, 2010, **178**,

1007–1014.

13 J. Ramsay, *Eur. J. Purch. Supply Manag.*, 1996, **2**, 129–143.

14 S. K. Bhangu and M. Ashokkumar, *Top. Curr. Chem.*, 2016, **374**, 1–28.

15 G. J. Price, M. Ashokkumar, M. Hodnett, B. Zequiri and F. Grieser, *J. Phys. Chem. B*, 2005, **109**, 17799–17801.

16 M. H. Islam, H. Mehrabi, R. H. Coridan, O. S. Burheim, J. Y. Hihn and B. G. Pollet, *Ultrason. Sonochem.*, 2021, **72**, 105401.

17 R. E. Vos, K. E. Kolmeijer, T. S. Jacobs, W. Van Der Stam, B. M. Weckhuysen and M. T. M. Koper, *ACS Catal.*, 2023, **13**, 8080–8091.

18 A. Goyal, G. Marcandalli, V. A. Mints and M. T. M. Koper, *J. Am. Chem. Soc.*, 2020, **142**, 4154–4161.

19 M. N. Hossain, J. Wen and A. Chen, *Sci. Rep.*, 2017, **7**, 1–10.

20 K. Ohta, K. Suda, S. Kaneco and T. Mizuno, *J. Electrochem. Soc.*, 2000, **147**, 233.

21 L. Fan, X. Bai, C. Xia, X. Zhang, X. Zhao, Y. Lu, Y. Liu, H. Wang, Y. Xia and Z. Wu, *Nature Communications,* 2022, 1–9.

22 M. Lim, Y. Son and J. Khim, *Ultrason. - Sonochemistry*, 2014, **21**, 1976–1981.

Final Conclusions and Future Work

6.1 Final Conclusions

In this thesis, we studied the application of a suitable catalyst and optimisation of various parameters for the electrochemical reduction of CO_2 to oxalic acid in an organic solvent. Oxalic acid has been a versatile chemical and a major raw material for the production of other chemicals of industrial importance. We went further to electrochemically reduce oxalic acid to glyoxylic and glycolic acid, which are also chemicals with high market demand due to their applications in various sectors. Exploring alternative methods of producing valuable chemicals like oxalates paves the way for reducing dependence on traditional fossil carbon, which has been the main source of producing industrial chemicals. By converting CO_2 into chemicals or chemical intermediates for producing other chemicals, three cardinal objectives could be achieved: climate change mitigation, pollution control, and promoting the concept of a circular economy by transforming waste into valuable resources.

In **Chapter 3,** we electrochemically reduced CO_2 to oxalic acid and other valuable chemicals. Our process is a simple and potentially more sustainable one because we can reduce CO_2 in propylene carbonate with appreciable product yield and Faradaic efficiency at lower applied potential. This was achieved by adding 2 mM benzonitrile to 0.2 M tetraethylammonium chloride in propylene carbonate. The outcome of our investigations from cyclic voltammetry indicates a decrease in the onset potential of CO_2 reduction upon application of benzonitrile to the electrolyte. Also, analysis of product yields from bulk electrolysis suggests that the application of benzonitrile to the organic solvent enhances the combination of CO_2 anion radicals ($CO_2^{-\bullet}$) generated on the Pb electrode to form oxalate/oxalic acid, thereby increasing the Faradaic efficiency of the system. To further optimise system performance and determine the optimal potential for CO_2 reduction in the organic solvent, we evaluated a range of reduction potentials (from –2.2 to –2.7 V vs SCE) obtained from cyclic voltammetry measurement. Our experimental findings established –2.7 V vs SCE as the optimal potential for the process. As we go more negative beyond this potential, the electrode begins to exhibit some level of degradation. Consequently, we stopped the evaluation of potential at –2.7 V. The successful electrochemical reduction of CO_2 to oxalate/oxalic acid in propylene carbonate, assisted by benzonitrile at a relatively low applied potential, using a three-electrode setup in an H-cell, has yielded preliminary evidence for its potential application in scaled-up reactions within flow cells or industrial setups.

In **Chapter 4,** we reported for the first time the application of the native oxides of titanium on titanium-based electrodes (Ti/Ti_xO_y) as a catalyst in the electrochemical reduction of oxalic acid in an aqueous medium. Significant progress in electrochemistry has highlighted the valuable electrochemical and electrocatalytic properties of titanium electrodes.[1] Additionally, Ti_xO_y films have gained attention as electrocatalysts, especially in the domain of organic synthesis.[2,3] The growing interest in utilising titanium sub-oxide (Ti_xO_y) as an electrode or a support material for electrochemical applications stems from its distinctive physical and chemical properties, remarkable corrosion stability in alkaline and acidic environments, affordability, and low toxicity.[4–6] We exploit the exceptional properties of native titanium oxides and apply them in the electrochemical reduction of oxalic acid. 0.03 M oxalic acid in 0.2 M Na_2SO_4 solution was electrochemically reduced to glyoxylic and glycolic acids. The outcome suggests a relatively better conversion of the starting material and overall product yield when compared to other titanium-based electrodes that are deliberately modified or the Ti-oxides that are synthesised for the same purpose. These results in turn suggest that unmodified Ti electrodes bearing the naturally forming native Ti-oxides on their surface are competent for oxalic acid reduction and that deliberate modifications or synthesising other forms of Ti oxides to the Ti surface may be unnecessary for acceptable performance. Although post-experimental evaluation of the titanium electrode (Ti/Ti_xO_y) by ellipsometry and electrochemical impedance spectroscopy (EIS) revealed a decrease in thickness of the native oxide, that does not significantly interfere with the catalytic effect needed from the electrode. Since these oxides are naturally forming, their application into industrial scale or flow cell systems for the production of glyoxylic and glycolic acid could potentially remove a large financial impediment to the development or synthesising Ti-oxides.

Finally, in **Chapter 5**, we investigated the synergistic effects of ultrasound and electrochemistry in the sonoelectrochemical reduction of CO_2 into useful chemicals. The integration of ultrasonic waves and electrochemical methods is anticipated to offer substantial benefits compared to conventional electroanalytical techniques. These benefits are facilitated by the production of acoustic cavitation bubbles during the sonoelectrochemical process, which occurs as a result of irradiation with ultrasound.[7] The cavitation induces acoustic streaming and shockwave phenomena,[8] which help to reduce issues like blockage on the surface of electrodes, mass transport limitations and poor reaction kinetics associated with traditional electrochemical methods.[9] In this study, we investigated

the electrochemical reduction of CO_2 using a copper plate electrode immersed in a CO_2-saturated 0.1 M KOH solution. Various ultrasound-assisted conditions, including variations in frequency (37 kHz and 80 kHz) and power levels (40%, 60%, 80% and 100%) were tested at both room temperature (~25°C) and 4°C. In the presence of ultrasound, the charge transfer at the semiconductor/electrolyte interface was enhanced, as evidenced by the decreased charge transfer resistance observed in electrochemical impedance spectroscopy (i.e., from 26.5 Ω cm^{-2} to 17.8 Ω cm^{-2} in the presence of ultrasound). In all conditions, the current density gradually increased with time until it eventually stabilized after a short period, attributed to the observed deposition of carbon/copper oxide on the electrode.

Previous studies have envisaged the positive influence of ultrasound on various electrochemical reactions, showcasing its potential as a tool for improving reaction kinetics and selectivity. However, to the best of our knowledge, this is the first time this theory has been corroborated with experimental evidence, which evaluated and optimised various parameters in sonoelectrochemical reduction of CO_2 on a copper electrode. Moreover, the hydrogen evolution reaction is known to be the major competing reaction in CO_2 electroreduction. The synergistic effect of ultrasound significantly reduced the occurrence of the hydrogen evolution reaction during CO_2 electroreduction across all tested conditions. To sum up, this study proposed a mechanism for sonoelectrochemical reduction of CO_2, highlighted and optimized important parameters for the process.

6.2 Recommendations for Future Work

Having electrochemically reduced CO_2 to oxalic acid and other valuable chemicals using a three-electrode setup in a laboratory set-up, as well as having optimised various parameters, it is worth noting that the preliminary findings suggest that the optimised data could be applied in larger-scale reactions due to the efficient performance recorded. To validate the potential use of the combination of tested solvents, catalysts, and optimised parameters in large-scale chemical production, further work is necessary. This involves integrating and replicating the experiments in a flow cell system that closely resembles an industrial setting as shown in Figure 6.1, rather than a laboratory H-cell.

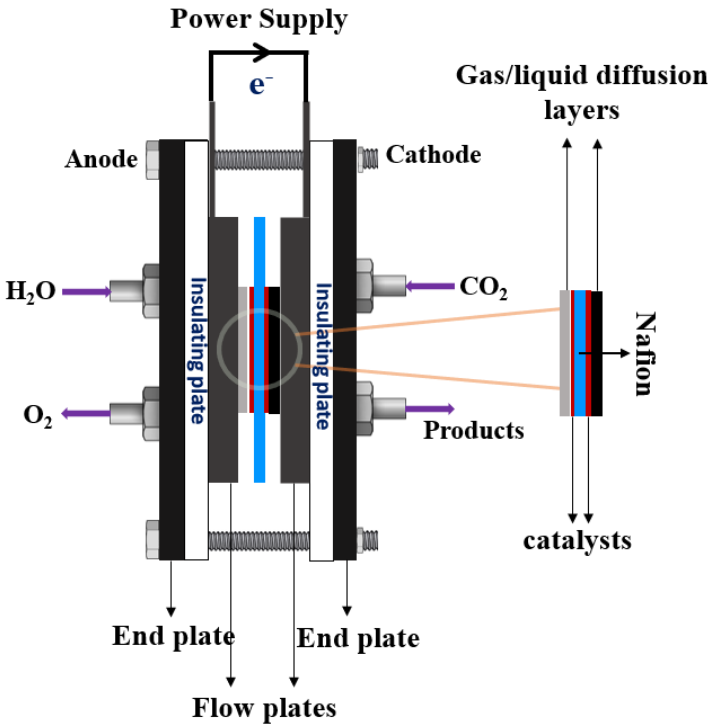

Figure 6.9: Schematic diagram of a flow cell for electrochemical reduction of CO_2

As a result, the following recommendations are proposed for additional research in this field:

In **chapter 3**, our results show that the use of Pb as a working electrode and benzonitrile as a homogeneous electrocatalyst improves the faradaic and reaction yields of oxalate/oxalic acid production, as well as the area-normalised rate of formation of oxalate/oxalic acid, giving a new record rate of formation of 1.65 ± 0.35 mM cm^{-2} h^{-1} (averaged over 1 h) at a voltage of –2.7 V vs. SCE (–2.46 V vs. SHE). The use of Pb on a large scale is discouraged due to its poisonous effect. Therefore, further research is needed to identify alternative cathode materials like gas diffusion electrodes or alloys of other metals that are safer and exhibit a similar or improved propensity for oxalate/oxalic acid formation.

In **Chapter 4**, our findings demonstrate that the direct reduction of oxalic acid to glyoxylic and glycolic acid can be accomplished with a high yield at room temperature, facilitated by the native oxides of titanium on titanium electrodes (Ti/Ti_xO_y). However, the outcome of the electrode characterisation by ellipsometry and electrochemical impedance spectroscopy (EIS) in a post-experimental analysis suggests a decrease in the thickness of the native oxide. The decrease in the oxide thickness should be further investigated in an experiment with long duration in a flow cell to ascertain the possibility of using the electrode/catalyst in a large-scale or industrial application.

In **Chapter 5**, we investigated the synergistic effects of ultrasound and electrochemistry in the sonoelectrochemical reduction of CO_2 on a copper electrode into useful products. The outcome suggests an interesting result which addresses the problem of bubble formation on the surface of the electrode and reduces charge transfer resistance by enhancing the mass transport of electroactive species through acoustic streaming and cavitation phenomena. In addition, the optimal power and ultrasound frequency have been established based on the current setup. These optimised parameters and the synergistic performance suggest a potential improvement in enhancing CO_2 reduction processes in future applications. Considering the fact that only a copper electrode was investigated, different electrodes should also be examined in sonoelectrochemical setups to determine the various CO_2 reduction products obtainable from the system. For this approach to be employed industrially, the energy requirements of the sonoelectrochemical process need to be re-examined. One such approach is by applying a pulse width modulated ultrasonic regime to minimise the energy usage by the transducer and improve the cavitation efficiency.

6.3 References

1 S. Popescu, C. Ungureanu, A. Albu, C. Pirvu, *Progress in Organic Coatings,* (2014), **77**, 1890–1900.

2 L. Liu, X. Gu, Z. Ji, W. Zou, C. Tang, F. Gao and L. Dong, *J. Phys. Chem. C*, 2013, **117**, 18578–18587.

3 W. Xu, Y. Cheng, J. Hou and P. Kang, *ChemCatChem*, 2023, **15**, e202201687.

4 M. Molina-Torres, O. Hernández-Cristóbal and R. Mendoza-Cruz, *Front. Nanotechnol.*, 2023, **5**, 1–17.

5 S. K. S. Hossain, J. Saleem, S. U. Rahman, S. M. J. Zaidi, G. McKay and C. K. Cheng, *Catalysts*, 2019, **9**, 1–19.

6 R. Daghrir, P. Drogui and D. Robert, *Ind. Eng. Chem. Res.*, 2013, **52**, 3581–3599.

7 L. A. Yusuf, Z. Ertekin, S. Fletcher and M. D. Symes, *Ultrason. Sonochem.*, 2024, **103**, 106792.

8 L. Yusuf, M. D. Symes and P. Prentice, *Ultrason. Sonochem.*, 2021, **70**, 105273.

9 D. L. Goldfarb, H. R. Corti, F. Marken and R. G. Compton, *J. Phys. Chem. A*, 1998,

102, 8888–8893.